MICROPARTICLE SAMPLING AND SEPARATION ENABLED BY DROPLET MICROFLUIDICS

by

Yuejun Zhao

B. S. in Thermal Engineering, Tsinghua University, 2001

M. S. in Thermal Engineering, Tsinghua University, 2004

Submitted to the Graduate Faculty of

Swanson School of Engineering in partial fulfillment

of the requirements for the degree of

Doctor of Philosophy

University of Pittsburgh

2008

UNIVERSITY OF PITTSBURGH

SWANSON SCHOOL OF ENGINGEERING

This dissertation was presented

by

Yuejun Zhao

It was defended on

July 18, 2008

and approved by

Minking K. Chyu, PhD, Leighton Orr Professor of Engineering,

Department of Mechanical Engineering and Materials Science

John A. Barnard, PhD, James T. MacLeod Professor of Engineering,

Department of Mechanical Engineering and Materials Science

Minhee Yun, PhD, Assistant Professor,

Department of Electrical and Computer Engineering

Dissertation Director: Sung Kwon Cho, PhD, Assistant Professor,

Department of Mechanical Engineering and Materials Science

MICROPARTICLE SAMPLING AND SEPARATION

ENABLED BY DROPLET MICROFLUIDICS

Yuejun Zhao, PhD

University of Pittsburgh, 2008

This work reports design, device fabrication, modeling and experimental results on new sampling and separation principles in which liquid is transported in a droplet form on a planner hydrophobic surface with no moving parts. The presented particle sampler and separator constitute core units for the handheld lab-on-a-chip-based airborne particle monitoring system.

For the airborne particle sampling, a novel method is developed by which the particles on the solid surface are swept and sampled by electrowetting-actuated moving droplets. Theoretical analysis and experimental works along with microfabricated testing devices are carried out to investigate the underlying physics and to optimize the sampling conditions. The sampling concepts are examined and proved on a solid surface and perforated filter membrane showing high sampling efficiencies.

For the particle separation, a new separation scheme is developed in which the mixed particles are separated within a mother droplet by traveling-wave dielectrophoresis (tw-DEP). Using the subsequent operation of droplet splitting by way of electrowetting, the separated particles can be isolated into each split droplet according to the DEP properties of the particles. This in-droplet separation is examined with many combinations of particles in microfabricated devices. By investigating the particle behavior as function of the frequency of the traveling wave DEP signal, the separation efficiencies are optimized.

The above microfluidic units constitute key components for upstream particle sampling and downstream sample processing in the lab on a chip system, providing the following advantages: extremely small amount use of samples/reagents (2) no external pressure source required for fluidic operations, (3) simple design and fabrication since no mechanical moving structure.

TABLE OF CONTENTS

LIST OF TABLES

LIST OF FIGURES

1.0 INTRODUCTION

1.1 MICROFLUIDICS

Microfluidics deals with the behavior, precise control and manipulation of microliter and nanoliter volumes of fluids. This multidisciplinary field, which intersects physics, chemistry, microtechnology and biotechnology, may be practically applied to the design of systems consisting of small volumes of fluids. Microfluidics emerged in the 1990s and have been used in the development of DNA chips, micro-propulsion, micro-thermal technologies, and lab-on-a-chip technology.

1.1.1 Droplet microfluidics

To date, most of these technologies have been developed based on continuous flows. Biological and chemical solutions are dispensed, pumped, mixed and regulated in a network of microchannels fabricated on a substrate such as silicon, glass, quartz, or plastic. Accordingly, the microchannel network is a core element in such a system. The channel plate is often bonded to another piece of substrate with inlet/outlet holes matching the ends of microchannels. In addition, micropumps, microvalves and micromixers have been added for precise and advanced fluidic handling and are often integrated into a single substrate with the microchannels. As a result, a complete continuous flow system tends to require complicated micromechanical structures,

raising the cost of design and fabrication and lowering the reliability of operation. Moreover, these types of systems are usually application-specific and offer little flexibility. For a new application, the system needs to be re-designed and re-fabricated. A different approach is needed which imposes less mechanical complication in the device and allows reconfigurability after production.

Alternatives to the closed-channel continuous-flow systems include novel open structures, where independently controllable discrete droplets are manipulated on a substrate. Following the analogy of microelectronics, this approach is referred to as digital microfluidics. By using discrete unit-volume droplets, microfluidic functions can be reduced to a set of repeated basic operations, such as moving one unit of fluid over one unit of distance. This "digitization" method facilitates the use of a hierarchical and cell-based approach for microfluidic biochip design. Therefore, digital microfluidics offers a flexible and scalable system architecture as well as high fault-tolerance capability. Moreover, because each droplet can be controlled independently, these systems also have dynamic reconfigurability, whereby groups of unit cells in a microfluidic array can be reconfigured to change their functionality during the concurrent execution of a set of bioassays. One common and powerful actuation method for digital microfluidics is electrowetting-on-dielectric (EWOD) that controls the wettability of solid surfaces. This principle has been proven highly efficient and versatile in realizing digital microfluidics.

1.1.2 Electrowetting on Dielectric (EWOD)

Lippmann [1] recognized over a hundred years ago that an externally added electrostatic charge may significantly modify the capillary forces at an interface. Since first introduced to the MEMS community by Matsumoto and Colgate [2], the notion of electrical control of surface tension

(i.e., electrocapillary or electrowetting) has been quite attractive for microdevices because of its inherent effectiveness in microscale and simplicity in implementation. Recently, this principle was also validated in the configuration where the electrode is covered with a thin insulating film [3, 4], as illustrated in Fig. 1(a). When an electric voltage is applied, the electric charge changes free energy on the dielectric surface, inducing a change in wettabilty on the surface and contact angle of the droplet [Fig. 1(b)]. This phenomenon, which is named electrowetting on dielectric (EWOD), has an excellent reversibility with many kinds of dielectric layers compared to the conventional electrowetting where liquids contact the conductive surface directly. For more details, see Lee et al. [5, 6] and Moon et al. [7].

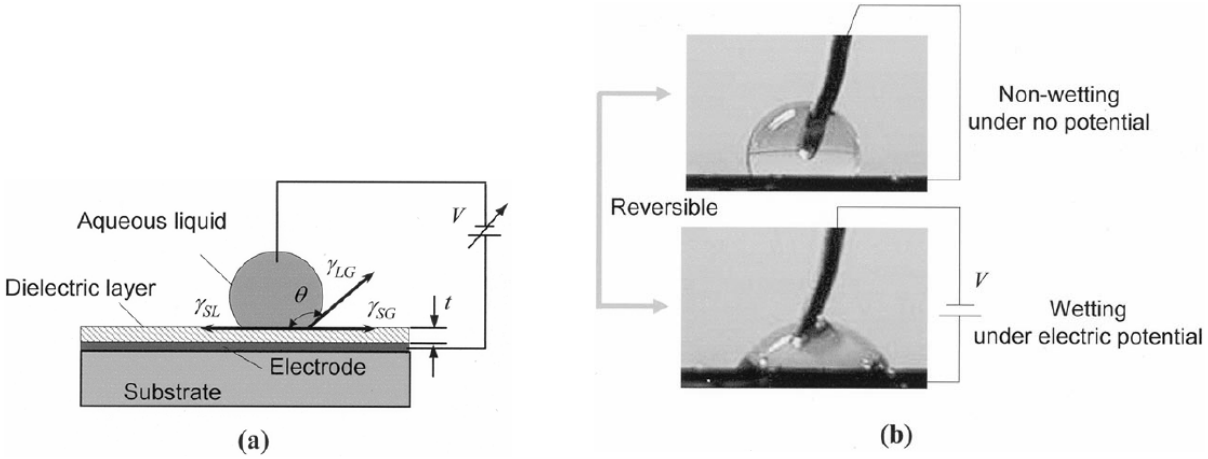

Figure 1. Principle of electrowetting on dielectric (EWOD). (a) Schematic configuration. (b) Pictures of basic EWOD demonstration (volume ~ 5μl).

According to Lippmann's equation, the solid–liquid interfacial tension γ_{SL} can be controlled by the electric potential across the interface, V:

$$\gamma_{SL}(V) = \gamma_{SL}\big|_{V=0} - \frac{C}{2}V^2 \tag{1}$$

where C (F/m^2) is the specific capacitance of the dielectric layer. For the case of EWOD where the electric potential at no external voltage is considered zero, V is equivalent to an applied voltage. At the three-phase contact line, the relation among contact angle θ and interfacial tensions is given by Young's equation:

$$\cos\theta = \frac{\gamma_{SG} - \gamma_{SL}}{\gamma_{LG}} \tag{2}$$

where γ_{SG} is the solid–gas interfacial tension and γ_{LG} the liquid–gas interfacial tension. By substituting (1) into (2), the change of contact angle by the electric potential represented by the cosine of contact angle, can be described as:

$$\cos\theta(V) = \cos\theta_0 + \frac{\varepsilon_0\varepsilon}{2\gamma_{LG}t}V^2 \tag{3}$$

where θ_0 denotes the equilibrium contact angle at $V = 0$ V, ε_0 (8.85×10^{-12} F/m) the permittivity of the vacuum, ε the dielectric constant of the dielectric layer, and t the dielectric layer thickness. Note in (3) that the contact angle change is not related to the polarity of the applied potential V.

If a patterned electrode over which a droplet is partially placed is activated, the droplet can be transported by breaking the force balance in the droplet. Likewise, sequential activations of addressable patterned electrodes can produce a continuous movement in a programmed way. Recently, Cho *et al.* have successfully demonstrated a variety of droplet operations: creating, transporting, splitting and merging of droplets [8, 9]. A droplet (450 nanoliters in volume) could be transported at variable speeds ranging up to as fast as 250 mm/s [8]. Furthermore, properly combined switching of multiple electrodes can generate splitting and merging of droplets. By activating two electrodes located beneath the two ends of a mother droplet, the mother droplet could be elongated and split into two daughter droplets. Merging was also achieved by activating the electrode between two droplets [9].

1.2 MICROPARTICLE SENSING SYSTEM

Exposure to airborne microorganisms in environments such as healthcare, agricultural and industrial workplaces, causes millions of episodes of health complications and disorders in the US each year. Many respiratory and other adverse health effects such as infectious, hypersensitivity pneumonitis, toxic reactions and sick building syndrome (SBS), can be caused by airborne biological particles [10-15]. The harmful airborne particles are diverse, including airborne infectious agents such as Legionella spores and Mycobacterium tuberculosis; indoor allergens such as Penicillium, Altenaria, Bacillus subtilis, Bacillus cereus and Actinomyces spores; invasive infectious fungal agents such as Aspergillus fumigatus and Aspergillus favus; and others. In particular, there has been an increased threat recently that certain microorganisms such as anthrax-causing Bacillus anthracis spores can be used as bio-warfare agents. A mason jar of anthrax sprayed over an urban area could infect 400,000 urban residents and possibly kill half of them in less than several weeks. Efficient sensing tools are crucial in the prevention and control of exposure to airborne biological particles in an immediate manner and are required to enable fast responses that are capable of avoiding possible catastrophe caused by exposure to agents such as anthrax.

To assess the bacterial and fungal contents suspended in air, they are usually sucked and impacted on an agar surface or impinged in a liquid medium by air flowing[12]. The collected bacteria and fungi are then cultured in a separated system for a period ranging from 2-3 days for most microorganisms; even up to 3-5 weeks for M. tuberculosis. By counting the colony forming unit (CFU) and observing its morphology, bacterial and fungi levels are enumerated and their genera are identified. All these operations are carried out manually by skilled technicians. This conventional process shows several drawbacks: (1) high fluctuations in measured data [16, 17],

(2) timeconsuming due to culture-based analysis, (3) likely misidentification of cultured morphology (since the identification is not based on DNA match or immunoassay), and (4) detecting only culturable microorganisms. These drawbacks result in significant underestimations of airborne microbial concentrations or false negative results, and a long analysis time [18, 19]. Most of the microorganisms vulnerable to vitality loss by the impaction as well as the non-culturable microorganisms cannot be detected in this system. However, such microorganisms also need to be monitored since the allergenic, toxic and inflammatory responses can be provoked by exposure not only to viable but also to non-viable microorganisms present in air [10, 15]. Therefore, a highly specific and sensitive direct measurement technique is more desirable than the culture-based analysis system.

One of the candidates for direct measurement is to use a lab-on-a-chip system [20-25] enabled by the MEMS (MicroElectroMechanical System) technology. The concept of the lab-on-a-chip is the miniaturization and integration of various biological and chemical analysis units using micro manufacturing technologies. This miniaturized system is capable of synthesizing chemicals efficiently and economically. Furthermore, the integrated system is fully capable of automatically carrying out biological and clinical analyses from sample introduction to bio/chemical separation and detection, all on a single chip of a credit card size or even smaller. Using this lab-on-a-chip system, direct identifications and concentration measurements of microorganisms can be made without culturing them. One of the possible scenarios is to use a lab-on-a-chip system embedded with DNA match technology [18] or immunoassay [26]. The main procedure for the DNA match technology is as follows: (1) collect airborne particles and sample them into reagents, (2) lyse the sampled microorganisms, (3) extract (separate) and amplify DNA of the collected microorganisms by PCR (polymerized chain reaction), (4) identify

microorganisms using a DNA micro array with hybridization (DNA match). In this process, one can not only identify microorganisms directly but can also make accurate measurements of their populations by quantifying their matched DNA concentration, regardless of their viability. This method allows us not only to reduce the processing time down to less than several hours (versus at least 2-3 days in the culture-based analysis) but also to shrink dimensions of the system down to the size of Pocket PC, thereby providing high mobility of the system.

However, the realization of the above lab-on-a-chip system has been hindered by the following issues: (1) lack of an efficient particle sampling method compatible with the lab-on-a-chip format. The conventional techniques require a large volume of liquid to impinge particles into liquid and/or wash particles from an agar surface for analysis in subsequent manual handling steps. Thus, they are impractical for implementation in a lab-on-a-chip system that typically processes micro-to-pico liter volumes. (2) Assay protocols are too complicated, especially in DNA amplification, and thus require the use of many microfluidic devices (such as pumps, valves, reactors, heaters, mixers, and other fluid regulators) for completing the analysis. In fact, PCR DNA amplification requires stringent isolation/purification of DNA from the cell debris prior to amplification (to avoid false positive amplification due to contamination) and numerous cycling steps (to achieve a detectable target concentration level) [27]. As a result, successful development of a reliable lab-on-a-chip system has been complicated by the difficulties in monolithic fabrication and integration of a number of complex micro components (especially for moving devices such as pumps and valves) on a single chip. To circumvent these current shortcomings a proposed novel airborne biological particle sensing system is illustrated in Fig. 2. The system consists of three main sequential units: droplet based particle collection, in-droplet sample preparation, and QDs-based detection. The droplet-based digital fluidic operations [8, 9,

28-30] can minimize the requirement of liquid volume for particle sampling and avoid the need for building moving components on the chip and the highly sensitive QD-based nano-biosensors [31, 32] can eliminate the need for PCR amplification, thereby simplifying assay protocols and system integration.

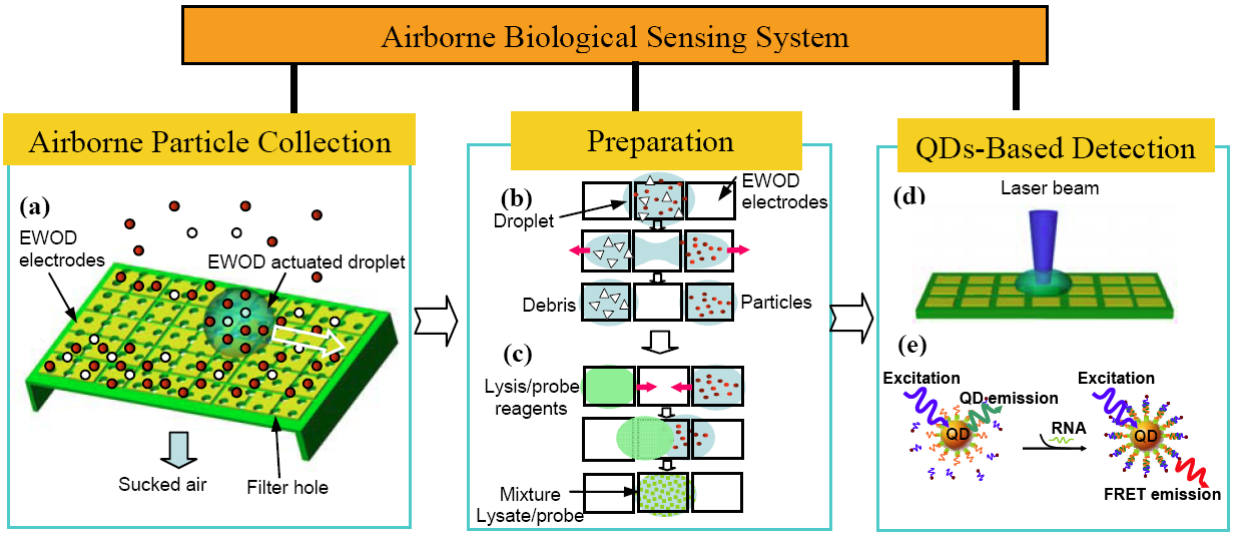

Figure 2. Concept of airborne biological particle sensing system. (a) Particles are collected on the filter membrane and sampled into an EWOD-actuated droplet. (b) Particles of interest are isolated and concentrated after unwanted debris is removed via in-droplet separation using dielectrophoresis and EWOD. (c) The particle droplet is mixed with another droplet containing lysis and probe reagents. (d) The processed sample droplet containing a mixture of cell lysate and probes is transported to a laser-focused region of a confocal spectroscope for fluorescence detection. (e) The specific bio-particles (e.g. Bacillus species) are detected based on DNA (probe)-RNA (target) hybridization and hybridization-mediated FRET using QDs as donors.

In the particle collection unit, air with suspended particles will be first sucked into the system and passed through a filter comprising of an array of micro size holes, allowing particle trapping on the filter membrane [33-35]. A mobile liquid droplet will then sweep and collect the particles on the filter membrane (Fig. 2(a)) and will be manipulated based on EWOD principles

[1, 3, 36]. Sequential activations of the electrodes underneath the droplet will make the droplet move continuously in a programmed way and pick up the particles on their paths. The capability to manipulate liquid droplets eliminates the need to build any microchannel network and pump/valve components for fluidic processing, enabling a very simple yet highly efficient chip-based unit for particle collection.

Next, the droplet containing the particles will be transported to the in-droplet sample preparation unit where the bio-particles of interest will be separated from the unwanted debris and then be concentrated (Fig. 2(b)). After mixing with the cell lysis buffer and probe reagents (Fig. 2(c)), the droplet of the mixture will be transported to the QDs-based detection unit for further analysis (Fig. 2(d)). Specifically, sample preparation will proceed as: (i) isolate/separate the bio-particles of interest and the unwanted debris in a droplet configuration using dielectrophoresis, according to their different dielectric properties, (ii) split the droplet in two using EWOD, by which the bio-particles are concentrated within a smaller droplet and the debris is confined in the other one, and (iii) merge the bio-particle droplet with another droplet containing cell lysis and probe/QDs reagents. This totally integrated on-chip sample preparation unit minimizes target loss (which is significant in conventional sample preparation methods due to inter-equipment mass transfer) and reduces the necessary amounts of samples of probe reagents, thereby leading to the enhancement in sensitivity and the reduction in time and cost of detection.

Finally, the droplet of target-probe mixture will be transported to a laser-focused region in the QDs-based detection unit (Fig. 2(d)) where the specific biological species will be identified based on RNA sequence match. A QDs-based RNA nanosensor (Fig. 2(e)) will be developed that detects a conservative region of ribosomal RNA (rRNA) of the target species.

The presence of the specific rRNA target will be detected based on DNA-RNA hybridization and hybridization-mediated fluorescence resonance energy transfer (FRET) using QDs as donors. The QD-FRET fluorescence signals will be measured using a custom-made confocal fluorescence spectroscopy apparatus [37, 38]. This apparatus allows measurements of a minimized sample volume (down to even the femtoliter range) with high signal-to-noise ratio [37, 38]and is amenable for miniaturization, thereby providing ideal detection readout for the coupling with the droplet-based sample preparation unit.

1.3 OBJECTIVES AND ORGANIZATION OF THE THESIS

The main goal of the work reported in this thesis was to realize the droplet based particle sampling and separation concept shown in Figure 2.

For the particle sampling unit, the particle sampling on the solid surface is introduced and the particle sampling on the perforated membrane is presented in section 2. The theory and modeling of the droplet actuation is also included. The goal was to investigate the physics behind the reversibility actuation and eventually offer a guideline for better designing perforated surface structures.

For the particle separation part the principle of travelling wave dielectrophoresis (twDEP) is introduced in section 3. Based on calculations and measurements of the twDEP force, the in-droplet particle separation was realized.

The experimental works are reported and discussed in each section and the conclusions and suggestions for the future work are given.

2.0 MICROPARTICLE SAMPLING BY DROPLET MICROFLUIDICS

Bioaerosols are diverse and complex particles of biological origin suspended in the air, including pollen, fungal spores, fragments of fungal mycelium, bacterial cells and endotoxins, viruses, protozoa, and fungal mycotoxins. Exposure to harmful bioaerosols in indoor and outdoor environments can result in many respiratory and other adverse health effects such as infection, hypersensitivity, pneumonitis, toxic reactions, sick building syndromes (SBS). In particular, there has recently been an increased bio-terrorism threat since certain microorganisms such as anthrax-causing Bacillus anthracis spores can be used as bio-warfare agents. In order to control and prevent exposure to harmful airborne biological particles, many studies have been carried out for better sampling and monitoring methods[12, 14, 39, 40].

Typically, airborne microorganisms are identified and quantified following two major steps: sampling and analysis. Over the past years a number of bioaerosol samplers including portable samplers have been developed and evaluated[16, 17, 41-44]. In general, there are three kinds of principles to sample (collect) bioaerosols: impaction of airborne particles onto a nutrient agar, particle filtration by membrane filters and particle sampling into liquid by using bubblers or impingers. Then, the sampled particles are finally identified and quantified using microscopic, microbiologic, biochemical, immunochemical, or molecular biological analysis. Typically this is done on a conventional laboratory scale which requires many skilled technicians and massive, expensive facilities. On the contrary, the lab-on-a-chip system[20, 21, 23, 45] brings us many

advantages over the conventional analytical technologies: short processing time, drastic reduction of reagent and sample consumption, small mass of the equipment, full automation, parallel analysis, high throughput, highly sensitive and specific output signals, and so on. However, seamlessly integrating the lab-on-a-chip system with the existing bioaerosol samplers is still challenging. The conventional samplers require not only a large volume of liquid in impinging particles into liquid or extracting particles from the agar surface but also numerous manual handling steps. Recently, Frisk et al.[46] reported a micromachined interface (~ cm^2 in sampling area) for airborne sample-to-liquid adsorption. Their device uses a pump to generate a constant flow, a paper filter for the front-end collector of molecules or particles and a controllable heater to facilitate evaporation of interesting substances, demonstrating a significant reduction in detection time and device size. However, their system still requires many manual steps and the liquid volume far above the micro-to-pico liter range, which may hamper in creating a fully-automated portable lab-on-a-chip system for airborne particle monitoring.

2.1 ENVISIONED AIRBORNE PARTICLE COLLECTION SYSTEM

In the meantime, in the process of particle sampling into liquid, it may be more efficient to move the air-to-liquid interface rather than particles, especially in microscale devices[35, 47]. Based on this principle, a new sampling system[48] is envisioned as illustrated in Fig. 2. In this system[9, 28], when air suction is applied through the filter membrane, airborne particles of interest, supposedly lager than the filter hole size, are stopped on a filter membrane. Then a liquid droplet is moved around on the filter membrane by the electrowetting on dielectric (EWOD[36, 49, 50]) principle, picking up the particles on the filter surface and sampling them into the droplet itself.

In this pickup process, the interfacial tension of the moving droplet is responsible for the detaching of the particles from the surface. Finally, the droplet containing the sampled particles can be transported automatically to an adjacent lab-on-a-chip analysis system, also by EWOD actuation. This automatic transportation will eliminate manual handling steps between particle sampling and analysis that are typically required in the conventional system. Various fluidic operations and analysis steps can follow immediately without any inter-equipment sample loss, enabling on-chip analysis. More importantly, this technique uses an extremely small volume of sampling liquid (several droplets of submicro-liter range) without any external pumps. As a result, sampling itself can be a simultaneous concentration process as well, possibly eliminating the need for an additional downstream concentration.

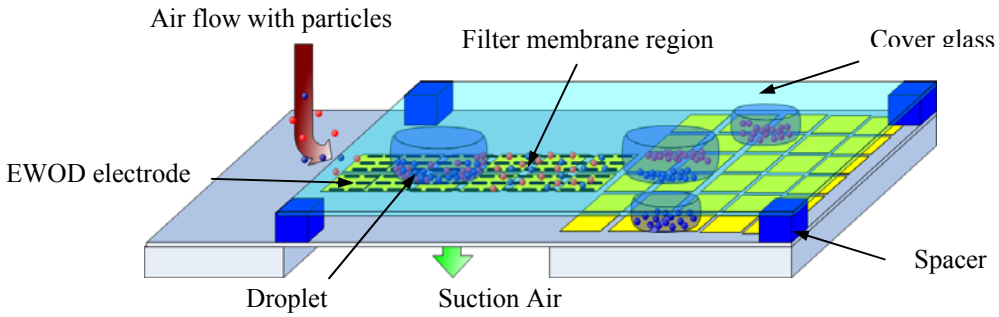

Figure 3. Envisioned airborne particle collection system integrated with digital microfluidics for sample analysis. The droplets are moved by activating the array of electrodes, so called EWOD (electrowetting on dielectric), sweeping the particles on the filter membrane. The droplets containing the particles are automatically transported by EWOD to the next section for downstream on-chip analysis.

2.2 PARTICLE SAMPLING ON A FLAT SURFACE

In this section, particular focus is placed on particle sampling from flat solid surfaces, not from the filter membrane (structured surface), as fundamental issues in the course of developing of the envisioned particle sampler. In order to assess the particle sampling efficiency by electrowetting-actuated droplets, three different types of micro particles are selected based on the hydrophobicity of the particle, and carefully deposited on a solid surface. Then, their sampling efficiency has been examined after droplets actuated by electrowetting principle sweep and sample the particles.

2.2.1 Static force balance in particle

As illustrated in Figs. 3 and 4, when a droplet actuated by electrowetting principle passes spherical micro particles, there exist two regions involved in particle removal and collection from the surface: advancing and receding regions of the droplet. The passage of the air-to-liquid interface can generate a force in the upward direction such that the particle can be eventually levitated from the surface. Of course, it appears that, under properly chosen wetting conditions [51] of the particle and the substrate, the particle can be removed. In order to find the proper conditions, it is important to identify the significant forces acting on the particle in micro or submicro scale. On a static equilibrium, the forces acting on the particle are the adhesion force, the gravity force, the hydrostatic force of the liquid, and the surface tension force. Among them, the gravity force and the hydrostatic force are proportional to the third power of the particle radius R, and thereby negligible at the scale where the radius of the particles is below 10 μm[51].

Thus, the adhesion force and the surface tension force are dominant forces that largely determine the force balance on the particle.

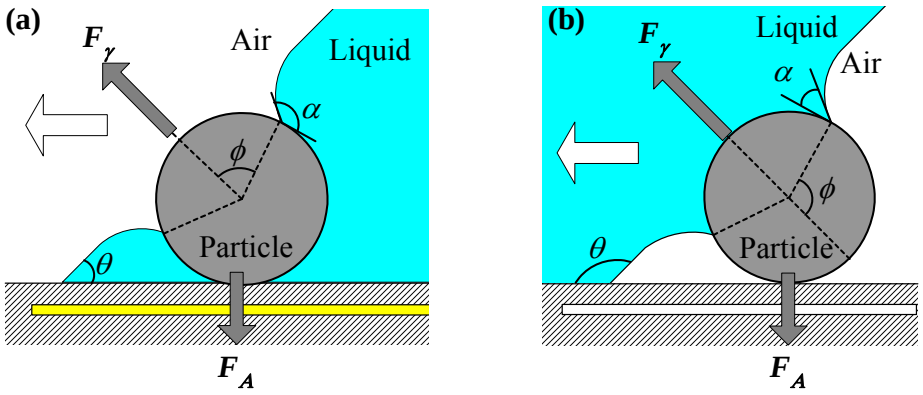

Figure 4. Microscopic views of spherical particle sampling on a dielectric solid surface during the passage of the air-to-liquid interface: (a) Advancing region of the droplet (hydrophilic dielectric surface); (b) Receding region of the droplet (hydrophobic dielectric surface). Surface tension force acts on the particle as a detaching force from the solid surface against the London-van der Waals adhesion force. Note that the dielectric solid surface on the electrode can be switched from hydrophobic ((b)) to hydrophilic ((a)) by electrowetting actuation.

If we assume that there is no chemical bonding between a particle and a substrate, the adhesion for particles generally smaller than about 10 μm in radius is primarily caused by van der Waals forces. For this idealized case the adhesion force can be represented by

$$F_A = \frac{AR}{6H^2};\ H << R, \tag{4}$$

where F_A is the London-van der Waals force, A the Hamaker constant, R the particle radius, and H the gap between the particle and the substrate. A reasonable value of A for metallic and oxide particles adhering to a solid surface immersed in water ranges around 10^{-19} Joule. For H the value of 1 nanometer is taken because adhesion forces corresponding to H-values quite close to

1nm are mostly determined[52, 53]. Equation (4) shows that at constant gap H the adhesion force decreases linearly with decreasing particle size. A close-to-linear relationship has also been observed experimentally elsewhere[53, 54].

In the mean time, the surface tension force acts on the particle with the circular line contact (the solid-liquid-gas contact line), of which magnitude and direction are completely determined by the position of the contact line on the particle (angle ϕ), the contact angle of the fluid on the particle (angle α), the particle radius R, and the liquid-gas interfacial tension γ_{lg}, as shown in Fig. 4. The resultant surface tension force F_γ in the advancing region, as shown in Fig. 4(a), is given by

$$F_\gamma = 2\pi R\gamma_{\mathrm{lg}} \sin\phi \sin(\alpha - \phi). \tag{5}$$

The vertical component of F_γ is also given by $F_{\gamma v} = F_\gamma \cos\theta$, where θ is the contact angle of the liquid on the solid surface. When $F_{\gamma v}$ is positive (i.e., upward direction in Fig. 4(a)), the surface tension force acts as an opposing force to the adhesion force F_A, contributing to the particle removal from the surface.

Similarly, in the receding region the vertical component of the surface tension force can be calculated. Depending on the contact angle θ on the solid surface, the angle ϕ (i.e., how much the particle is immersed into the liquid), and the contact angle α on the particle, the direction of $F_{\gamma v}$ changes. For example, in case of $\theta < 90^{\mathrm{o}}$ in the advancing region as shown Fig. 4(a), the vertical component of surface tension force $F_{\gamma v}$ has positive values when $\alpha > \phi$, while its direction is reversed when $\alpha < \phi$. That is, the force $F_{\gamma v}$ is in the upward direction in limited regions as the particle is immersed. By differentiating Eq. (5), it can be obtained that the maximum values of positive $F_{\gamma v}$ occur when $\phi = \alpha/2$. We can expect the particles to be removed from the solid surface if $F_{\gamma v,max} > F_A$.

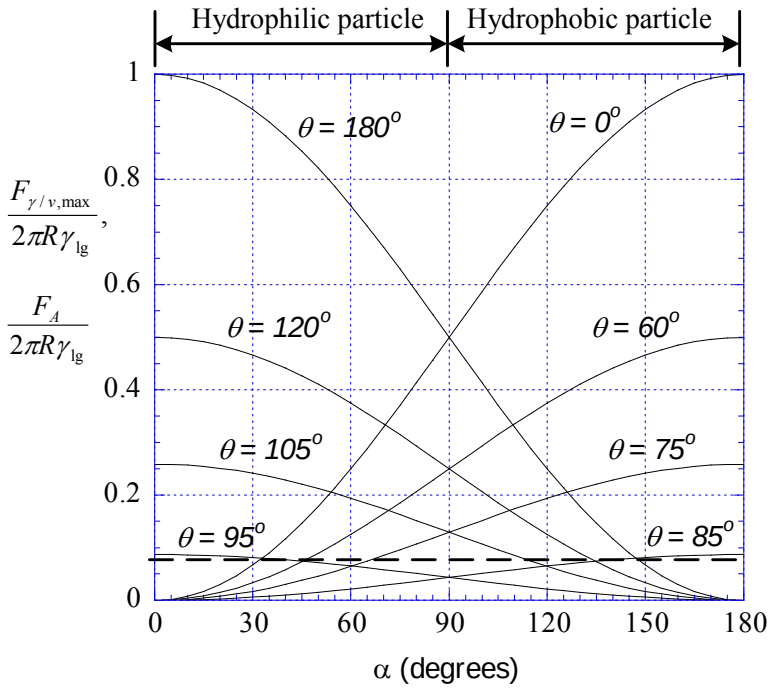

Figure 5. Static analysis and comparison of surface tension force $F_{\gamma/v,\,max}$ with the adhesion force F_A under variations in wetting properties of the particles and dielectric substrate surface. The dashed line represents F_A divided by $2\pi R\gamma_{lg}$.

More results over a wide range are shown in Fig. 5. Note in Fig. 5 that the region above the dashed line is where the removal force by the surface tension is large enough to effect removal. It can be seen in a wide range of θ and α that the removal force by surface tension is dominant over the adhesion force, indicating the present sampling technique would be effective over a wide range. However, the region below the dashed line reveals that it would be difficult to remove particles. If α and θ are chosen improperly, for example, $\alpha = 60^o$ and $\theta = 85^o$, particle removal might not take place as illustrated in Fig. 5. Also note in Fig. 5 that the hydrophilic particles ($\alpha < 90^o$) can be removed more likely if the solid surface is hydrophobic ($\theta > 90^o$) than hydrophilic ($\theta < 90^o$), and vice versa. Therefore, the droplet sweeping can remove and sample

both types of particles: hydrophobic as well as hydrophilic. Considering that it is in the advancing region of the droplet that the solid surface is switched from hydrophobic ($\theta \approx 120^{o}$) to hydrophilic ($\theta \approx$ down to 70^{o}) by electrowetting, hydrophobic particles are expected to be more likely removed and collected in this region, while in the receding region the hydrophilic particles are expected to be sampled more likely. However, this is simply based on the static force analysis[51]. Real situations are more complicated as will be discussed in the Result and Discussion section.

It is relevant to point out that the ingenuity of this particle sampling method lies in the fact that F_γ is proportional to R as is F_A, unlike other sampling methods which exert forces that are $O(R^2)$ or $O(R^3)$. Thus, for very small R the force F_γ still remains dominant enough to oppose the F_A forces, perhaps effective even in sampling submicron-size particles.

2.2.2 Testing device fabrication and experiment setup

In order to examine particle sampling on flat solid surfaces, testing devices are fabricated based on the standard lithographic micro fabrication technology, as illustrated in Fig. 6. Testing devices are mainly made up of two parallel plates (top and bottom). The main fabrication process on the bottom plate consists of three steps: metallization and patterning of electrodes, deposition and patterning of the dielectric layer, and deposition of the hydrophobic layer.

For the driving electrodes, a chromium layer of 100 Å in thickness as an adhesion layer and a gold layer of 2000 Å in thickness are sequentially deposited on a glass wafer by an e-beam evaporator and then patterned by wet etching. Each planar driving electrode is of square type with an area of 1.4×1.4 mm^2, separated by a 50 μm gap from the adjacent electrodes. Then, a

2000 Å silicon dioxide (SiO2) layer as the dielectric layer is deposited using a PECVD (plasma enhanced chemical vapor deposition) process, followed by opening of the oxide layer on electrode connection pads by wet etching in order to transmit activation signals to each driving electrode. Finally, the bottom plate is finished with a hydrophobic Teflon layer. Spin-coating of 2 % Teflon solution (Teflon AF 1600® + Fluorocarbon solvent) results in a 2000 Å thick Teflon layer. This Teflon AF® layer acts as the dielectric layer as well. The relationship between the required voltage for reliable electrowetting actuations and the selection of dielectric layers has been discussed in Moon *et al*[7].

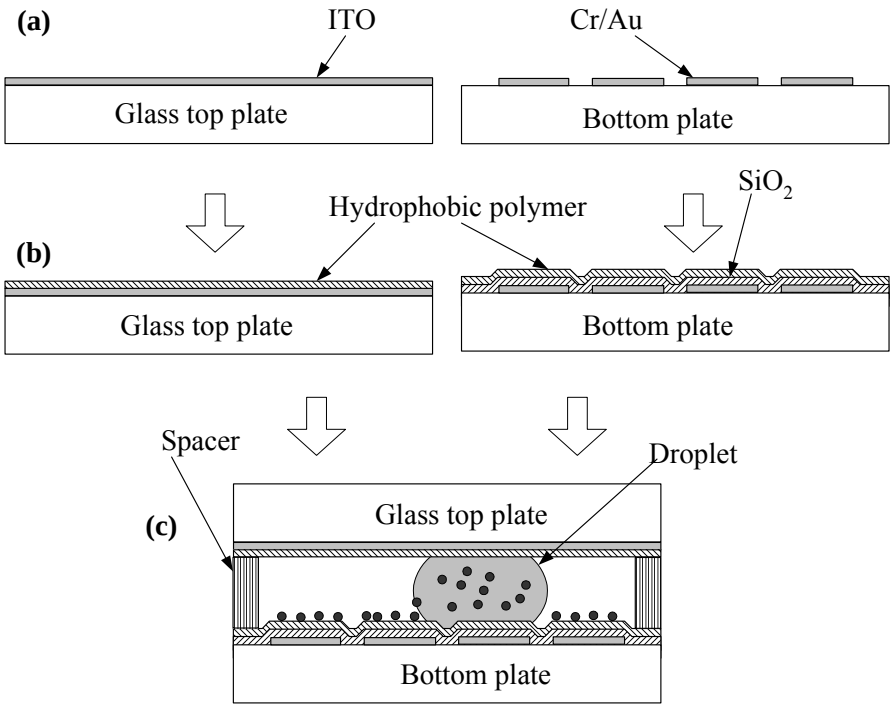

Figure 6. Fabrication process flow of testing device: (a) Top glass plate with ITO (Indium Tin Oxide) layer/Metallization and patterning of electrodes (Cr/Au) on the bottom plate; (b) Deposition of oxide layer (SiO2) by PECVD on the bottom plate/Deposition of polymer layer on both plates; and (c) Integration of the top and bottom plates with spacers in between.

Meanwhile, the top glass plate first coated with an ITO (Indium Tin Oxide) layer is also spin-coated with the hydrophobic Teflon layer. The ITO layer covering the entire area of the top glass plate is served as grounding and its transparency makes droplet motions visible. The last fabrication process is to integrate the two plates (Fig. 4(c)). The first step in the integration is that dry particles are indirectly deposited on the bottom plate with particular care. To improve the uniformity in deposited particle distribution, dry particles are first deposited on a dummy vinyl membrane which is afterwards turned upside down over the bottom plate. The particles are still adhered to the dummy membrane surface yet. By gently tapping the dummy membrane, particles adhered on the dummy membrane surface are detached and landed on the bottom plate. This method is simple, yet providing much better uniformity than the direct deposition method. The second step in the integration is that after pipetting a water droplet on the bottom plate the top glass plate is gently pressed against the spacers for which four layers of the double-sided tape of about 150 μm thickness are placed in stack in the four corners on the bottom plate. Therefore the gap between the top and bottom plates, that is around 600 μm, is defined by the spacers.

For droplet actuations, the integrated testing devices are connected to a driving circuit system consisting of a personal computer, a digital output board (DAQPad-6507, National Instrument), and a custom-made interface circuit mainly made up of photo-coupled relays. A PC-based program generates control signals outputted through the digital output board. Then, the control signals switch the relays in the custom-made interface circuit that provide activation voltages to the electrodes on the testing devices. The applied voltage to the electrodes is set at V_{cc} = 65 VAC at 1 kHz.

2.2.3 Results and discussion

2.2.3.1 Proof of concept First of all, in order to prove the present sampling concept, two extreme cases of particle types in terms of hydrophobicity are selected: super hydrophilic and super hydrophobic. For the super hydrophilic particle type, borosilicate glass beads (8 μm in diameter, 9000series, Duke Scientific Inc.) of which contact angle (α) with water is 14^{o} [55] are selected and tested. For the super hydrophobic particle type the borosilicate glass beads are coated with an amorphous Teflon layer. The contact angle α with water is around 120^{o}, which is close to the maximum intrinsic contact angle attainable as of today. This angle is estimated based on the measured values with millimeter-size water droplets on flat amorphous Teflon layers[7, 9].

The super hydrophilic (8 μm-diameter glass beads) particles are first examined as demonstrated in sequentially captured pictures in Fig. 7. An array of the driving electrodes is patterned in such a manner that the droplet moves in a square path (Fig. 7(a)). Millions of borosilicate glass micro spheres are then deposited on the bottom plate using the indirect method. After a droplet is in place, the top cover is pressed against spacers (Fig. 7(b)). The solid surface of the bottom plate looks frosted due to the deposited particles. It is seen that many particles have been already sampled around the droplet. This is because the droplet is moved a little bit when manually dispensed on the bottom plate. By sequentially activating the driving electrodes in a counter clockwise direction (65 VAC, 1 kHz), the droplet moves along the path, simultaneously sweeping and sampling the particles into the droplet (Figs. 7(b)-(e)). The path on which the droplet has passed become clear, not frosted anymore, indicating that the particles barely remain on the path. Furthermore, this sampling technique effectively works even with the clustered particles (Figs. 7(c)-(e)). Although particles are indirectly deposited using the dummy

membrane, there are still found many particle clusters as observed in the form of large circular dots in Fig. 7. However, these clustered particles are effectively picked up by the droplet as well. Finally, we can see that the sampled particles are suspended inside the droplet (Fig. 7(f)).

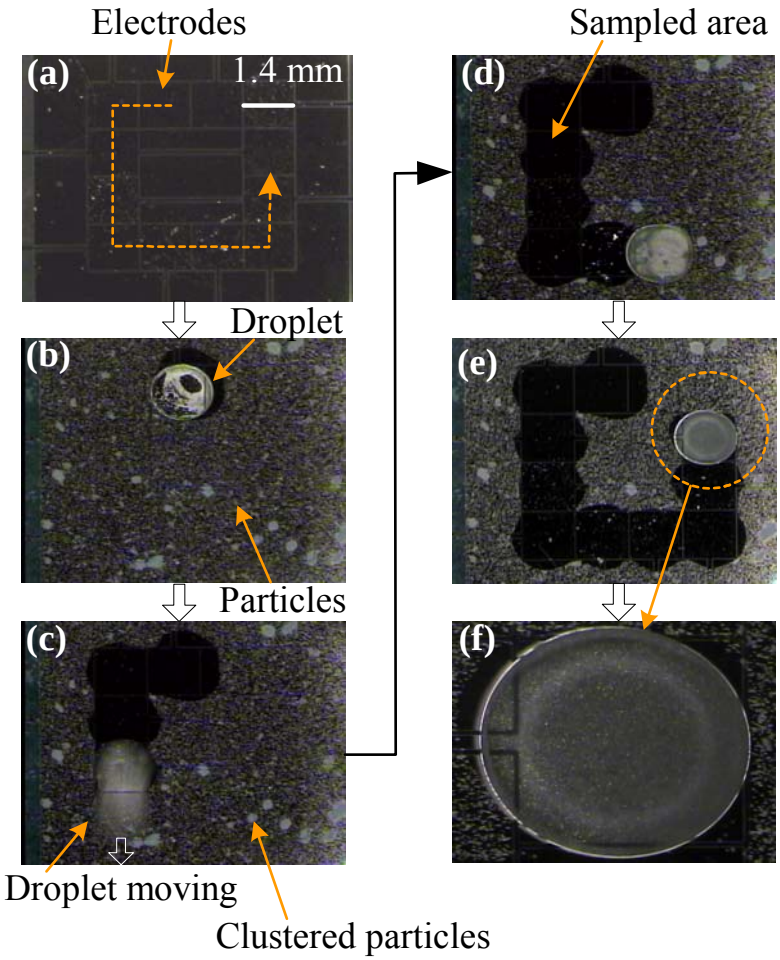

Figure 7. Sequential pictures of 8 μm-diameter borosilicate glass bead sampling viewed through the transparent top glass plate. The particles (even clustered particles) on the solid surface can be efficiently sampled into the droplet. The dashed line in (a) indicates the path of the droplet; (f) Magnified view of the droplet. The sampled particles are suspended within the droplet.

Interestingly, it is observed during the droplet moving that the electric field inside the droplet induced by electrowetting actuation signals generates violent motions in the suspended

particles. This phenomenon gives us a positive effect that prevents the suspended particles from attaching to the surface again. Furthermore, whether this particle motion exists or not can be used as an indicator to determine whether or not particles are completely sampled into and suspended in the water droplet. When particles stay on the air-to-water interface or remain on the solid surface as deposited, the violent particle motion was not observed. It is speculated that the electrokinetic force [56] is responsible for this phenomenon. The electric field for the electrokinetic force can be produced by electrowetting actuation signals without adding any additional electrodes. Of course, the frequency of the applied electric signal and the shape and arrangement of the electrodes need to be optimized to maximize the dielectrophoretic effect. However, the frequency of the applied signal can be chosen almost independently without significantly affecting electrowetting actuations since the electrowetting actuation is effective in a relatively wide range of the applied frequency.

The present sampling method also works with Teflon-coated glass beads (super hydrophobic particle, 8 μm in diameter), as shown in Fig. 8. Due to difficulty in availability of the super hydrophobic spherical particles, they are prepared by coating the borosilicate glass beads with an amorphous Teflon layer. The glass beads are immersed into a 0.2% Teflon AF® solution diluted with a fluorocarbon solvent and then dried in an ultrasonic bath to minimize the particle aggregation. As a result, the surface of the glass bead becomes super hydrophobic. Presumably, the contact angle on the Teflon-coated particle can be considered equal to the one on the bulk Teflon material (around 120^{o} [7, 9]). As shown in Fig 6(a), the coated particles are deposited on the bottom plate. Differently from the hydrophilic particle case, the Teflon-coated particles are easily aggregated as the white dots on the black background are much bigger than

those in Fig. 7. The strong aggregation of the Teflon-coated particles was also confirmed under a high power microscope.

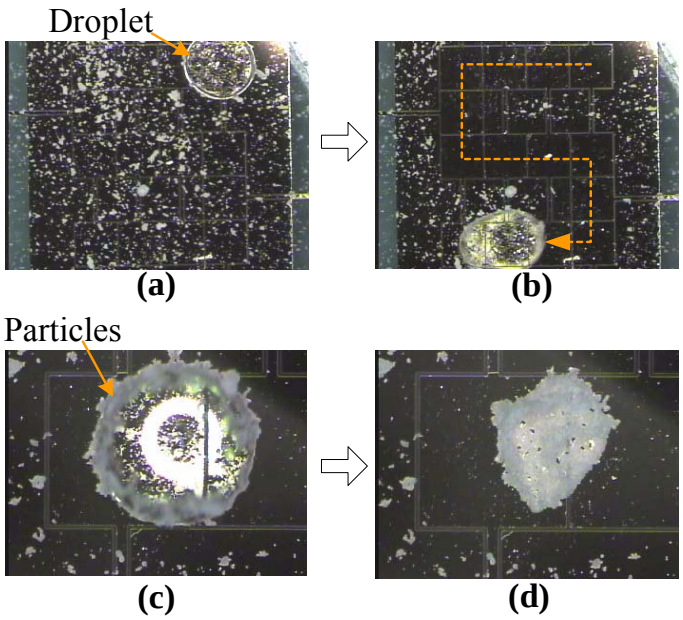

Figure 8. Sequential pictures of particle sampling of Teflon-coated glass beads (super hydrophobic): (a) Teflon-coated particles and a water droplet are deposited; (b) the droplet is sampling the particles along the electrowetting-actuated path; (c) Magnified view of the droplet. Most particles are adsorbed on the air-to-water interface. Note that the top glass cover is removed to enhance evaporation; (d) the sampled particles are remained on the surface after the water droplet is completely evaporated.

In any case, the droplet is also actuated along the 's' letter pattern as shown in Fig. 8(b). As the droplet moves, the hydrophobic particles are also picked up. As a result, the 's' path becomes clean, not much frosted anymore. Other than the super hydrophilic particles that are absorbed or suspended inside the water solution, the picked-up super hydrophobic particles are staying (adsorbing) on the air-to-water interface of the droplet, as shown in Fig. 8(c). This is because the Teflon-coated particles are super hydrophobic. The interfacial tensions prevent the

particles from detaching from the air-to-water interface and moving into the water solution. As a result, all the collected particles are accumulated on the air-to-water interface. This causes the following problems. The total distance a single droplet can sweep over is much shorter than the hydrophilic particle case since particle storage is restricted to the interface of the droplet which is not enough for all deposited particles. In order to sample all particles in a given area, many fresh droplets need to be provided. Furthermore, the particles on the interface hinder droplet movement as discussed more details later. Many times it was observed that the droplet could not be moved anymore by electrowetting actuation after travelling a certain distance, especially on the surface deposited with a high concentration of the Teflon-coated particles.

Meanwhile, the present sampling method can be used to concentrate particles by incorporating evaporation process. The top glass plate was deliberately removed to enhance evaporation (Fig. 8(c)). About 3 minutes later the water droplet is completely evaporated, as shown in Fig. 8(d), leaving a large pile of the collected particles.

2.2.3.2 Sampling efficiency In addition to the aforementioned two extreme cases, other types of particles are also examined, as tabulated in Table 1, in order to study the following issues: (1) to see whether or not the present sampling method works with the intermediate contact angle. As being intermediate between two extreme contact angles, polystyrene particle (DRI-CAL™, Duke Scientific Co.) of which contact angle is about 66^{o} [27] has been selected and examined; (2) to see the particle size effects on the sampling behaviour. 2 μm-diameter borosilicate glass beads (9000 series, Duke Scientific Co.) are also examined and compared with the same glass beads but different size (8 μm); (3) to re-confirm the sampling behaviour with the super hydrophobic particle. Since the Teflon-coated glass bead strongly aggregated together and may not be fully

covered with the Teflon layer although it could not be checked, 3-μm PTFE particles (poly tetra fluoro ethylene, Zonyl® MP 1200, Dupont Inc.) are also examined. The estimated contact angle (α) is about 110^{o} [55]; (4) to quantify the sampling efficiency for each particle type.

Figure 9 shows the experimental results for the four different types of particles: 8-μm glass beads, 2-μm glass beads, 8-μm polystyrene beads and 3-μm PTFE particles. The droplets are also actuated following through the 's' letter pattern. It is seen that 8-μm glass beads (Fig. 9(a)), 2-μm glass beads (Fig. 9(b)) and 8-μm polystyrene beads (Fig. 9(c)) are almost completely picked up by the droplets. After the droplets passed, their paths become clean, not frosted. For the PTFE particle case, however, the path still looks frosted, as shown in Fig. 9(d) and, more clearly, in Fig. 11, although a large number of the particles have been picked up.

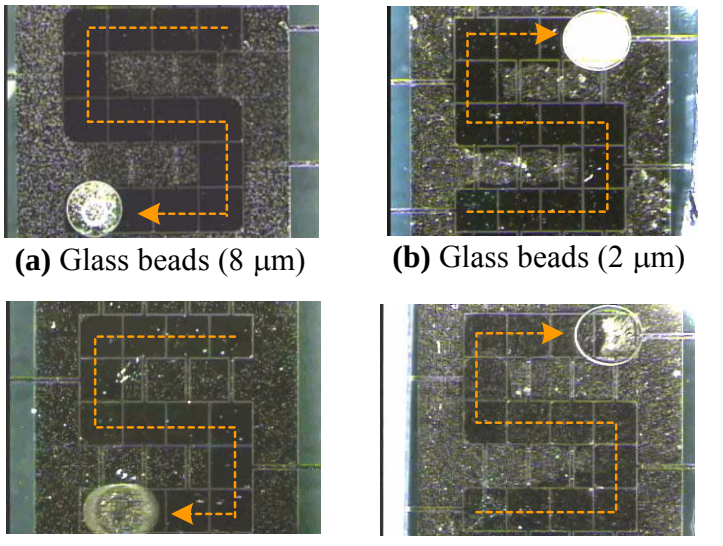

(a) Glass beads (8 μm) **(b)** Glass beads (2 μm)

(c) Polystyrene beads (8 μm) **(d)** Teflon powder (3 μm)

Figure 9. (a)-(d) Sampling results of different particle types. Droplets are moved along the 's' letter path. Except the Teflon powder case, the paths are clean after the droplets passed, showing the high sampling efficiency. The magnified view for the Teflon powder case is shown in Fig. 11

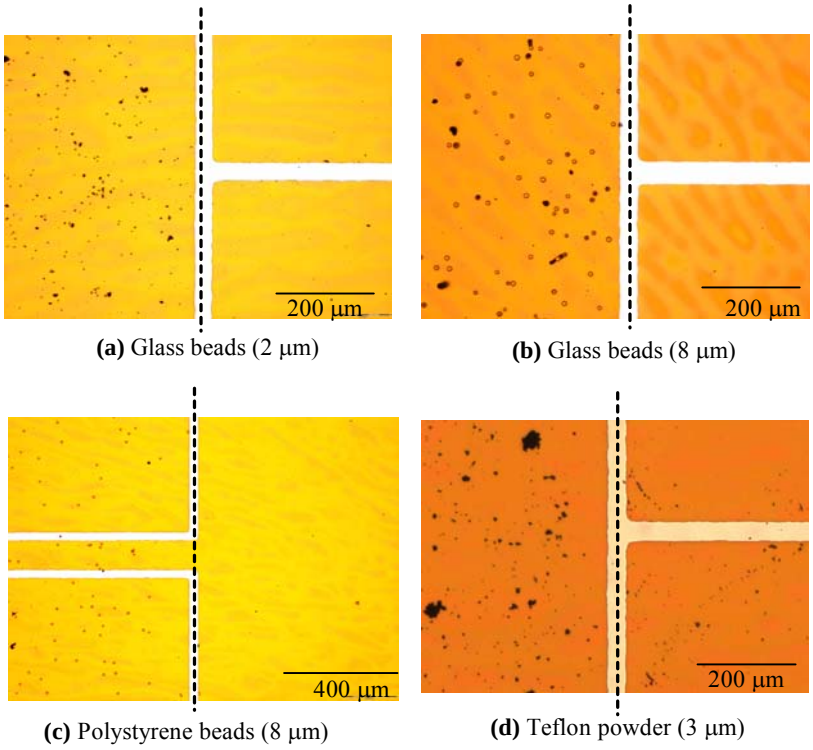

(a) Glass beads (2 μm) **(b)** Glass beads (8 μm)

(c) Polystyrene beads (8 μm) **(d)** Teflon powder (3 μm)

Figure 10. Magnified pictures at the footprint boundary of the moving droplet showing the particle sampling efficacy for each type of particle. The droplet has passed on the right side of each broken line. Almost all the deposited particles are removed on the right side except with the Teflon powder, while the particles on the left side remain intact as deposited.

The results shown in Fig. 9 can also be confirmed with the magnified pictures shown in Fig. 10. For comparison, the picture for each particle case is taken at the footprint edges of droplet paths. The right side of the broken line for each particle type is on which each droplet has passed. Almost all the particles for the 2-μm and 8-μm glass bead and 8-μm polystyrene bead cases are effectively removed on each right side, as shown in Figs. 10(a)-(c), suggesting that the present sampling method is highly effective over a wide range of the particle contact angle (α), at least up to 66^{o}. However, the sampling efficiency seems to be lowered with the super hydrophobic particles. As shown in Fig. 10(d), many PTFE particles are still found on the right

side of the broken line. Meantime, the particles on the left side remain intact as deposited. This area can be used as a base image to indirectly compare how many particles are sampled after droplet sweeping.

Table 1. Tested particle types and their sampling efficiency

Particle Name	Borosilicate glass		Polystyrene	Teflon coated glass	Teflon powder
Diameter (μm)	2	8	8	8	3
Contact angle (α) with water	14^o	14^o	66^o	120^o	110^o
Sampling efficiency η (%)	93.9	98.7	93.3	N/A[a]	68.7

[a] Strong particle aggregation makes it difficult to quantify the sampling efficiency.

In order to quantify the sampling efficiency for each particle case, two areas for each particle case are taken along the edge of the droplet footprint. One is from where the droplet swept and the other from where the droplet did not. Using the 'touch count' function in analySIS® FIVE image analysis software, the number of particles in the droplet-passed area is counted by *m* and the number of particles in the other area is counted by *n*. Then the sampling efficiency is calculated by $\eta = (n-m)/n$. For particle clusters, the total particle number was roughly estimated based on the cluster area. To minimize any marked deviation from the true values in the sampling efficiency, this procedure was repeated in ten different spots and the

sampling efficiency was averaged out. The averaged sampling efficiency for each case is shown in Table 1. As consistent with the images shown previously, for the glass bead and polystyrene bead cases, the sampling efficiencies are all over 93%, especially the highest efficiency, 98.7 % for the 8-μm glass beads. It does not seem to be much size-dependent in sampling, at least within our experimental range, considering only about 5% difference between 2 μm and 8 μm glass beads. Also polystyrene beads show the high sampling efficiency. As expected, however, with the PTFE particles the sampling efficiency is significantly lower than the other types of particles. It is not clear at this moment how the sampling efficiency would change in the range of $66^o < \alpha < 110^o$. There might be a rapid or gradual drop in the sampling efficiency. More in-depth studies are required to answer this question.

Since the camera used is not fast enough, it is not sure whether particles are mostly sampled in the advancing region or the receding region for each particle type. However, for the PTFE particle case only, it turns out that most of the particles are sampled in the receding region, as shown in Fig. 11. The broken circles in Fig. 11 indicate the droplet positions prior to actuation. After actuation, the droplet moves one step right. Note in Fig. 11(a) that, after the droplet moves to the right, the particles (in white) gather in a particular area within the droplet contour, but not within the contour of the previous droplet. As the droplet moves one more step right again, the particles gather again in the similar way, as shown in Fig. 11(b). Here, one interesting thing is that the gathered particles appearing in Fig. 11(a) disappeared in Fig. 11(b). Since the PTFE particles are super hydrophobic, they stay (adsorb) on the air-to-water interface of the droplet, not inside the droplet. This means that the gathered particles are removed from the solid surface when the droplet leaves the solid surface in the receding region. Then all collected particles are staying on the interface.

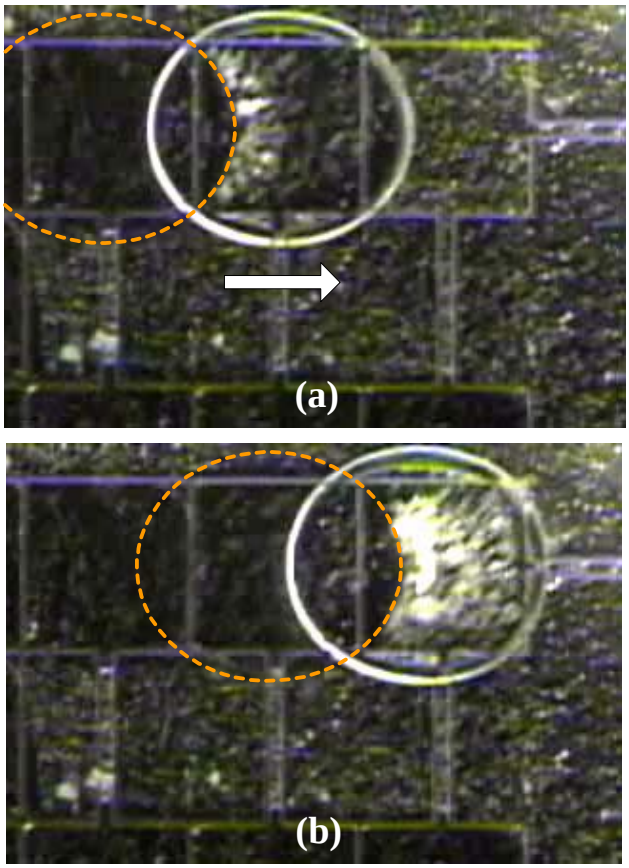

Figure 11. Magnified sequential views of sampling the Teflon powder. The broken circles are drawn to depict the initial shape of the droplet before moving to the next right electrode. (a) It is seen inside the contour of the droplet that the particles gather. (b) The particles gathered in the previous step disappear and another group of particles gathers inside the droplet contour again, but not in the overlapping area with the previous droplet footprint.

Here is a question of why the particles gather when the droplet moves. One of the possible scenarios is illustrated in Fig. 12. As the droplet moves right, a circulating fluid motion in a clockwise direction is induced in the lower part of the droplet while a fluid motion in a counter clockwise direction in the upper part. Therefore the particles in the advancing region of the droplet experience the downward flow to the solid surface and then are held down on the lower interface of the droplet. Since the particles are super hydrophobic, they cannot be absorbed into the droplet. As the droplet moves further, the particles (hatched particles in Fig. 12) reach

the receding region of the droplet and are then lifted up from the solid surface. In contrary to the advancing region, the particles experience the upward fluid motion. In this scenario, the advancing region is where the particles are likely to be accumulated due to the circulating flows in the droplet. The particle accumulation in the advancing region will be one of the main causes hindering the droplet from advancing. Apparently, the particles underneath the droplet, especially near the advancing region, reduce the contacting area of the droplet advancing front to the solid surface. As a result, the electrowetting driving force will be lowered.

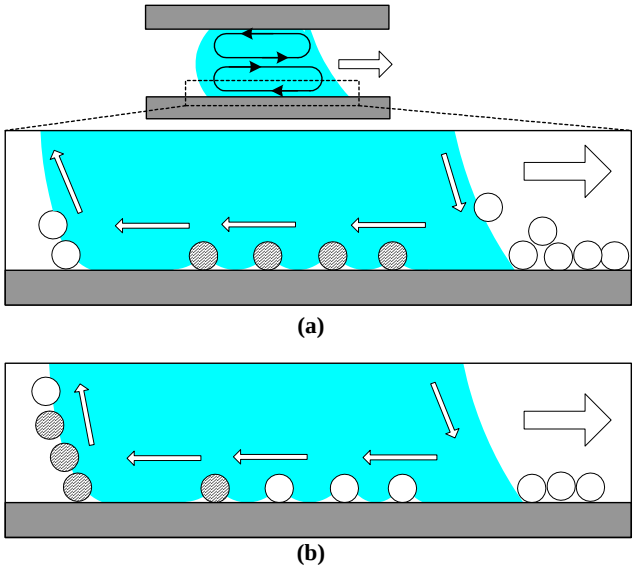

Figure 12. Possible scenario of the super hydrophobic particle interaction with the moving droplet. (a) Fluid motions circulating in clockwise and counter clockwise directions are induced in the lower and upper parts of the droplet, respectively. The particles in the advancing region of the droplet experience the downward flow to the solid surface and are held underneath the droplet since they are super hydrophobic. (b) The particles underneath the droplet reach the receding region of the droplet and then are lifted up by the upward fluid motion.

2.3 DROPLET TRANSPORTATION AND PARTICLE SAMPLING ON A PERFORATED MEMBRANE

Although particle sampling by droplet sweeping was proven very successful on a flat surface, it is challenging to apply the method for micro/nanostructured surfaces on a perforated membrane. More specifically, the question is, can we reliably transport droplets by EWOD on micro/nano-structured surfaces?

Recently, Krupenkin *et al.*[57] incorporated an EWOD electrode into nano-post structures. Then, they showed that the *apparent* contact angle in sessile droplets placed on the nano post surface is significantly decreased when the EWOD electrode is on. However, it turned out this process is unidirectional, not reversible. Once droplet liquid completely wets into the nano-post valleys by EWOD, it does not return to the initial state upon EWOD switched off but remains stuck permanently. Dhindsa *et al.*[58] showed an reversible EWOD actuation of droplet on superhydrophobic carbon nanofibers only if the valleys of the nanofiber forest is filled with liquid (dodecane). When the valleys are filled with air, the irreversibility occurs again. Most recently, Verplanck *et al.*[59] reported an reversible EWOD actuation on an air-filled silicon nanowire forest. The contact angle change is between 160^{o} and 137^{o}, that is, a 23^{o} span. So far, the reversibility of EWOD on structured surfaces has been proven valid only for the very limited configurations. In this regard, the reversibility of EWOD actuation on perforated membranes is analytical studied. The experimental study is also presented including EWOD actuation on the perforated membranes and followed by particle sampling on them.

2.3.1 Theoretical Backgrounds

2.3.1.1 Droplet states on rough surfaces When a small amount of liquid is placed on a rough surface, it forms a droplet whose shape is determined by the liquid volume and the equilibrium contact angle between the liquid and the surface. With the equilibrium contact angle the energy of the system reached a local minimum. If the volume of the droplet is of the order of μL, or less, the gravitational effects have little effect, and the droplet shape is very close to a cap of a sphere.

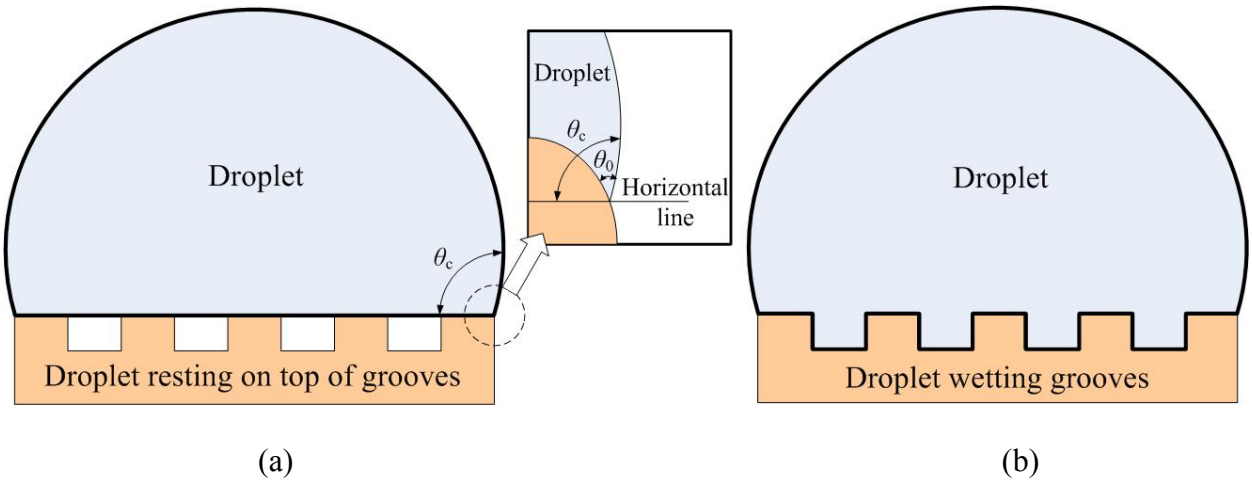

Figure 13. Droplet states on rough surfaces: (a) Cassie state and (b) Wenzel state

The influence of surface roughness on the apparent contact angle of the droplet is generally understood by a study of two theoretically extreme situations. In the Cassie state[60] as shown in Fig 13(a) the droplet base rests on the tips of the roughness elements; consequently the droplet is in composite contact with air and solid at its base. In the Wenzel state[61] as shown in Fig 13(b) the droplet fills the grooves between the roughness elements and is in intimate contact with the solid surface.

In the Cassie state, the apparent contact angle θ_c of such a droplet can be obtained[62] from the energy-minimization principle as

$$\cos\theta_c = -1 + \phi(1 + \cos\theta_0) \tag{6}$$

where ϕ is the fraction of the solid contacting the liquid and the θ_0 is the contact angle of the droplet on a flat surface. In the Wenzel state, the droplet is in intimate contact with the surface features. For such a droplet the apparent contact angle θ_w is similarly obtained [62] as

$$\cos\theta_w = r_m \cos\theta_0 \tag{7}$$

where r_m is the roughness factor defined as the ratio of the total surface area (including the sides and base of the roughness elements) to the projected surface area.

2.3.1.2 The apparent contact angle under EWOD voltage It is well known that a system seeks lower Gibbs free energy states when it becomes stable and in equilibrium. Likewise, a droplet under EWOD actuation seeks minimum energy states. Therefore, energy analysis provides a handy tool in understanding the state transition and its directionality.

In this section an energy-minimization approach can be used to develop expressions for the apparent contact angle of a droplet resting on a rough surface in the presence of an EWOD voltage. The approach consists of estimating the total droplet surface energy as the sum of the solid-liquid and liquid-air interfacial energies. Minimization of the surface energy subject to a constant droplet volume constraint gives the apparent contact angle of the droplet on the electrowetted rough surface. The dimensions of the droplet are such that the effect of gravity is neglected. The droplet assumes the shape of a truncated sphere.

The total droplet surface energy at the constant temperature and pressure for the idealized surfaces substrate can be described by the interfacial energy as follows[63]:

$$E = \gamma^0_{\mathrm{LA}}(A^{\mathrm{LA}} - A^{\mathrm{SL}}\cos\theta_0) \tag{8}$$

where γ^0_{LA} is the liquid-air interfacial tension, A the interfacial area and θ_0 the intrinsic contact angle. Superscripts LA and SL refer to the liquid-air and solid-liquid interfaces, respectively.

For a Cassie droplet the total droplet surface energy can be expressed as

$$\begin{aligned} E &= \gamma^0_{\mathrm{LA}}(A^{\mathrm{LA}} - A^{\mathrm{SL}}\cos\theta_0) \\ &= \gamma^0_{\mathrm{LA}}\{[A_{\mathrm{LA}} + A_{\mathrm{SL}}(1-\phi)] - \phi A_{\mathrm{SL}}\cos\theta_0\} \\ &= [A_{\mathrm{LA}} + A_{\mathrm{SL}}(1-\phi)]\gamma^0_{\mathrm{LA}} + \phi A_{\mathrm{SL}}(-\gamma^0_{\mathrm{LA}}\cos\theta_0) \\ &= [A_{\mathrm{LA}} + A_{\mathrm{SL}}(1-\phi)]\gamma^0_{\mathrm{LA}} + \phi A_{\mathrm{SL}}(\gamma^0_{\mathrm{SL}} - \gamma^0_{\mathrm{SA}}) \end{aligned} \tag{9}$$

where

$$A_{\mathrm{LA}} = 2\pi R^2(1-\cos\theta) \tag{10}$$

and

$$A_{\mathrm{SL}} = \pi R^2 \sin^2\theta \tag{11}$$

A_{LA} and A_{SL} are the apparent liquid - air and solid - liquid interfacial areas, respectively, and γ^0_{SL} and γ^0_{SA} are the solid-liquid and solid-air interfacial energies, respectively. R is the Cassie droplet of radius and θ is the apparent contact angle.

EWOD affects the surface energy content of the droplet by lowering the solid-liquid interfacial energy as predicted by Lippman's equation. The total surface energy E of a Cassie droplet under the application of an EWOD voltage V can be expressed as

$$E = [A_{\mathrm{LA}} + A_{\mathrm{SL}}(1-\phi)]\gamma^0_{\mathrm{LA}} + \phi A_{\mathrm{SL}}(\gamma^0_{\mathrm{SL}} - \gamma^0_{\mathrm{SA}} - \frac{\varepsilon\varepsilon_0 V^2}{2t}) \tag{12}$$

where ε_0 (8.85×10^{-12} F/m) the permittivity of the vacuum, ε the dielectric constant of the dielectric layer, and t the dielectric layer thickness. At the equilibrium, the total surface energy of the droplet is minimized subject to a constant droplet volume constraint:

$$\mathrm{V} = \frac{\pi R^3}{3}(1-\cos\theta)^2(2+\cos\theta) \tag{13}$$

The method of Lagrange multipliers is employed to solve this constrained minimization problem and results in the following equations:

$$\frac{\partial E}{\partial R} = \lambda \frac{\partial \mathrm{V}}{\partial R} \tag{14}$$

$$\frac{\partial E}{\partial \theta} = \lambda \frac{\partial \mathrm{V}}{\partial \theta} \tag{15}$$

where λ is the Lagrange multiplier. Elimination of λ from equations (14) and (15) yields the apparent contact angle of a Cassie drop on an electrowetted surface $\theta^{\mathrm{E}}_{\mathrm{C}}$ as

$$\begin{aligned}\cos\theta_{\mathrm{C}}^{\mathrm{E}} &= -1+\phi\left(1+\frac{(\gamma_{\mathrm{SA}}^0-\gamma_{\mathrm{SL}}^0)}{\gamma_{\mathrm{LA}}^0}+\eta\right)\\ &= -1+\phi(1+\cos\theta_0+\eta)\end{aligned} \tag{16}$$

where η is the electrowetting number expressed as

$$\eta = \frac{\varepsilon\varepsilon_0 V^2}{2t\gamma_{\mathrm{LA}}^0} \tag{17}$$

Substituting the Cassie equation (6) we can write the apparent contact angle as

$$\cos\theta_{\mathrm{C}}^{\mathrm{E}} = \cos\theta_{\mathrm{C}} + \phi\eta \tag{18}$$

A similar procedure can be applied to estimate the apparent contact angle $\theta^{\mathrm{E}}_{\mathrm{W}}$ of a Wenzel drop under an EW voltage as

$$\cos\theta_{\mathrm{W}}^{\mathrm{E}} = r_m(\cos\theta_0+\eta) \tag{19}$$

The dimensionless surface energy E of any droplet of fixed volume V can be expressed solely in terms of apparent contact angle θ_{app} as

$$\frac{E}{(9\pi)^{3/2}\mathrm{V}^{2/3}\gamma_{\mathrm{LA}}^0} = (1-\cos\theta_{\mathrm{app}})^{2/3}(2+\cos\theta_{\mathrm{app}})^{1/3} \tag{20}$$

2.3.2 Analytical study on EWOD reversibility on perforated membrane

2.3.2.1 The apparent contact angle on perforated membrane under EWOD voltage When a droplet is sitting on the perforated membrane the droplet liquid will always exposure to the air from the bottom. Also we assume the thickness of the perforated membrane is neglected compare to the size of the droplet. So the droplet will play as the Cassie drop status. The apparent contact angle on the perforated membrane under EWOD voltage will be similar to eq(16) by using opening ratio (β=1-ϕ) instead of ϕ:

$$\cos\theta_C^E = -1 + (1-\beta)(1+\cos\theta_0 + \eta) \tag{21}$$

Similarly we can rewrite the eq(18) as

$$\cos\theta_C^E = \cos\theta_C + (1-\beta)\eta = \cos\theta_C + (1-\beta)\frac{\varepsilon\varepsilon_0 V^2}{2t\gamma_{LA}^0} \tag{22}$$

It can be seen that equation (22) is otherwise identical to eq (3), but that the Young angle has been replaced by the initial contact angle of the Cassie drop, and there is the opening ratio β in the voltage term. If (1-β)<<1, namely $\beta \to 1$, the electrowetting effect (contact angle change) is much weaker on the highly opening ratio surface than on normal surfaces.

2.3.2.2 The drop surface energy on perforated membrane under EWOD voltage It can be seen from Eq (22) that the apparent contact angle on the perforated membrane will be monotonically decreased by applying the EWOD voltage. From eq (20) we can also easily see that the dimensionless energy E is monotonically increasing with the apparent contact angle. So the surface energy will be monotonically decreased when the voltage gradually applied to the

droplet and there has no energy barrier during this process. This suggests that the EWOD actuation on the perforated membrane is highly reversible.

On the contrary irreversible EWOD actuation on the Nanostructured Surfaces reported by other group[57] has different structure compared with the perforated membrane. At the post structures when the EW voltage is applied the droplet will eventually in contact with the solid bottom which change the Cassie drop to the Wenzel drop. Based on the calculation from Bahadur et al[64], there always a energy jump for electrowetted Cassie-Wenzel transition. The energy will be needed to excite the drop from Wenzel state to Cassie state.

2.3.3 Experimental results and discussion

To realize the droplet based particle sampling on perforated membranes, four generation of devices are fabricated. The reversible EWOD actuation is tested and followed by the particle sampling on them.

2.3.3.1 1st generation devices 1st generation devices were made using a commercially available filter membrane that has a rectangular array of perforated holes (60 μm × 128 μm hole area, 20% opening ratio) as shown in Fig 15. The goal was to demonstrate the reversible operation of liquid droplets on a perforated membrane by EWOD and particle sampling on the membrane by EWOD-actuated moving droplets. Part of the results were presented at the MicroTAS2006 conference in Tokyo, Japan[65].

Figure 14 shows a configuration for fundamental EWOD operation testing with a sessile droplet on a perforated structure. A commercially available filter membrane that has a rectangular array of perforated holes (60 μm × 128 μm hole area, 20% opening ratio) is first

passivated by a parylene layer and then coated with a Cr/Au layer for the EWOD electrode. For the EWOD dielectric layer, another parylene layer is deposited, followed by a Teflon layer. For grounding, a sharp tip is penetrated into the droplet. Under electrical potential (165 VAC, 1 kHz) applied, the contact angle is changed from 120° to 60° (Fig. 14(b)). Also, the top views (Fig. 14(b)) confirm corresponding droplet spreading. This 60° angle change was shown highly reversible and repeatable, and is large enough to guarantee reliable droplet transportations with patterned electrodes [9, 28, 36]. From the section 2.3.1.1 the apparent contact angle on the Teflon coated 20% opening ratio mesh without EW voltage should be around 124° which is similar to the experiment data (120°). Based on the calculation with 2um parylene and 2000 Å Teflon layer, 130V voltage can bring the contact angle down to 60°. However during the experiment the higher voltage (165V) is applied to make the contact angle change to 60°, this probably caused by the well known contact angle saturation.

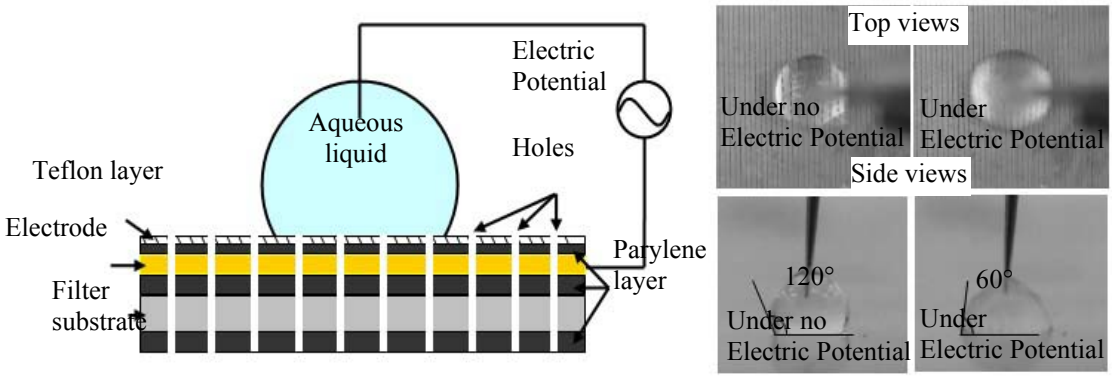

Figure 14. Reversible EWOD operations with a sessile droplet on a *perforated* filter membrane: (a) Configuration of EWOD actuations. The volume of the droplet is about 5 μl. The filter membrane (hole size 60 μm × 128 μm, see Fig. 3 for hole geometry) is coated with a Parylene layer (10 μm) for passivation, Cr (100Å)/Au (1000Å) metal layers for EWOD electrodes, another Parylene layer (2 μm) for EWOD dielectric, and a Teflon layer (2000Å) for hydrophobic layer; (b) Contact angle is reversibly and repeatedly changed from 120° to 60°.

To test droplet transportation and particle sampling, testing devices are fabricated (Fig.15) that mainly consists of a perforated filter membrane and a transparent top plate.

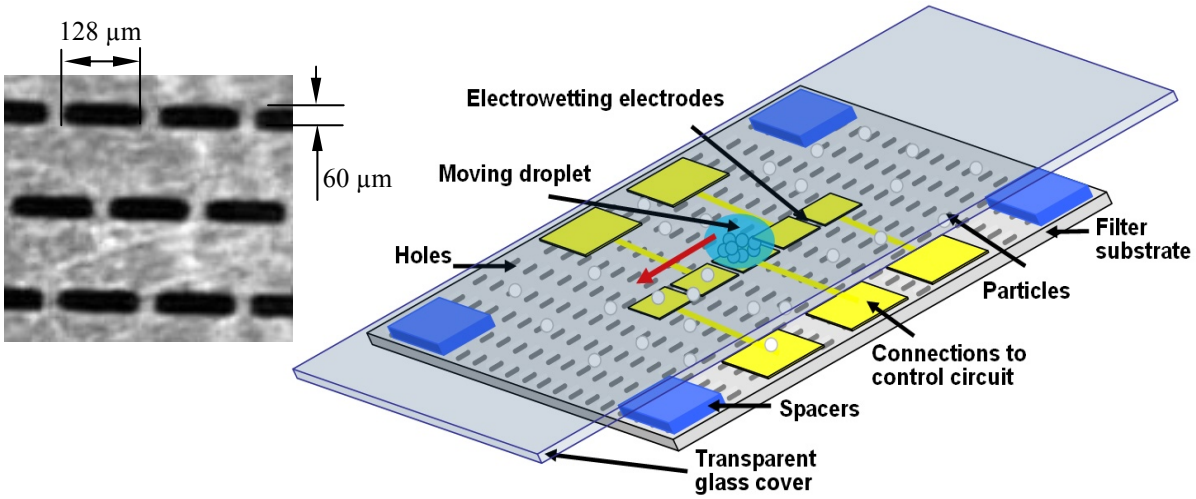

Figure 15. Testing devices for particle sampling (not to scale). A linear array of square electrodes is patterned on the filter membrane. The transparent top plate is covered with an Indium Tin Oxide (ITO, 1000Å) layer for EWOD grounding and a Teflon layer (2000Å).

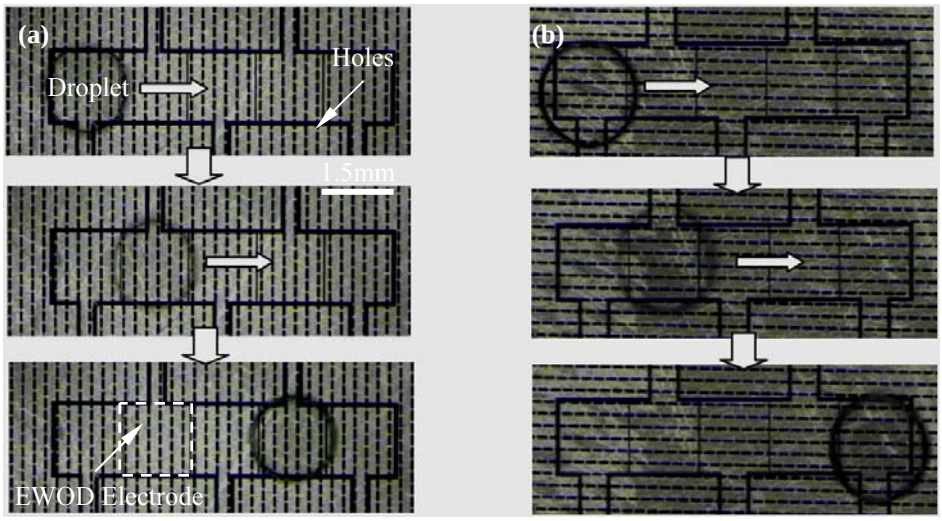

Figure 16. Sequential pictures of successful EWOD droplet transportations on a perforated filter membrane. Sequential activations of the electrodes make droplets move right, perpendicularly (a) as well as in parallel (b) to the hole pattern line.

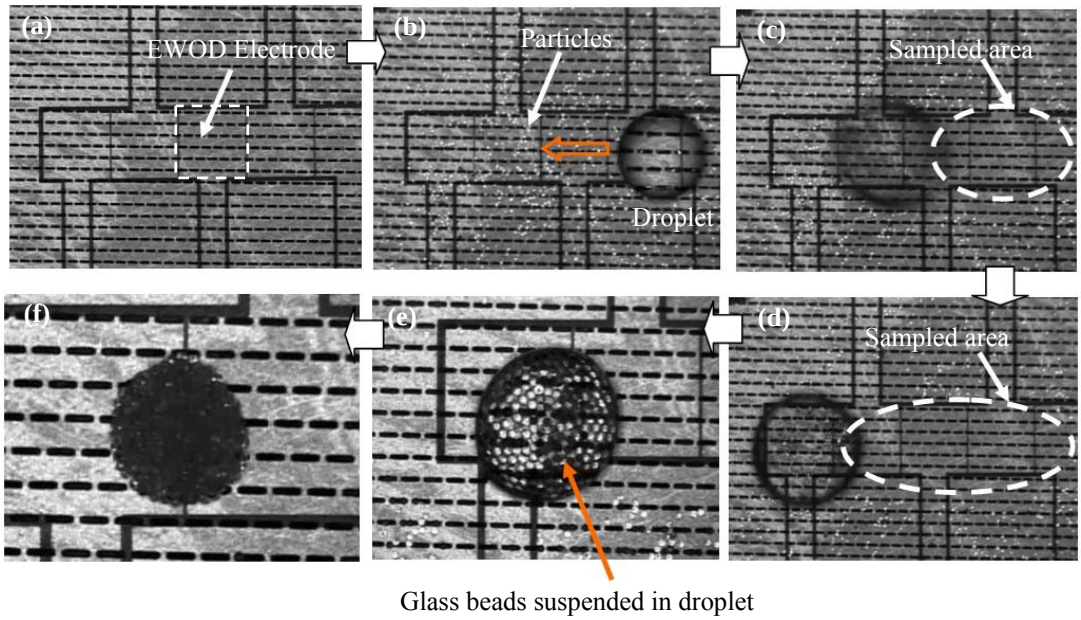

Figure 17. Sequential pictures of glass beads sampling viewed through the transparent top glass plate: (a) The filter membrane without particles; (b) glass beads (white dots, 80 μm diameter) and a droplet are deposited on the perforated membrane. Note that the droplet looks smaller than those in Figs. 17(c-d) since it is not sandwiched yet by the top plate; (c-d) the droplet moves left when the EWOD electrodes are activated sequentially to the left. Glass beads are picked up by the moving droplet. After the droplet passes, the membrane surface becomes clean with no bead left behind; (e) Collected beads are suspended in the droplet (close-up view). Note that the top plate is removed to enhance evaporation; (f) Beads pile up after the water droplet is completely evaporated (close-up view).

The membrane structure is the same as that in Fig. 14(a), except a linear array of square electrodes (1.5×1.5 mm^2) are patterned for EWOD droplet transportations. The ground electrode (Indium Tin Oxide layer) for EWOD entirely covering the top plate is coated with a Teflon layer. Sequential activations of the patterned electrodes generate continuous movements of the droplet perpendicular (Fig. 16(a)) as well as parallel (Fig. 16(b)) to the hole pattern line, implying that droplets may move in any directions on the current membrane regardless of hole arranging pattern.

Finally, particle sampling is tested with hundreds of glass beads (80 μm in diameter) deposited on the membrane (Fig. 17(b)). A droplet moves from the right to the left along the electrodes, simultaneously sweeping and sampling the particles into the droplet (Figs. 17(c-d)). It is seen that no particle remains on the path where the droplet has previously passed (Figs. 17(c-d)). Finally, the sampled particles are suspended inside the droplet (Figs. 17(d-e)). The sampled particles can pile up by completely evaporating the water droplet (Fig. 17(f)).

2.3.3.2 2nd generation devices For the 1st generation devices both filter holes and particles tested were limited to the pretty large dimension (~ 100 μm), making the sampling method impractical. Considering that airborne target particles typically range in several microns in size, in this section, we microfabricated 2nd generation filters of several-μm sized holes and examined them with 8-μm particles, targeting for practical airborne particle sampling.

Shown in Fig. 18a-c are detailed fabrication steps of the microfabricated perforated filter membrane embedded with an EWOD electrode array. The filter membrane was made of the low-stress Si_xN_y layer (3000 Å) deposited on a Si wafer (500 μm). After backside KOH etching, a Si_xN_y and Si membrane of 50 μm thickness was left suspended. The filter holes on the membrane were opened by a reative ion etching (RIE) process followed by another KOH etching to comepletely remove the remaining Si in the membrane (Fig. 18a).

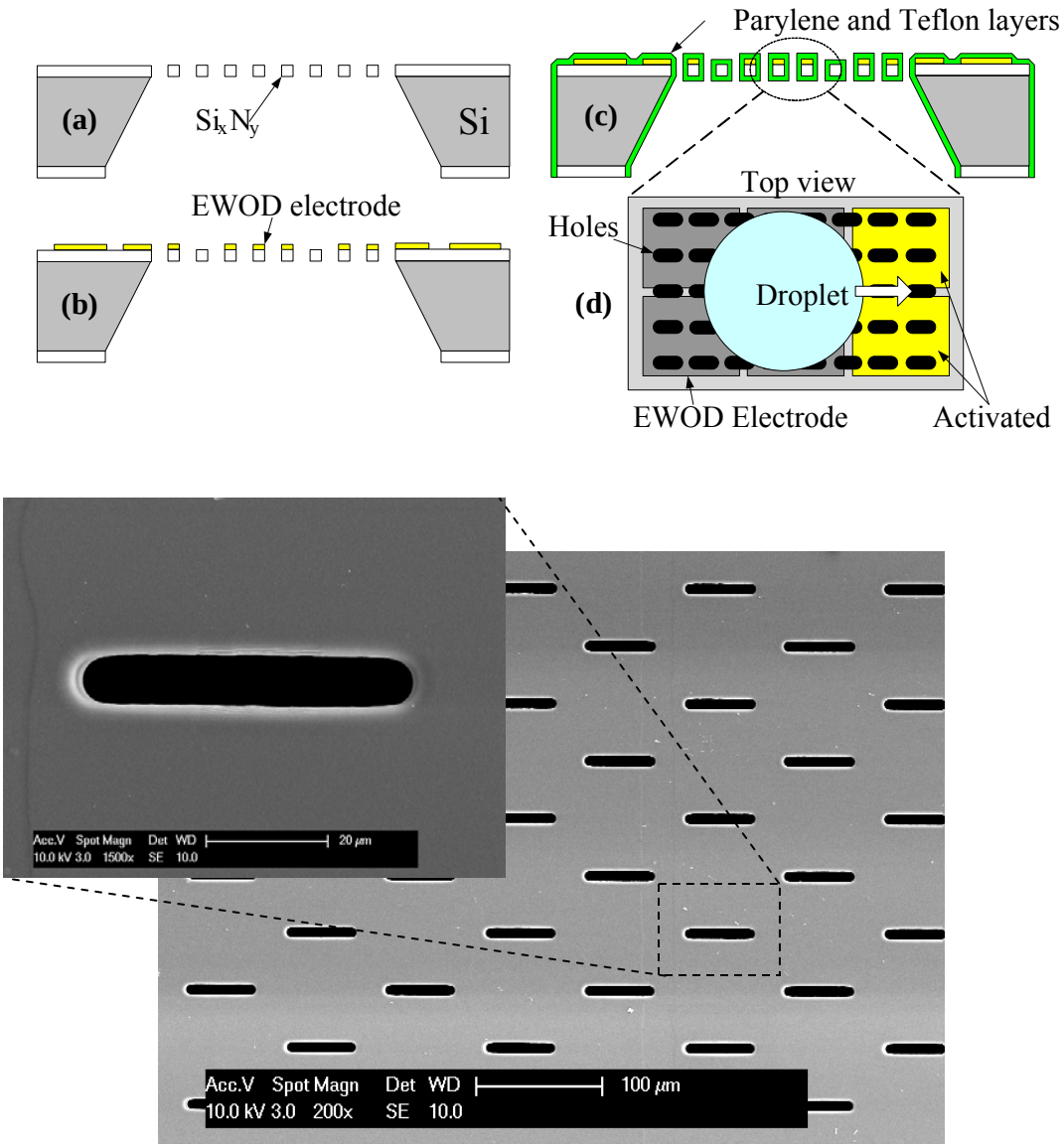

Figure 18. Fabrication steps (not to scale) of micro filter membrane embedded with arrayed EWOD electrodes and perspective view of testing devices: (a) The low stress Si_xN_y membrane is fabricated by KOH backside etching. Filter holes are opened by RIE etching, (b) A gold layer (1000 Å) along with a Cr seed layer (100 Å) is sequentially deposited on the membrane and patterned. (c) A parylene layer (1 or 3 μm thick) is deposited on the membrane followed by a 100 Å thick teflon layer. (d) Configuration of droplet on the electrodes. (e) The SEM picture of filter 1

For the linear array of EWOD electrodes, a gold layer (1000 Å) along with a Cr seed layer (100 Å) was deposited by an E-beam evaporator and patterned by wet etching (Fig. 18b). Then a parylene layer (1 or 3 μm thick) is conformally coated on the membrane structure using a chemical vapor deposition process. Finally, a 100 Å thick teflon layer was spin-coated to make the surface hydrophobic (Fig. 18c). A scanning electron microscopy (SEM) image of perforated filter membrane is shown in Fig. 18e. In this fabrication process, the most difficult part is pattern the electrode on the released the membrane. Cause the photoresist is easily getting into the hole of the membrane the exposure condition is going to very critical. Sometimes need to over exposure to make sure the photoresist accumulated in the hole can be finally developed.

Three different kinds of membrane designs were fabricated with different hole shape, size and opening ratio (ratio of the hole area to the total area): filter 1 (rounded rectangle hole of 48 μm × 6 μm, opening area ratio of 5 %); filter 2 (rounded rectangle hole of 24 μm × 6 μm, opening area ratio of 20 %); filter 3 (circular hole of 8-μm dia., opening area ratio of 9 %).

Figure 19a shows a configuration for fundamental EWOD operation testing with a sessile droplet on a perforated structure. In this case, the electrode underneath the droplet was not patterned but covered the entire area of the droplet base. For grounding, a sharp tip is penetrated into the droplet. Similary to the 1st generation device, the reversible EWOD operations were observed on the microfabricated membranes. A sessile droplet was first put on the membrane of design 1 (rounded rectangle hole of 48 μm × 6 μm). As shown in Fig. 19b, under the electric potential (130 V_{AC}, 1 kHz), the contact angle was also switched back and forth between 120° and 60°. Likewise, revesibile contact angle change of 60^{o} was observed as well in filters 2 and 3 (data not shown). This highly reversible and repeatable 60° angle change is large enough to guarantee reliable droplet transportations with patterned electrodes.

In the meantime, these results confirm the reversible EWOD actuations as described in the previous section. For example, from the section 2.3.1.1 the apparent contact angle on the Teflon coated 5% opening ratio mesh without EW voltage should be around 119° which is similar to the experiment data (120°). Based on the calculation with 3um parylene and 100 Å Teflon layer, around 125V voltage can bring the contact angle down to 60° which is also similar to the experiment data (60°).

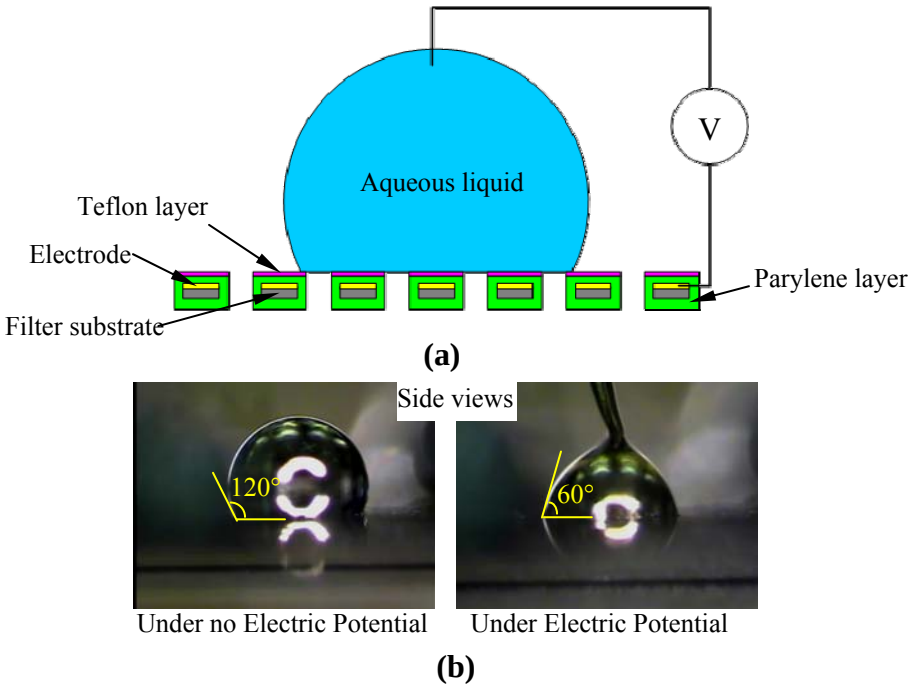

Figure 19. Reversible EWOD operations with a sessile droplet on a perforated filter membrane: (a) Configuration of EWOD actuations. The volume of the droplet is about 5 µl. The filter membrane is embedded with an electrode covering the entire area of droplet base. A sharp tip is penetrated into the droplet, serving as a ground; (b) On filter 1 (hole size 48 µm × 6 µm): the contact angle is also reversibly and repeatedly changed from 120º to 60º on the filter membrane under 130 V_{AC}, 1 kHz.

For testing of droplet transportation and particle sampling, the perforated filter membranes were integrated with a transparent top plate with a gap in between. The entire area of the top plate is covered with an indium tin oxide layer and a 2000 Å Teflon layer, serving as a ground electrode for EWOD actuation.

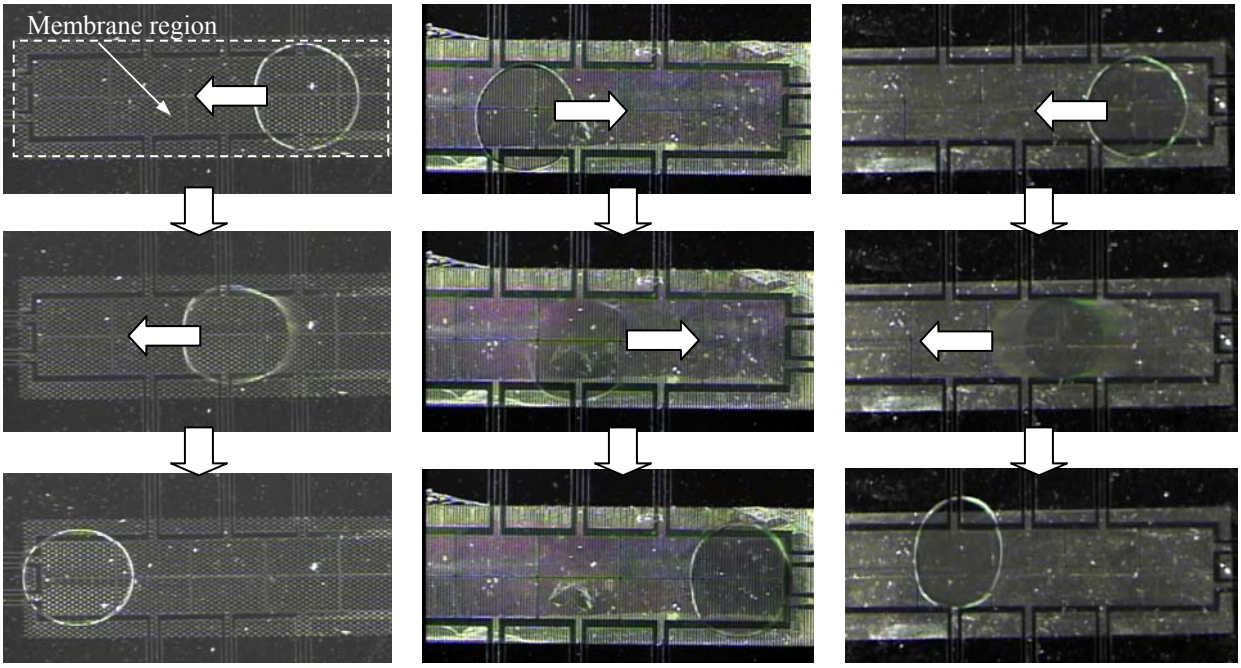

Figure 20. Sequential pictures of successful EWOD droplet transportations on perforated filter membranes (viewed through the transparent top glass plate). (a) filter 1 (rounded rectangle hole of 48 μm × 6 μm, opening area ratio of 5 %); (b) filter 2 (rounded rectangle hole of 24 μm × 6 μm, opening area ratio of 20 %); (c) filter 3 (circular hole of 8-μm dia., opening area ratio of 9 %).

For the microfabricated membranes, droplet transportation was examined. As shown in Fig. 20a-c, droplets are easily transported on all the three microfilter designs. In these experiments, the applied voltage was 120 V_{AC} for filters 1 (Fig. 20a) and 3 (Fig. 20c) and 70 V_{AC} for filter 2 (Fig. 20b). EWOD transportation can be made in a wide range of the holes shape,

arrangement, and size, at least in the current membrane conditions, thus promising the versatility and robustness of the current droplet sampling for wide applications.

Particle sampling was examined for the microfabricated filters using two different types of particles: borosilicate glass particles (7.9-μm in diameter, 9000 series, Duke Scientific Inc.) and 8-μm polystyrene particles (DRI-CAL, Duke Scientific Co.). These two types are almost the same in size but different in the contact angle on the particle surface. In the literature, the contact angle of the borosilicate particle is found to be around 14º[66] while the polystyrene particle is around 66º[67]. The borosilicate glass particles can be a model for highly hydrophilic particles while the polystyrene particle for intermediate hydrophilic particles.

The glass particles are examined on filter 1, as demonstrated in sequentially captured pictures in Fig. 21. A large number of the glass particles are initially deposited on the filter membrane with a uniform distribution. For this deposition, an indirect method was used as follows. Before depositing the particles on the testing filter membrane, they were first deposited on a plastic dummy membrane. Then tapping the dummy membrane over the testing membrane make the particles detached from the dummy membrane and land on the filter membrane with a uniform distribution. After a droplet (~ 500 nanoliters in volume) was in place, the top cover was pressed against the spacers (Fig. 21a). By sequentially activating the driving electrodes from the right to the left (130 V_{AC}, 1 kHz), the droplet moves along the line path, simultaneously sweeping and sampling the particles into the droplet (Fig. 21b and c). The path on which the droplet has passed becomes clear, indicating that very few particles remain on the path. Finally, we can see that the sampled particles are suspended inside the droplet (Fig. 21d).

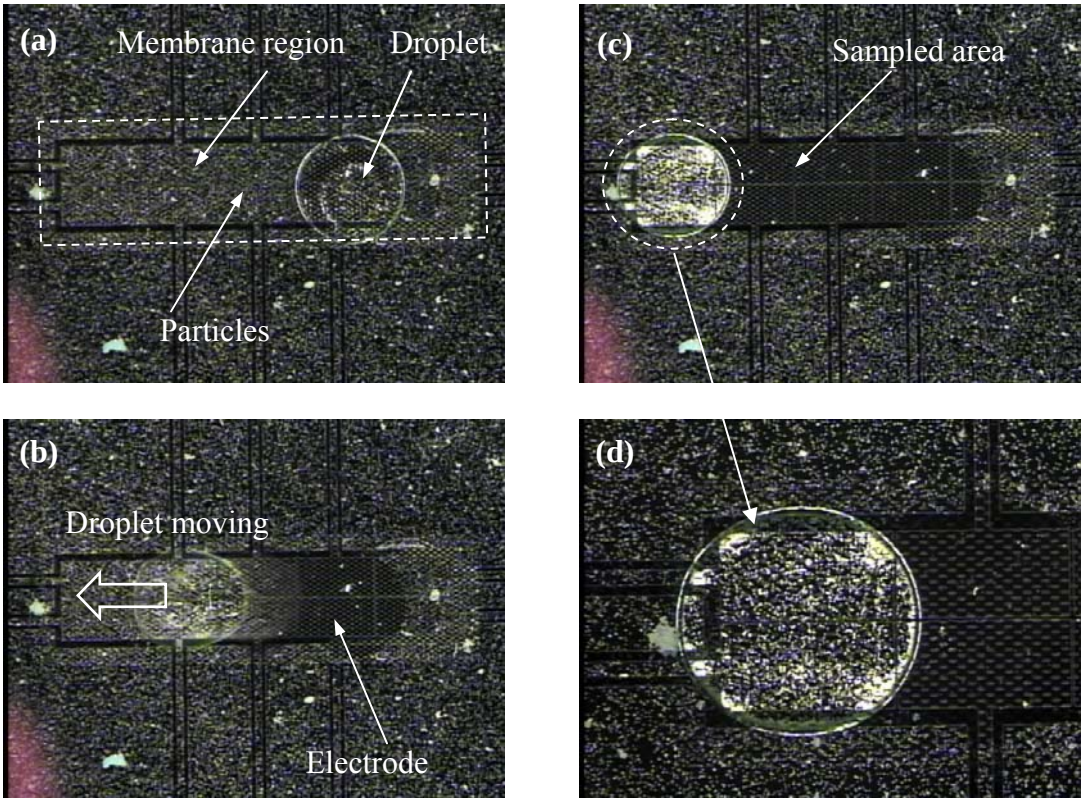

Figure 21. Sequential pictures of glass particle sampling: (a) Glass particles (white dots, 7.9-μm dia.) and a droplet are deposited on the perforated membrane. (b, c) the droplet moves left when the EWOD electrodes are sequentially activated to the left. The glass particles are picked up by the moving droplet. After the droplet passes, the membrane surface becomes clean (not frosted) with no particle left behind. (d) Sampled particles are suspended in the droplet (close-up view).

Furthermore, the other microfabricated filter designs were examined, as the final states after droplet sweeping are shown in Fig. 22.

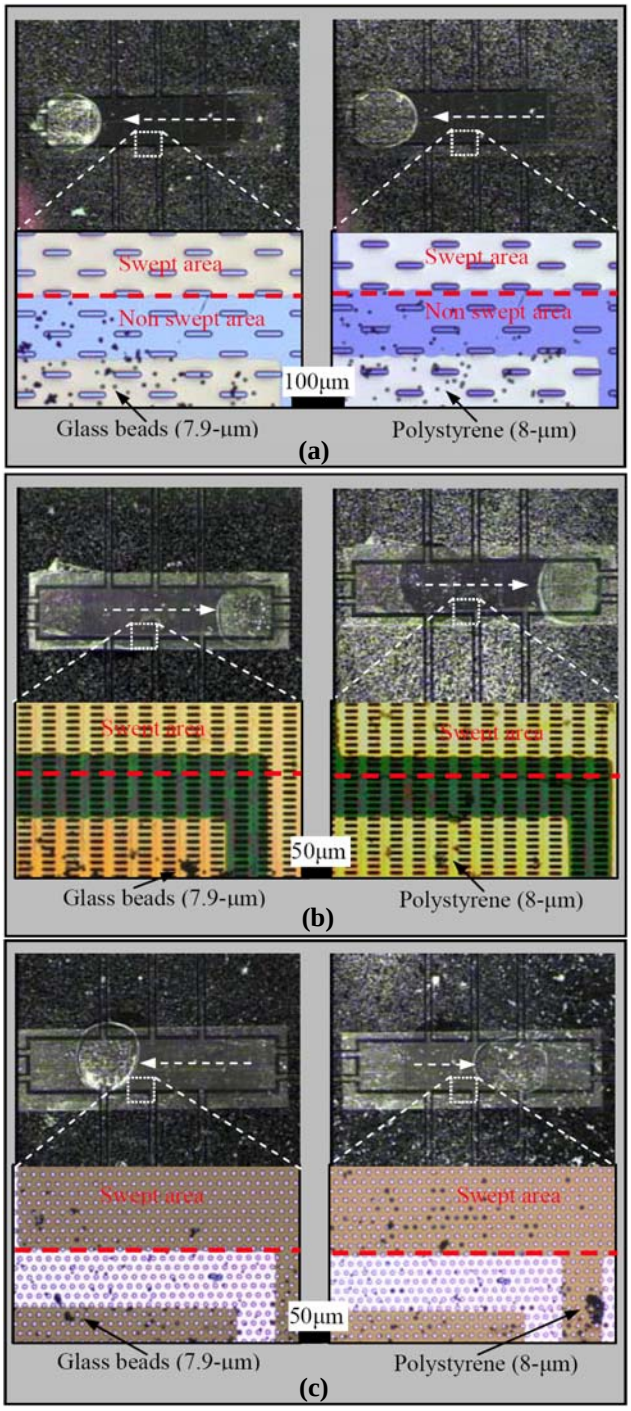

Figure 22. Sampling results for the different filter designs examined with two types of particles (7.9-μm glass and 8-μm polystyrene particles): (a) Filter 1 (rounded rectangle hole of 48 μm × 6 μm, opening area ratio of 5 %); (b) Filter 2 (rounded rectangle hole of 24 μm × 6 μm, opening area ratio of 20 %); (c) Filter 3 (circular hole of 8-μm dia., opening area ratio of 9 %). The upper part of the dotted lines denotes droplet-swept regions while the lower part indicates non-swept regions.

We can see that almost all the glass particles are sampled into the droplet in all the three filter designs whereas some polystyrene particles are not sampled still remaining on the droplet swept path, especially on filters 2 (right in Fig. 22b) and 3 (right in Fig. 22c). Although the polystyrene particles were initially deposited uniformly on the membrane surface, most of the unsampled particles were found near or in the hole areas after droplet sweeping. This suggests that during the droplet sweeping process, some polystyrene particles were pushed to and likely trapped in the hole area. In this case it seems to be more difficult to remove the trapped polystyrene particles out of the hole areas. On the contrary, the glass particles show high sampling performance, no matter whether they are initially deposited in the hole areas or on the flat surface area. The adhesion force between the particle and the meniscus of the droplet is highly dependent on the contact angle on the particle surface. The lower contact angle is, the higher the adhesion force[68]. That is why the glass particles can be easily sampled into the droplet although they are trapped into the filter holes.

In order to quantify the sampling efficiency for each case two areas are taken along the edge of droplet footprint. One is from where the droplet swept and the other from where the droplet did not. Using the 'touch count' function in an image analysis software (analySIS® FIVE), the number of particles m in the droplet swept area and the number of particles n in the non swept area were manually counted. Then, the sampling efficiency η is defined and calculated according to $\eta = (n - m)/n$. For particle clusters, the total particle number was roughly estimated based on the cluster area. To minimize any marked deviation from the true values in the sampling efficiency, this procedure was repeated in ten different spots and the sampling efficiency was averaged out. The averaged sampling efficiency for each case is shown in Table 2.

Table 2. Sampling efficiency for the three filter designs

Particle	Contact angle With water (degree)	Sampling efficiency (%)		
		Filter 1	Filter 2	Filter 3
Glass	14	99.5	98.7	95.9
Polystyrene	66	93.9	87.2	86.4

Overall all the three microfabricated filters show high sampling efficiencies (over 95 % for glass beads and over 86% for polystyrene beads). Compared to the sampling efficiencies on the solid surface[69] (98.7 % for 7.9-μm glass beads and 93.3 % for 8-μm polystyrene beads), for the glass particles the sampling efficiencies on the perforated filter membranes are as high as that on the solid surface. However, for the polystyrene particles, the sampling efficiencies are slightly lower than that on the solid surface, more or less depending on the hole design.

In this section, micro particle sampling on perforated micro filter membranes are demonstrated using EWOD (electrowetting on dielectric) actuated droplet sweeping. Three different microfabricated filters varying the hole shape (rounded rectangle and circular holes), size (≥ 6 μm) and opening ratio (5 %, 9 % and 20 %) were embedded with a linear array of EWOD electrodes. On all the four perforated filters, first we achieved and demostrated reversible EWOD actuations using sessile droplets. Also, we achieved reliable EWOD droplet transportations along a linear path on the perforated membranes by sequentially activating the array of electrodes. For particle sampling, the microfilter membranes were examined against two

different types of particles: 7.9-μm diameter glass particles (surface contact angle ~ 14º) and 8-μm diameter polystyrene particles (surface contact angle ~ 70º). Initially these particles were uniformly deposited on the filter membranes using an indirect method. When a droplet was transported along a predefined path by EWOD, particles on the path are successfully picked up and sampled into the EWOD-actuated moving droplets. For both types of the particles, sampling efficiencies were quantified using a particle counting method, showing over 95 % for 7.9-μm glass particles and over 85 % for 8-μm polystyrene particles for all the micro filters. The present particle sampling method can be easily fully automated and requires an extremely small amount of liquid volume (several droplets of about 500 nanoliters each). Thus it will be highly compatible and easily integrated with lab-on-a-chip systems for downstream biological/chemical analyses.

2.3.3.3 3rd generation devices In the course of developing the envisioned system above, we have demonstrated successful particle sweeping on a flat surface [70, 71]as well as perforated surface (opening ratio < 20%)[72, 73] using EWOD-actuated droplet. In this system, however, the power consumption is of main concern, particularly in air suction process in this system. For the previous system we reported, the filters opening ratio is less than 20% which will lead higher pressure drop through the filter and need more power supply. To reduce the pressure drop and the power requirement, the larger opening ratio of the filter is needed. However based on the calculation from section 2.3.2.1, if the opening ratio $\beta \to 1$ the electrowetting effect (contact angle change) is much weaker on the highly opening ratio surface than on normal surfaces. Even the EWOD actuation is reversible, without highly contact angle change it will not guarantee reliable droplet transportations with patterned electrodes [9, 28, 36].

The goal of 3rd generation device is to investigate the reversibility of EWOD actuation in highly opened meshes which opening ratio is over about 50%, followed by droplet transportation on it. Two different kinds of commercially available meshes have been examined for the EWOD reversibility. Both of them are embedded with an array of electrodes for EWOD actuation.

Different designs of testing device were fabricated based on two kinds of commercially available meshes (Mesh 1: Thin Metal Parts LLC, Colorado Springs, CO and Mesh 2: Precision Eforming LLC, Cortland, NY), as shown in Fig 23. Since the commercial meshes were electrically conductive, they were first passivated by a parylene layer (Fig. 23a). In order to examine droplet transportation, a linear EWOD electrode array was then embedded into each mesh type. Fabrication steps are: depositing and pattering Cr (100 Å)/Au (3000 Å) layers (Fig. 23b); and depositing parylene (1 μm) and Teflon layers (100 Å) (Fig. 23c). The final step is to place a transparent glass coated with an ITO layer over the electrode-embedded mesh with

spacers in between. The top view of the fabricated testing device is shown in Fig. 23d along with a close-up view near the gap between adjacent electrodes.

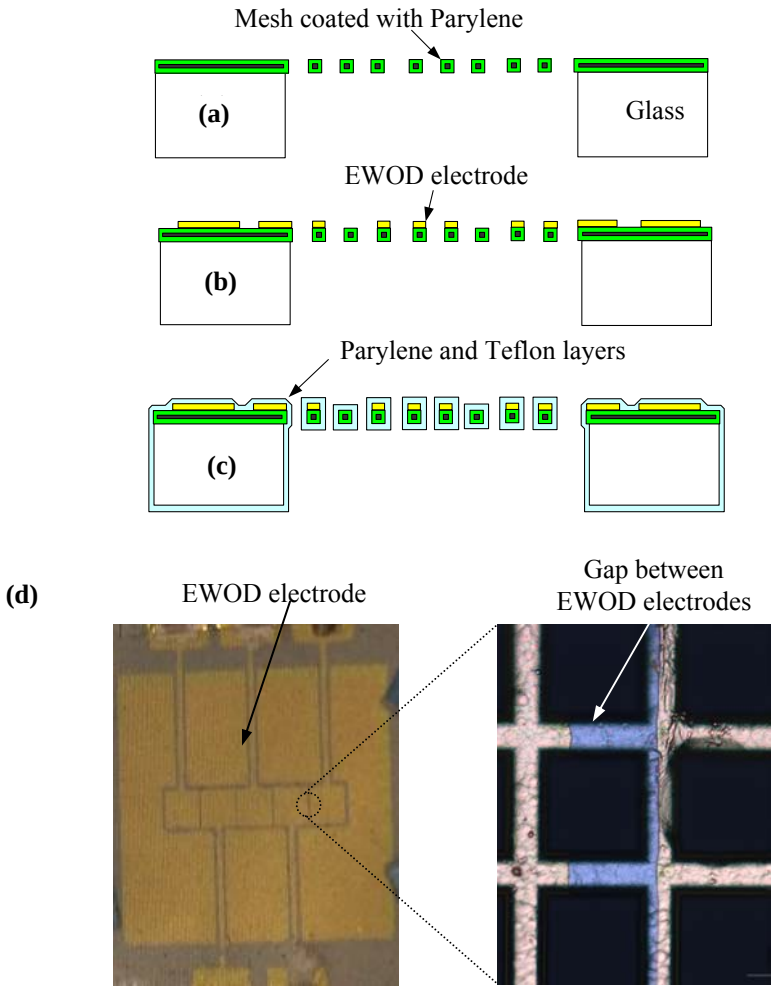

Figure 23. (a-c) Fabrication of filter membrane embedded with EWOD electrodes and (d) Top and close-up views of testing devices: (a) The nickel mesh coated with a parylene layer (1 μm thick) was bonded on a glass substrate; (b) A gold layer (1000 Å) along with a Cr seed layer (100 Å) was sequentially deposited on the membrane and patterned; (c) Another parylene layer (1 μm thick) and a 100 Å thick teflon layer were sequentially deposited; (d) top view of the fabricated testing device and close-up view in the gap area (shown in blue) between adjacent EWOD electrodes.

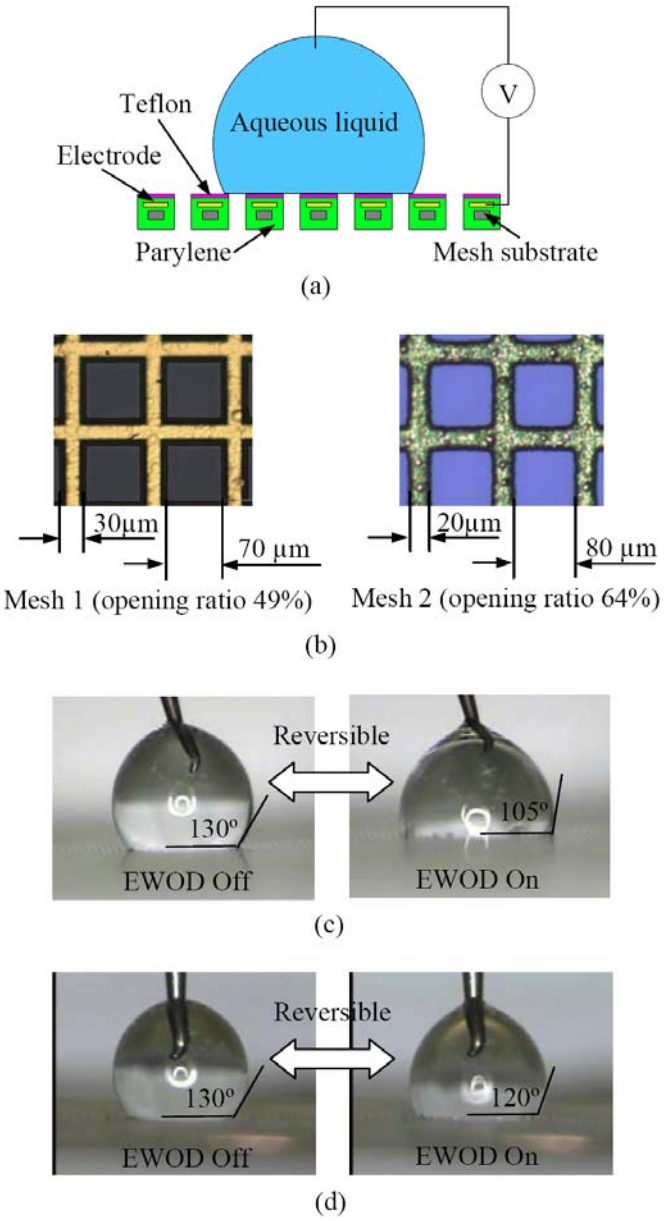

Figure 24. Reversible EWOD operations of a sessile droplet sitting on a micro filter mesh: (a) Configuration of EWOD actuations. The micro filter mesh is embedded with an EWOD electrode covering the entire area of bubble base. A sharp tip is penetrated into the droplet, serving as a ground; (b) Mesh geometry (Mesh 1: 49 % opening ratio and 30 μm thick, Mesh 2: 64 % opening ratio and 5 μm thick); (c) on Mesh 1, the contact angle is reversibly and repeatedly changed between 130º and 105º; (d) On Mesh 2, the contact angle is reversibly and repeatedly changed between 130º and 120º. Note that in both cases the applied voltage is 90 V (1 kHz).

Two different kinds of meshes were fabricated with different hole size, mesh thickness and opening ratio (ratio of the hole area to the total area): mesh 1 (70 μm × 70 μm square, 30 μm thick, opening area ratio of 49 %); mesh 2 (80 μm × 80 μm square, 5 μm thick, opening area ratio of 64 %).

Figure 24(a) shows a configuration for fundamental EWOD operation testing with a sessile droplet on a perforated structure. In this case, the electrode underneath the droplet was not patterned but covered the entire area of the droplet base. For grounding, a sharp tip is penetrated into the droplet. An electrical potential (90 VAC, 1 kHz) applied between the tip and electrode repeatedly was switched on and off to see the reversibility. Figure 24b shows a close view of the two meshes: mesh 1 (70 μm × 70 μm square, 30 μm thick, opening area ratio of 49 %); mesh 2 (80 μm × 80 μm square, 5 μm thick, opening area ratio of 64 %). As shown in Fig. 24c, on the mesh 1 we observed reversible EWOD actuations with a contact angle change between 130° and 105°. This 25° angle change was shown highly reversible and repeatable. This highly reversible and repeatable 25° angle change is enough to guarantee reliable droplet transportations with patterned electrodes, as detailed in the next section. On the other hand, we only observed 10° reversible EWOD actuations with a contact angle change between 130° and 120° on mesh 2. Even though this 10° angle change is reversible and repeatable, it is not large enough to guarantee the reliable droplet transportations. In addition to the AC signal, we also observed similar contact angle changes with DC voltage applied.

In the meantime, these results confirm the reversible EWOD actuations as described in the previous section. For example, from the section 2.3.1.1 the apparent contact angle on the Teflon coated 49% opening ratio mesh without EW voltage should be around 136° which is similar to the experiment data (130°). Based on the calculation with 1μm parylene and 100 Å

Teflon layer, around 90V voltage can bring the contact angle down to 87° which is much smaller than the experiment data (105°).This may be caused by the contact angle saturation. For an au layer coated with 1 μm parylene and 100Å Teflon, the contact angle saturation normally occur at 70V and above. Recalculate the contact angle change under 70V applied potential, it shows that the contact will decrease to 105° which is as same as the experiment data (105°).

On the other hand, based on the calculation the apparent contact angle on the Teflon coated 64% opening ratio mesh without EW voltage should be around 143° which is much higher than the experiment data (130°). This maybe caused by the mesh 2 substrate is flexible and after embedded with an array of electrodes the chip surface is not flat as mesh 1. Considering the contact angle saturation, under 70V the contact angle can decrease to 118° which is similar to the experiment data (120°).

For testing of droplet transportation, the fabricated meshes were integrated with a transparent top plate with a gap in between. The entire area of the top plate is covered with an indium tin oxide layer and a 2000 Å Teflon layer, serving as a ground electrode for EWOD actuation.

Figure 25 shows sequentially captured images of successful droplet transportation on Mesh 1 (viewed through the transparent top glass plate). The droplet moves to the left step by step, as the electrodes are sequentially activated one by one to the left. Then, the droplet moves back to the initial position when the EWOD electrodes are activated to the right. The applied voltage is 90 V (1 kHz). With this repeatable droplet transportation on the high opening ratio mesh (49%) results, it is highly possible to realize the particle capturing and sampling into the droplet on this highly-opened micro filter meshes.

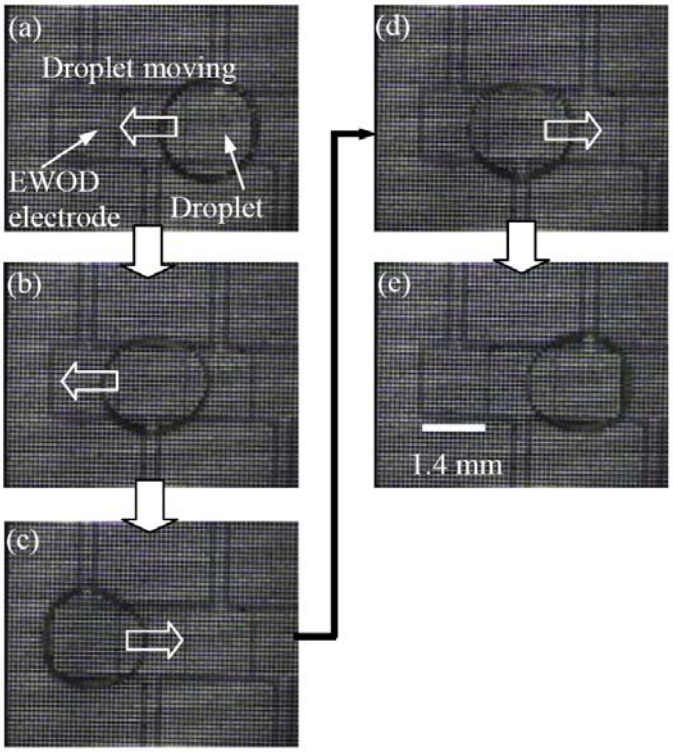

Figure 25. Sequential pictures of successful droplet transportation by EWOD on Mesh 1: (a-c) the droplet moves left when the EWOD electrodes are sequentially activated to the left one by one. (c-e) the droplet moves back to the initial position when the EWOD electrodes are sequentially activated to the right.

On Mesh 2, however, the droplet could not be transported (not shown here). This is because the contact angle change (10° in Fig. 3d) is not large enough.

In this section, droplet transportation on the perforated meshes with high open ratio is demonstrated. Two commercial meshes varying the hole size (70 μm × 70 μm square and 80 μm × 80 μm square), thickness (30 μm and 5 μm) and opening ratio (49 % and 64 %) were embedded with a linear array of EWOD electrodes. On both of the perforated meshes, first we achieved and demonstrated reversible EWOD actuations using sessile droplets. Also, we achieved reliable EWOD droplet transportations along a linear path on the perforated meshes

(open ratio 49%) by sequentially activating the array of electrodes. On the other hand the droplet transportations could be realized on the perforated meshes (open ratio 64%) in this configuration.

In summary, the opening ratio limit for successful EWOD operations is around 50% for the present mesh configuration. In our previous work, the opening ratio was less than 20%[72, 73]. In this work we achieve 30% increase in opening ratio. This can entail more than 85% reduction in power requirement for the air suction process, based on the correlation for the pressure drop through filter holes[74].

With this repeatable droplet transportation on the high opening ratio mesh results, it is highly possible to realize the particle capturing and sampling into the droplet on this highly-opened micro filter meshes.

2.3.3.4 4th generation devices Cause the commercial mesh size and opening ratio is limited, it is necessary to fabricate the higher opening ratio mesh by using the microfabrication method. The goal of 4th generation device is to investigate the reversibility of EWOD actuation in ultra-high opened meshes which opening ratio is about 90%, followed by droplet transportation on it. Eight different kinds of meshes (the opening ratio is from 20% to 90%) have been fabricated. All of them are embedded with an array of electrodes for EWOD actuation.

The design of 4th generation meshes is shown in Fig 26. The dark area in the design is the hole on the mesh and the white area is the frame of the mesh. The distance *d* represents the size of the hole and the *t* represents the thickness of the frame. The design parameter of each mesh is shown in table 3.

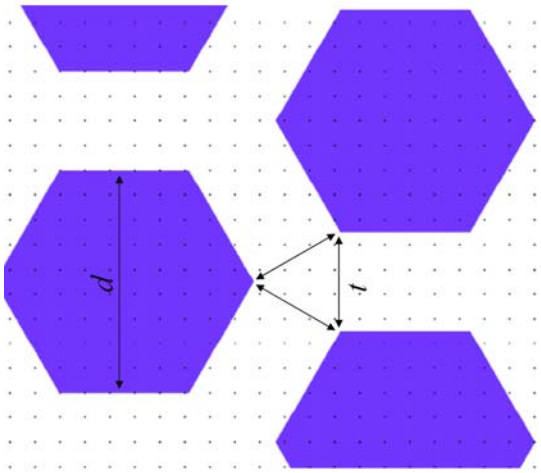

Figure 26. The design of 4th generation meshes

Table 3. The parameter of 4th generation filter designs

Design	*d* (μm)	*t* (μm)	Parylene thickness (μm)	Opening ratio
1	6	9.6	1	20%
2	6	6.8	1	30%
3	6	5	1	40%
4	6	4	1	50%
5	9	4	1	60%
6	14	4	1	70%
7	25	4	1	80%
8	55	4	1	90%

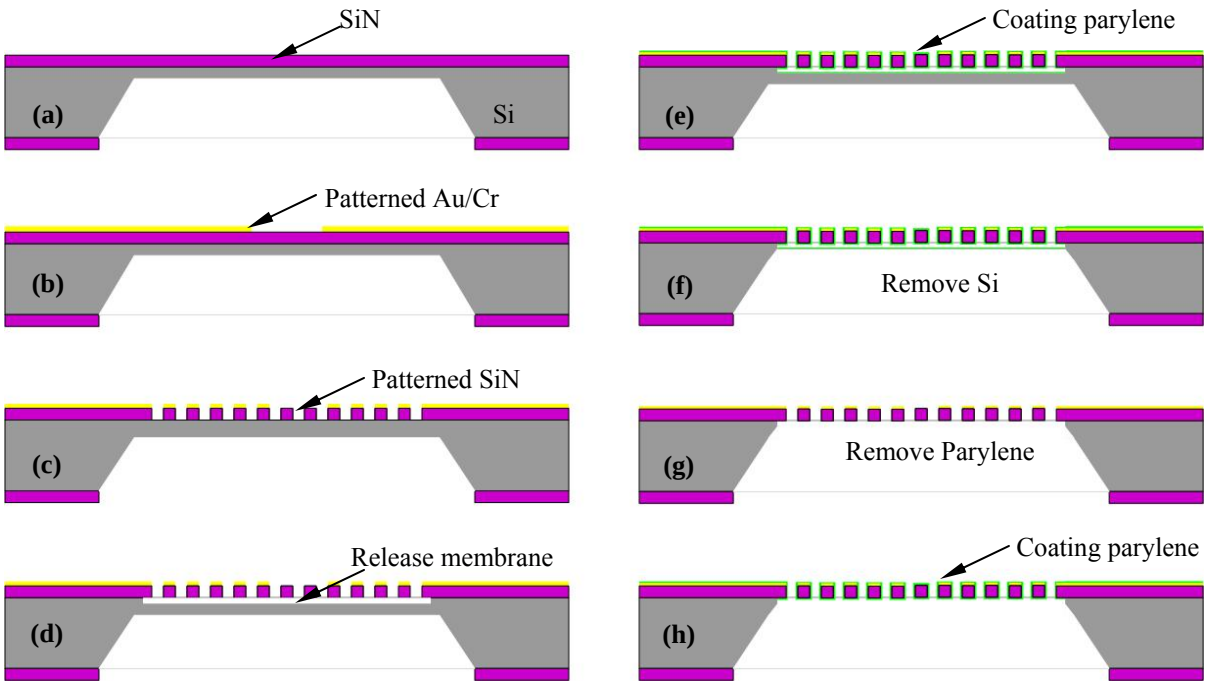

Figure 27. Fabrication steps (not to scale) of micro filter membrane embedded with arrayed EWOD electrodes: (a) The low stress Si_xN_y membrane coated wafer is fabricated by KOH backside etching and 50 μm thick Si is left on the back. (b) A gold layer (1000 Å) along with a Cr seed layer (100 Å) is sequentially deposited on the membrane and patterned. (c) The Si_xN_y membrane is patterned on the front side and etched by RIE. (d) The membrane is released by XeF_2. (e) a conformal parylene coating is applied on the membrane. (f) The Si on the back of the membrane is removed by XeF_2. (g) All the parylene layer is removed by RIE. (h) another parylene layer with 1 μm thick is coated on the membrane.

Shown in Fig. 27a-h are detailed fabrication steps of the microfabricated perforated filter membrane embedded with an EWOD electrode array. The filter membrane was made of the low-stress SixNy layer (3000 Å) deposited on a Si wafer (500 μm). After backside KOH etching, a SixNy and Si membrane of 50 μm thickness was left suspended. For the linear array of EWOD electrodes, a gold layer (1000 Å) along with a Cr seed layer (100 Å) was sputtered and patterned by wet etching (Fig. 27b). The filter holes on the membrane were opened by a reative ion etching

(RIE) process followed by XeF2 etching to release the membrane of the wafer (Fig. 27c,d). Then a parylene layer (1μm thick) is conformally coated on the membrane structure using a chemical vapor deposition process. Then the Si is totally removed by XeF_2 etching. By using the RIE all the parylene layer is removed and finally, another parylene layer (1μm thick) is coated on the filter membrane. The reason to introduce the XeF2 to release the membrane instead of KOH wet etching is this dry etching process will avoids the sticking issues during the wet release process. The final step should be coating the Teflon layer, but the spin coat technique is not suitable for this thin frame (4 μm) mesh. The vapor type of Teflon coating process is needed.

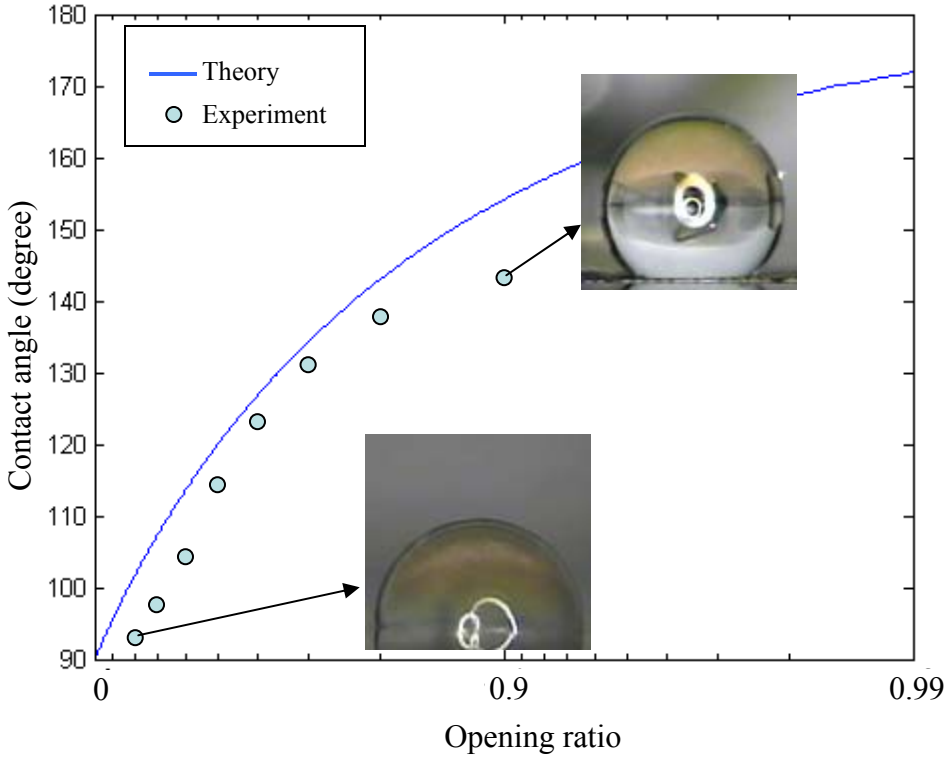

Figure 28. The Cassie state droplet contact angle on parylene mesh

For the current state, the author just finished the parylene coating process without coating the Teflon layer. And the contact angle of Cassie state drop on the parylene mesh is measured and compared with the theory state, as shown in Fig 28. The experiment data is lower than the theory data, this due to the fabricated mesh has some residue around the frame which make the opening ratio is smaller than the design parameter. Cause no Teflon layer is deposited on the mesh, the EWOD actuation test is not performed. For the future if we can coat Teflon layer on the mesh the EWOD reversibility will be tested and the limitation for successful EWOD operation will be investigated.

2.3.4 Summery

In this section, the reversibility of EWOD actuation on perforated membranes is analytical studied. It has been shown that the droplet on the perforated membrane is always under the Cassie state and always has the reversibility under the EWOD actuation. If the opening ratio is close to one, the electrowetting effect (contact angle change) is much weaker on the highly opening ratio surface than on normal surfaces.

To realize the droplet based particle sampling on perforated membranes, four generation of devices are fabricated. For the opening ratio less than 20% meshes, the reversible EWOD actuation is tested and successful particle sampling on the mesh is realized. For the opening ratio around 50% meshes, the reversible EWOD actuation and droplet transportation is presented. With this repeatable droplet transportation on the high opening ratio mesh results, it is highly possible to realize the particle capturing and sampling into the droplet on this highly-opened micro filter meshes. For the ultra-high opening ratio (~90%) meshes, the fabrication process is introduced and the Cassie state contact angle is measured and compared with analytical solution.

2.4 CONCLUSION

In this chapter, a novel particle sampling system is reported which can be highly compatible and easily integrated with the lab-on-a-chip system.

We demonstrated that different kinds of particles can be successfully sampled from solid surface with the high efficiency, while droplets are driven along a programmed path by electrowetting principle. Also present the droplet transportation and particle sampling on the perforated membrane with theoretically study.

The present sampling technique provides many advantages: (1) highly compatible with lab-on-a-chip systems, droplet-based (or digital) as well as continuous flow systems, (2) extremely small amount of liquid volume required (a single droplet of nano/pico liters), thereby not necessarily requiring additional concentration steps in analyses, (2) no external pressure source required for liquid sweeping, (3) simple design and fabrication since no mechanical moving structure is associated, (4) high sampling efficiency, perhaps with extremely small particles since surface tension which is dominant in micro/nano scale is harnessed, (5) extremely low power consumption for droplet actuations, and (6) robust and reliable operations.

3.0 MICROPARTICLE SEPARATION BY DROPLET MICROFLUIDICS

There are currently high demands for means to efficiently manipulate and discriminate bio entities in microfluidics [75, 76]. To date, numerous systems have been developed to meet these demands. Most of them are based on continuous flows which basically require complicated micro channel networks, consequently often raising the cost of design and fabrication and lowering the reliability of operation. Recently, in the mean time, digital (droplet-based) microfluidics [28, 29, 71, 77, 78] (in particular, operated by electrowetting-on-dielectric, or EWOD) successfully demonstrated various fluidic operations, obviating the above drawbacks in many cases. A large number of minute droplets can be manipulated (created, transported, split, and mixed) individually and in parallel on a two-dimensional platform, with no need to build any micro channel structures. Furthermore, all of these operations can be accomplished under digital control from a programmable controller, promising tremendous potential for reconfigurable chemical and biologic analysis [30].

However, the implementation of bio-sample concentration and separation into digital microfluidics is still challenging since most of the previously developed concentration and separation methods essentially rely on long micro channels (e.g., micro capillary electrophoresis). Therefore, simply adopting the conventional concentration and separation methods into digital microfluidics requires constructing microchannel networks, as a result deteriorating the original strength of digital microfluidics. Most recently, with a motivation to

realize concentration and separation in digital microfluidics without microchannels, Cho and Kim [79] presented a particle separation and concentration method by using electrophoresis in a droplet configuration. However, this technique works only with electrically charged particles, restricting its application scope.

On the contrary, dielectrophoresis (DEP) [80] accesses a wide range of particle characteristics such as conductivity and permittivity by changing the frequency of the applied electric field or by using different suspending media. Most importantly, in DEP particle separations, particles to be separated need no charge treatments. It has been demonstrated that various solid particles and biological particles such as cells, virus, DNA and macromolecules can be separated by using differential DEP affinity separation [81-89]. In this case, one fraction of particles experiences negative DEP and moves towards local field minima at the center of, or between, electrodes while the other fraction is trapped by positive DEP at electrode edges. Dielectrophoretic forces can often be combined with hydrodynamic forces in a separation method known as dielectrophoresis-field flow fractionation (DEP-FFF). In DEP-FFF, particles are carried along the device by pumped liquid and separated by a perpendicular DEP force according to a combination of their effective polarizability and density. A number of groups have successfully applied DEP-FFF to particle separations [90-95]. However, DEP-FFF also requires an external pumping source along with microchannels to generate a horizontal continuous flow.

Meanwhile, if a micro particle is subjected to a moving electric field, instead of a stationary electric field, then under appropriate conditions the particle can also be moved by the effect known as travelling wave dielectrophoresis (twDEP) [83, 96-99]. In twDEP, long distance transportations of various particles can be achieved with no need to pump liquid along the device in order to produce horizontal motions in particles. Therefore, this principle has currently been

developed into a comprehensive technique for manipulating and separating various particles and cells [100-103]. However, most of them have also been dedicated for continuous flow streams, not for droplet configurations.

In this section, we develop an in-droplet concentration and separation method by implementing the principle of twDEP to droplet-based digital microfluidics which is operated by the EWOD principle. This method enables concentrating and separating of micro particles in droplet configurations with no need for micro channel networks. Furthermore, this method does not necessarily require any charge treatments on the particles. The first task in this paper is to characterize the dielectrophoretic properties of particles to be separated and concentrated under a well-established electric field generated from polynomial electrodes [104]. These characterizations allow us to optimize the frequency of the applied twDEP signal and the conductivity of the medium for successful in-droplet separation and concentration. Then, after testing devices were designed and fabricated, they were examined for in-droplet particle separation for two cases where particles of two different kinds were initially mixed. Also, in-droplet concentration was tested using a droplet containing single type particles. In order to quantify the concentration and separation efficiency, the number of particles was measured before and after operations of in-droplet separation and concentration using a direct particle counting method. The notion of this separation and concentration method using twDEP and its preliminary results have been previously reported in the MEMS 2007 conference and the Hilton Head 2006 workshop [105, 106].

3.1 CONCEPT

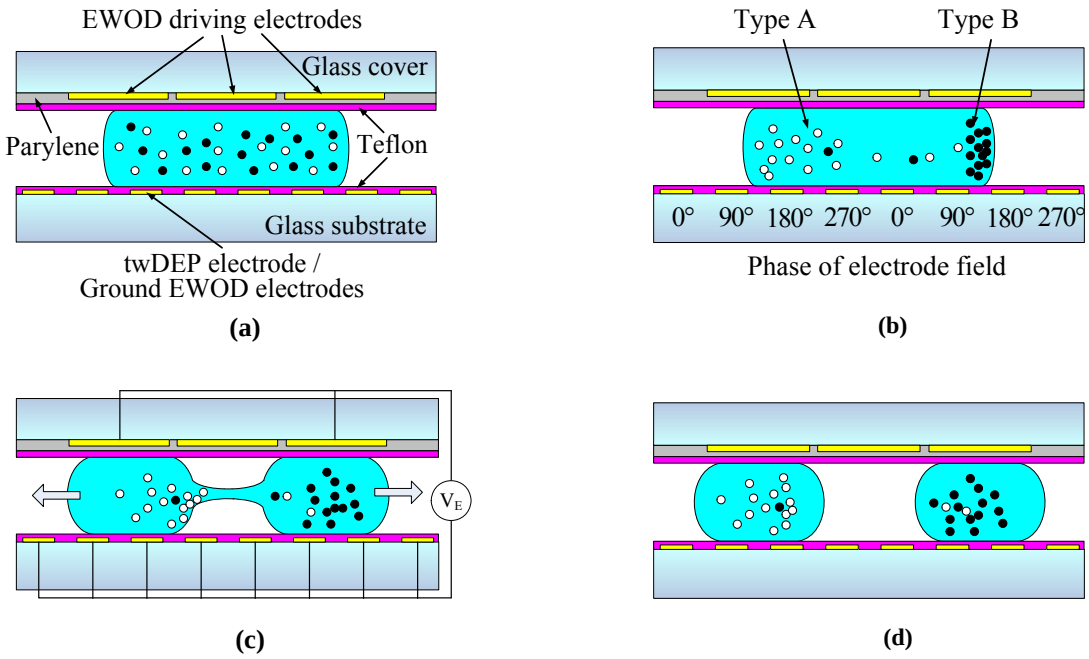

Figure 29. In-droplet particle separation procedures by twDEP and EWOD: (a) A droplet containing mixed particles is placed between two parallel plates; (b) under twDEP generated by the bottom electrodes, particles of type B (black) are transported and concentrated on the right side while particles of type A (white) in the left side; (c) under EWOD, the droplet is split into two daughter droplets. The two electrodes on the top plate are activated with the twDEP electrodes on the bottom plate grounded; (d) finally two types of particles are separated into two respective daughter droplets.

In the present in-droplet separation and concentration, two main microfluidic operations are incorporated: particle transportation by twDEP and droplet splitting by EWOD. Figure 29 illustrates sequential procedures for an ideal case of the present in-droplet particle separation by twDEP and EWOD: (1) initial state with a droplet containing mixed particles of two different types (e.g., types A and B, Fig. 29(a)); (2) transport type B particles (shown in black) and type A particles (shown in white) into the right and left edges, respectively, of the droplet by twDEP

(Fig. 29(b)); (3) split the mother droplet into two daughter droplets by EWOD (Fig. 29(c)). This step corresponds to an extracting process permanently isolating targets into a single droplet, thereby significantly minimizing particle dispersion after twDEP separation; (4) final state (Fig. 29(d)). As a result, type B particles are concentrated in the right daughter droplet while type A particles are concentrated in the left droplet. For twDEP particle separation, a traveling electric field is generated by activating the electrodes on the bottom plate with a continuous phase shift of 90^{o} between adjacent electrodes. For EWOD droplet splitting, the left and right electrodes on the top plate are simultaneously activated to elongate and split the droplet (Fig. 29(c)). In this splitting process, all of the twDEP electrodes on the bottom plate serve as signal grounding.

The concentration of single type particles is similar to but simpler than the separation procedure. If a mother droplet has only one type of particle, twDEP transports the particles to the droplet edge, followed by droplet splitting. Finally, one split daughter droplet has a higher particle concentration than the other.

The present concentration and separation scheme provides several significant and unique advantages. First, the twDEP actuation can be easily and directly interfaced with conventional electronics without building additional mechanical structures. Thus, it is highly compatible with EWOD-actuated chips and ultimately with the digital microfluidic lab-on-a-chip system which mainly consists of an array of electrodes. Second, the splitting step immediately follows the particle separation or concentration so that the dispersion of separated or concentrated particles by thermal diffusion or unwanted flows can be minimized. By simply switching electric connections from twDEP actuation to EWOD actuation, particles can be quickly extracted and secured in daughter droplets with minimal dispersion. Third, two fluidic operations (i.e., separation and concentration) can be performed in the same device without adding any

physically or electrically supplemental components. For the concentration unit, one can simply use a droplet with a single type of particle in the same device, rather than multiple types of particles.

3.2 TRAVELLING WAVE DIELECTROPHORESIS

Of the two main operations (particle transportation and droplet splitting) used in the in-droplet separation and concentration, droplet splitting is relatively well developed as we have previously discovered and reported a criterion for successful droplet splitting in which the channel gap and the droplet size should meet particular conditions [77]. Therefore, this section discusses particle transportation using twDEP.

When a spherical particle is placed under a spatially and temporally varying AC electric field $\overline{E}$, the time-averaged DEP force $\langle \overline{F}(t) \rangle$ acting on the particle can be given by [107]:

$$\langle \overline{F}(t) \rangle = \pi \varepsilon_m r^3 [\mathrm{Re}(f_{CM}(\omega)) \nabla |\overline{E}|^2 - 2\,\mathrm{Im}(f_{CM}(\omega))(\nabla \times (\mathrm{Re}(\overline{E}) \times \mathrm{Im}(\overline{E}))], \tag{23}$$

where ε_m is the permittivity of the suspending medium, ω the angular frequency of the electric field, r the particle radius, ∇ the del operator, $f_{\mathrm{CM}}(\omega)$ the Clausius-Mossotti factor, and $\mathrm{Re}(f_{\mathrm{CM}}(\omega))$ and $\mathrm{Im}(f_{\mathrm{CM}}(\omega))$ the real and imaginary parts of the factor $f_{\mathrm{CM}}(\omega)$, respectively. The Clausius-Mossotti factor $f_{\mathrm{CM}}(\omega)$ in Eq. (23) is given by

$$f_{CM}(\omega) = \frac{\varepsilon_p^*(\omega) - \varepsilon_m^*(\omega)}{\varepsilon_p^*(\omega) + 2\varepsilon_m^*(\omega)}, \tag{24}$$

where ε_p^* and ε_m^* are the frequency-dependent complex permittivities of the particle and its suspending medium, respectively. The complex permittivity of each material depends on its dielectric constant ε and electrical conductivity σ and takes the form $\varepsilon^* = \varepsilon - j\sigma/\omega$, where $j = \sqrt{-1}$.

In equation (23), we can see that the force acting on a polarized particle in the non-uniform AC electric field has two contributions: one is from the first term in the bracket of eq. (23) which represents a product between the real part of the Clausius-Mossotti factor $\mathrm{Re}(f_{CM}(\omega))$ and the spatial non-uniformity of the applied field magnitude squares. This term, which is identified by Pohl [80], directs the particle towards the strong or the weak field regions, depending upon whether $\mathrm{Re}(f_{CM}(\omega))$ is positive or negative. For example, when $\mathrm{Re}(f_{CM}(\omega)) > 0$ the particle is attracted to the high electric field region (electrode edges in many cases) while when $\mathrm{Re}(f_{CM}(\omega)) < 0$ the particle is repelled from the high electric field region. The former is called positive dielectrophoresis (pDEP) and the latter called negative dielectrophoresis (nDEP).

The other contribution is from the second term in the bracket in eq. (23), which is related to the imaginary component of the Clasusius-Mossotti factor $\mathrm{Im}(f_{CM}(\omega))$ and the spatial non-uniformity of the electric field phases. Depending on the sign of $\mathrm{Im}(f_{CM}(\omega))$, this force term exerts the particle towards the regions where the phases of the field component become larger ($\mathrm{Im}(f_{CM}(\omega)) > 0$) or smaller ($\mathrm{Im}(f_{CM}(\omega)) < 0$). For example, when an array of parallel planar microelectrodes is energized with sequentially phase-shifted AC voltages, a travelling electric field is produced, as shown in Fig. 2. At an appropriate frequency and medium conductivity, polarizable particles are levitated above the electrode under a negative DEP force (that is, $\mathrm{Re}(f_{CM}(\omega)) < 0$). This force is balanced by a gravitational force F_g. The levitated particles can also move horizontally either left or right along the electrode array. If $\mathrm{Im}(f_{CM}(\omega)) < 0$ (co-field), the particle would move in the same direction as the travelling electric field (white particle in Fig.

2). On the contrary, if Im($f_{CM}(\omega)$) > 0 (contra-field), the particle would move opposite to the travelling electric field (black particle in Fig. 30).

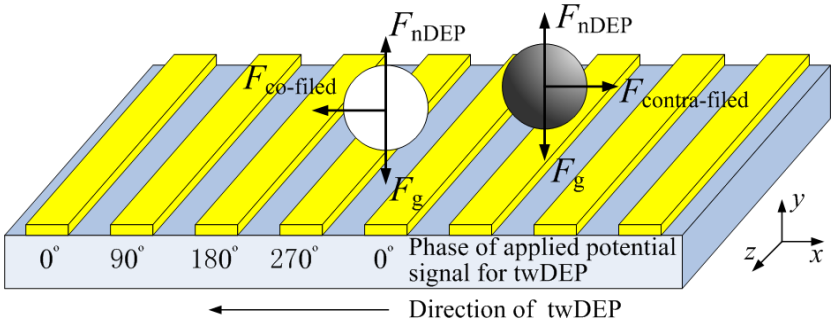

Figure 30. Travelling wave dielectrophoresis (twDEP) using an electrode array for particle separation. The numbers show the phase of the input signal applied to the electrodes.

The twDEP particle separation utilizes the opposite motions of particles. By properly changing parameters associated with the Clausius-Mossotti factor such as the applied frequency, and conductivities and permittivities of particles and their suspending media, two different types of particles can be move opposite to each other and thus separated (i.e., one type of particle is set in the condition of Im($f_{CM}(\omega)$) > 0 and the other type of particle in the condition of Im($f_{CM}(\omega)$) < 0, or vice versa). Among the associated parameters, the applied frequency and the conductivity of medium can be controlled more easily than the others.

3.3 DIELECTROPHORESIS (DEP) AND ELECTROROTATION (ROT) SPECTRA MEASUREMENTS OF PARTICLES

For higher separation efficiency of different particle types, the associated parameters, in particular, the frequency of the applied signal and the conductivity of the medium, should be properly adjusted. These parameters can be optimally determined by way of measuring the dielectrophoretic (DEP) and electrorotation (ROT) spectra of particles in the frequency domain.

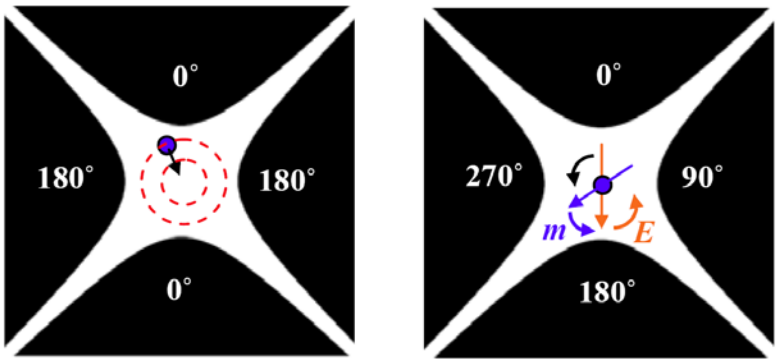

(a) (b)

Figure 31. The polynomial electrodes for DEP and ROT spectra measurements: (a) The moving velocity is measured for DEP spectra while a particle is moving between two dotted circles. (b) The rotation speed and direction is measured for ROT spectra while a particle is being held and rotated in the center between the electrodes. The number on each electrode denotes the phase of the applied signal.

Huang *et al* [104] described an experimental method to measure the spectra of DEP and ROT for a single particle using the 2nd order polynomial electrode designs (Fig. 31) of which electric field is well defined. Note in Fig. 31 that the number on each electrode represents the phase of the applied AC signal. By measuring the velocity of particle travelling along a predefined path (e.g., from the edge of the electrode to the center in case of nDEP or the other

way in case of pDEP), the DEP spectra can be indirectly inferred (Fig. 31(a)). In this particle motion, the DEP force on the particle is balanced with the viscous drag force, resulting in a linear relationship between $V^2\mathrm{Re}(f_{CM}(\omega))$ and the particle moving speed, where V is the applied peak-peak voltage across the electrodes. In this paper, this procedure was used to infer $\mathrm{Re}(f_{CM}(\omega))$ (or DEP spectra) in the frequency domain for two different medium conductivities.

Using the same polynomial electrode designs, a rotation electric field can be produced. This electric field induces a dipole moment m on a particle held in the center between the electrodes (Fig. 31(b)). The interaction between the dipole moment and the rotation electric field generates a torque on the particles, eventually resulting in particle rotation. Here, the particle rotating speed is also linearly proportional to $-V^2\mathrm{Im}(f_{CM}(\omega))$ and the rotating direction is correlated with the sign of $\mathrm{Im}(f_{CM}(\omega)$. That is, the same rotation direction of particle as the electric field indicates $\mathrm{Im}(f_{CM}(\omega)) < 0$ (co-field) while the opposite particle rotation indicates $\mathrm{Im}(f_{CM}(\omega)) > 0$ (contra-field). In this paper, this method was also used to infer $\mathrm{Im}(f_{CM}(\omega))$ (or ROT spectra) of different particle types for two medium conductivities.

3.3.1 Particle preparation and polynomial electrodes fabrication

In this section, two different cases of particle mixture were examined for separation: 1) mixture of 5-μm blue dyed aldehyde sulfate (AS) latex microspheres (Molecular Probes Inc., Eugene, OR, USA) and 8-μm glass microspheres (Microgenics Corp., Fremont, CA, USA), and 2) mixture of 8-μm glass microspheres and Lycopodium spores (ground pine or GP spores, Fisher Scientific, Fair Lawn, NJ, USA). Before running the in-droplet separation and concentration, DEP and ROT spectra for each particle type were first measured. In this measurement process, the particles were carefully washed using deionized water many times and then suspended in a DI water

solution. In order to adjust its conductivity, NaCl was added to the DI water solution. The conductivity of the solution was measured using a conductivity meter (Orion 3-Star Benchtop Conductivity Meter). For the above two cases of particle mixture, the conductivities were set at 10 $mS \cdot m^{-1}$ and 3 $mS \cdot m^{-1}$, respectively.

Three sets of the 2^{nd} order polynomial electrodes (the distance between opposite electrode tips were 100 μm, 200 μm and 1000 μm.) were fabricated using the standard photolithographic technology. For the electrodes, layers of 10 nm chromium and 100 nm gold were evaporated on a glass substrate by an E-beam evaporator, followed by wet-etching patterning. To ensure to have the same surface properties as the separation testing chips described in section V, the entire top surface of the electrode chip was spin coated with a 200 nm thick Teflon layer. Then, the particle suspended solution was pipetted onto the electrode chip and covered with a cover slip. The velocity and rotation of particles was recorded by a microscope (TE2000-U, Nikon) and CCD camera (KP-D20AU, Hitachi).

The DEP and ROT measurements have been performed over the frequency range between 1 kHz and 5 MHz. To measure the DEP spectra, a particle was placed close to the edge of the electrode or in the center between the four electrodes. The average velocity was determined by measuring particle traveling time between two concentric circles (Fig. 3(a)). To measure the ROT spectra, the particle was first positioned in the center by a negative DEP force and then the field was switchedto the rotation field. The images of particle rotation were analyzed to measure the rotation speed and direction.

3.3.2 DEP and ROT spectra results

Shown in Fig. 32(a) are dielectrophoretic (DEP) and electrorotation (ROT) spectra of the AS particles and glass particles, both suspending in the NaCl solution of conductivity 10 $mS \cdot m^{-1}$. Both particles show negative in the dielectrophoretic velocity in the entire range of examined frequency. That is, they move to the center of the polynomial electrodes, showing nDEP behavior regardless the applied frequency. The glass particle moves faster than the AS latex particle. In the meantime, although the electrorotation rates for both particles are close to 0 at the frequency of 10 kHz, they become significant as the frequency increases. More importantly, they rotate opposite to each other when the frequency is higher than 10 kHz. The AS particle rotates in the same direction as the rotating electric field (co-field rotation) while the glass particle rotates opposite to the rotating field (contra-field rotation). This means that $\mathrm{Im}(f_{CM}(\omega))$ of the AS particle is negative while $\mathrm{Im}(f_{CM}(\omega))$ of the glass particle is positive. To ensure clear separation of one type particle from another type using twDEP, the following two conditions need to be satisfied: (1) Both type particles first need to be vertically levitated from the electrodes. That is, a negative DEP force ($\mathrm{Re}(f_{CM}(\omega)) < 0$) is required for both types. (2) Both type particles should be horizontally propelled but opposite to each other. $\mathrm{Im}(f_{CM}(\omega))$ of the AS particle should be opposite to that of the glass particle. The shaded window in Fig. 32(a) satisfies the above two conditions. In particular, about 800 kHz (right end of the window) makes the difference of ROT spectra between two particle types maximum. Therefore, 800 kHz was chosen for the optimum frequency for in-droplet separation and concentration in section 3.3.4.

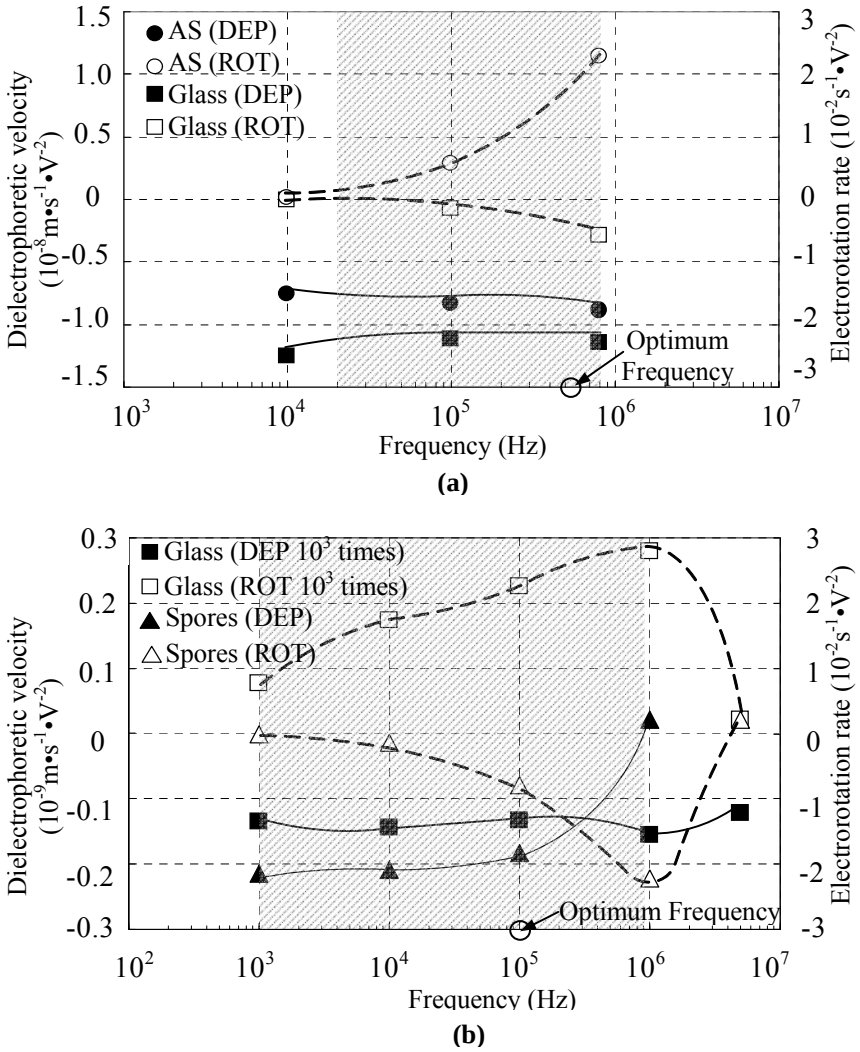

Figure 32. DEP and ROT spectra: (a) (case 1) AS latex beads and glass beads are suspended in solution of conductivity 10 mS·m^{-1}. At 800 kHz the AS latex beads exhibit co-field rotation, whilst the glass beads show contra-field rotation. The two types of particles both show negative DEP. (b) (case 2) Glass beads and GP spores are suspended in solution of conductivity 3 mS·m^{-1}. At 100 KHz the glass beads exhibit co-field rotation, whilst the spores show contra-field rotation. The two types of particles both show negative DEP as well. Note that a frequency window, in which particle separation is possible, is determined for each case, as hatched. Every data point represents the mean value averaged from randomly chosen three particles. The standard deviation for all the data points is less than 10%.

Similarly, the DEP and ROT spectra were also measured for the mixture of glass particles and GP spores, both suspending in the NaCl solution of the conductivity 3 $mS \cdot m^{-1}$. As shown in Fig. 32(b), the GP spore shows stable negative DEP and contra-field ROT in the frequency range between 1 kHz and 1 MHz. In particular, a contra-field ROT peak is located around at 1 MHz. However, at this frequency the DEP is close to zero. In the mean time, in the entire range of examined frequency, the glass particle shows stable negative DEP and co-field ROT, although they are about three orders of magnitude weaker than the GP spore. According to the two aforementioned conditions, the frequency region for successful twDEP separation can be identified as shaded in Fig. 32(b). The optimum frequency was chosen at 100 kHz, not 1 MHz, since the DEP spectra of the GP spore is close to zero at 1 MHz.

3.4 TESTING DEVICE FABRICATION AND EXPERIMENTAL SETUP FOR IN-DROPLET CONCENTRATION AND SEPARATION

Based on the measurements of DEP and ROT spectra, testing devices for in-droplet separation and concentration were fabricated using the standard lithographic micro fabrication technology. As shown in Fig. 33, the testing device mainly consists of two parallel plates (top and bottom). The bottom plate fabrication includes two main steps: metallization and patterning of twDEP electrodes and deposition of the hydrophobic layer. The twDEP electrodes consist of two sets of four spiral electrodes (Fig. 34). The droplet will be placed on the parallel electrode pattern in the middle of the two spiral electrode sets. This design allows us to avoid multi-layer wiring. All the signal lines of four-phase inputs were fabricated on a single plane, making fabrication process much easier. For the twDEP electrodes, a chromium layer of 100 Å in thickness as an adhesion

layer and a gold layer of 1000 Å in thickness were sequentially deposited on a glass wafer by sputtering and then patterned by wet etching into the spiral electrodes of 10 μm width and 10 μm spacing. The bottom plate was finally coated with a hydrophobic Teflon layer. Spin-coating of 2% Teflon solution (Teflon AF 1600® + Fluorocarbon solvent) resulted in a 2000 Å thick Teflon layer.

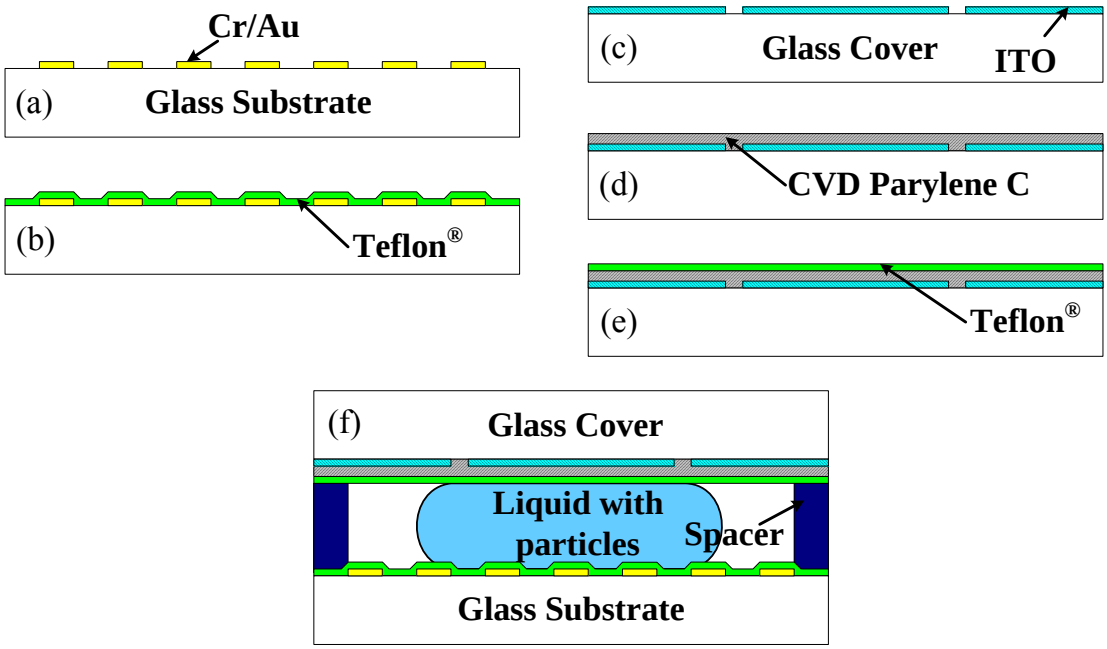

Figure 33. Fabrication process flow of testing devices: (a) deposition and patterning of electrodes (Cr/Au) on the bottom glass; (b) spin-coating of Teflon® AF; (c) Top glass cover with patterned ITO layer; (d) Deposition of parylene layer by CVD and patterning; (e) Spin-coating of Teflon® AF layer; (f) Integrating of the top and bottom plates with a spacer in between. The droplet containing particles is sandwiched between the plates.

The main fabrication process on the top plate consists of three steps: patterning of EWOD electrodes, deposition and patterning of the dielectric layer, and deposition of the hydrophobic layer. For the EWOD driving electrodes, an ITO (Indium Tin Oxide) layer was patterned by wet etching. Then, a 2-μm parylene layer as a dielectric layer was deposited using a vapor deposition

method (LABCOTER® 2, Specialty Coating Systems), followed by opening of the parylene layer on electrode pads by physical scratching in order to transmit activation signals to each driving electrode. Finally, the top plate was also spin-coated with the hydrophobic Teflon layer.

The last step of the fabrication process is to integrate the two plates (Fig. 33(f)). After putting a droplet containing particles on the bottom plate, the top cover plate was gently pressed against the spacers that were already placed on the bottom plate. The clean room tape was used for the spacers, making the channel gap at 70 μm that allows successful droplet splitting based on the design rule [77].

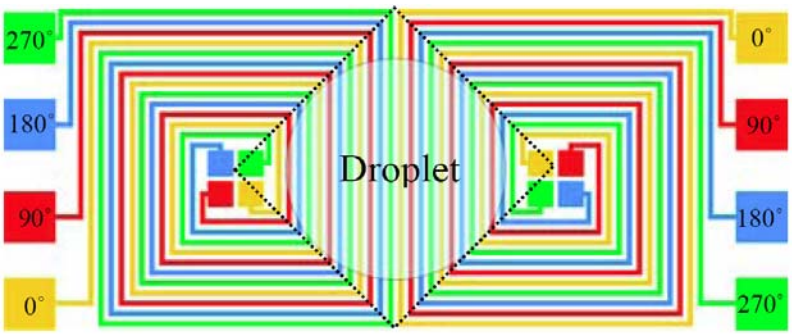

Figure 34. Top view of twDEP electrode design: A traveling wave of 90º phase shift to the adjacent electrodes is generated by two sets of four spiral electrodes. The droplet is placed on the area of straight parallel section (the dotted square) of the DEP electrodes. To avoid multi-layer wiring, a spiral type is used.

Figure 35 illustrates how to generate twDEP and EWOD signals. The whole system consists of a personal computer, a digital output board (DAQPad-6507, National Instrument), a custom-made phase shifter, amplifier and interface circuit mainly containing photo-coupled relays (PhotoMos®, AQW614EH, Aromat Co.). A PC-based program generates control signals transmitted through a digital I/O board. The control signals switch the relays through which four

phase signals are transmitted to the twDEP electrodes on the bottom plate and EWOD signals to the two EWOD electrodes on the top plate.

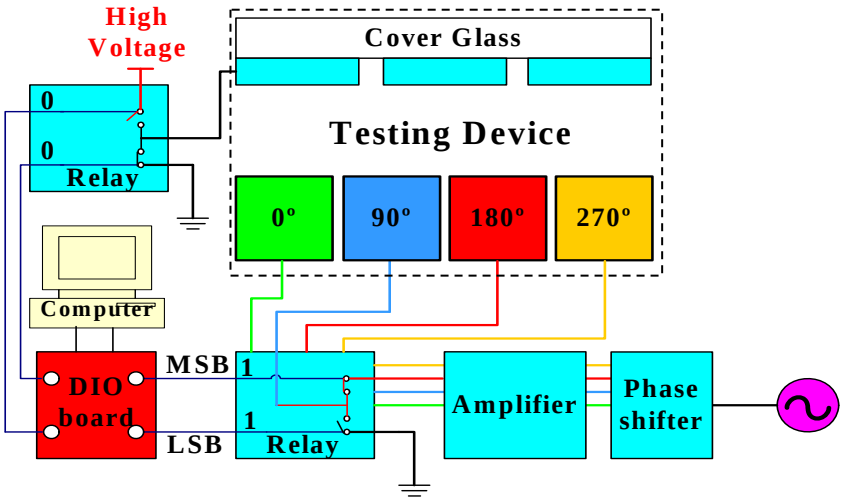

Figure 35. Schematic flow of twDEP and EWOD signals.

3.5 EXPERIMENT RESULTS OF PARTICLE CONCENTRATION AND SEPARATION

3.5.1 Particle concentration

We first tested particle transportation and concentration in a droplet using a single type of particle (5-μm aldehyde sulfate (AS) beads). Initially, a large number of AS beads were uniformly distributed over the droplet, as shown in Fig. 36(a). The conductivity of the droplet solution was set at 10 $mS \cdot m^{-1}$. The applied frequency to generate a travelling wave was set at the optimum frequency of 800 kHz (15 V_{p-p}) which was determined from the DEP and ROT spectra

results in Fig. 32(a). As shown in Fig. 36(b), most of the AS beads are transported and concentrated into the right edge of the droplet within 8 minutes after twDEP are activated on.

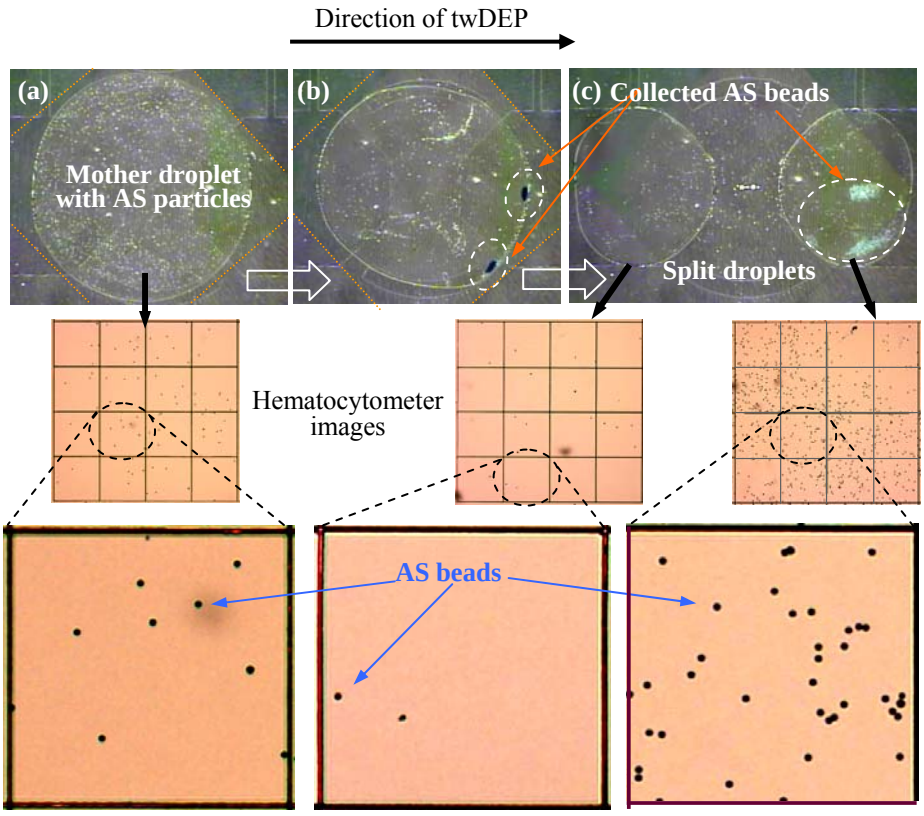

Figure 36. Sequential pictures of single type particle concentration: (a) Before twDEP actuation, 5-μm aldehyde sulfate (AS) beads are uniformly suspended in the droplet; (b) Most of the particles are collected in the right edge of the droplet under the twDEP wave (800 kHz, 15 Vp-p), especially into two spots; (c) After EWOD droplet splitting, the collected particles are secured in the right daughter droplet. The concentration efficiency is measured counting the particles on hematocytometer images. The dotted lines around the droplets represent the boundary of the straight parallel section of the DEP electrodes shown in Fig. 34.

Note that the dotted lines near the droplet represent the boundary of the straight parallel section of the DEP electrodes shown as a dotted square in Fig. 34. We can see two main blue spots (marked by broken circles in Fig. 36(b)) where the AS beads are finally concentrated. It is

interesting that the particles are collected into local spots, rather than distributed along the droplet edge. The two blue spots were observed only when the AS beads were used. It was confirmed that this phenomenon is not due to the dielectric breakdown and resultant electrolysis. It is speculated that the charges on the particles and/or their interaction with the interfaces may distort the applied electric field, thus possibly generating an attraction force to these spots.

After concentrating the particles within the droplet, splitting function by EWOD (1 kHz and 120 Vp-p) makes the droplet physically divided into two daughter droplets. After droplet splitting, the right daughter droplet contains higher populations of AS beads than the left droplet does, as shown in Fig. 36(c).

Table 4. Measured concentration efficiency of AS beads

	Mother droplet	Left droplet	Right droplet
Volume (μL)	0.44	0.23	0.21
Concentration (#/μL)	12298	491	25229
Percentile to total #	100 %	**2.1 %**	**97.9 %**

To evaluate the concentration efficiency, each split droplet is sucked into a hematocytometer chamber (Cell-VU® CBC) which makes particle distribution uniform with minimal clustering. The middle and bottom images in Fig. 36 show particles in the hematocytometer chamber. Consistently, they also show higher particle concentration in the right droplet than the left droplet. Using an image analysis tool, every particle on hematocytometer

images is counted. Qualitatively, 98% of the total AS particles are collected and isolated into the right droplet, as tabulated in Table 4. Note that the data shown in Table 4-6 are not statistically averaged but the general trend and behavior of particle concentration and separation have been confirmed consistent through the on-chip microscopic images obtained from repeated experiments.

3.5.2 Particle separation

The two different mixtures of particles, which were tested for DEP and ROT spectra in section 3.3, were also examined for particle separation. Case 1 is mixture of 5-μm AS beads and 8-μm glass beads. Case 2 is mixture of 8-μm glass beads and GP spores. The conductivities of the suspending medium for cases 1 and 2 were set at 10 $mS \cdot m^{-1}$ and 3 $mS \cdot m^{-1}$, respectively, which are the same as the ones in section 3.3

Shown in Fig. 37 are sequentially captured pictures of particle separation for case 1. Initially 5-μm blue-dyed aldehyde sulfate (AS) beads (seen as blue in the on-chip images) and 8-μm glass beads (seen as white in the on-chip images) are mixed in the droplet as shown in Fig. 37(a). A traveling wave was generated at the frequency of 800 kHz (15 V_{p-p}), which was also optimally determined in Fig. 32(a). Under the twDEP, the AS particles are moving to the right edge of the droplet. Note the traveling wave moves in the same direction as the AS particles. The moving direction of the AS beads is in agreement with the co-field rotation of the AS particles in Fig. 32(a). On the contrary, the glass particles did not move as substantially as the AS particles but they are overall pushed to the left to some extent. This is because $\mathrm{Im}(f_{CM}(\omega))$ of the glass particle is much smaller than that of the AS particle, as shown in Fig. 32(a). After about 10 minutes, almost all the AS (seen as blue) particles are collected in the right edge of the droplet as

shown in Fig. 37 (b), especially into two spots as well, while the glass beads are scattered mostly in the left region of the droplet. After the droplet is split by EWOD, large populations of the AS particles are separated into the right daughter droplet (Fig. 37(c)). As the particle counting results for each droplet are tabulated in Table 5, over 97% of the total AS particles are concentrated into the right daughter droplet while 77% of the total glass particles are separated into the left droplet.

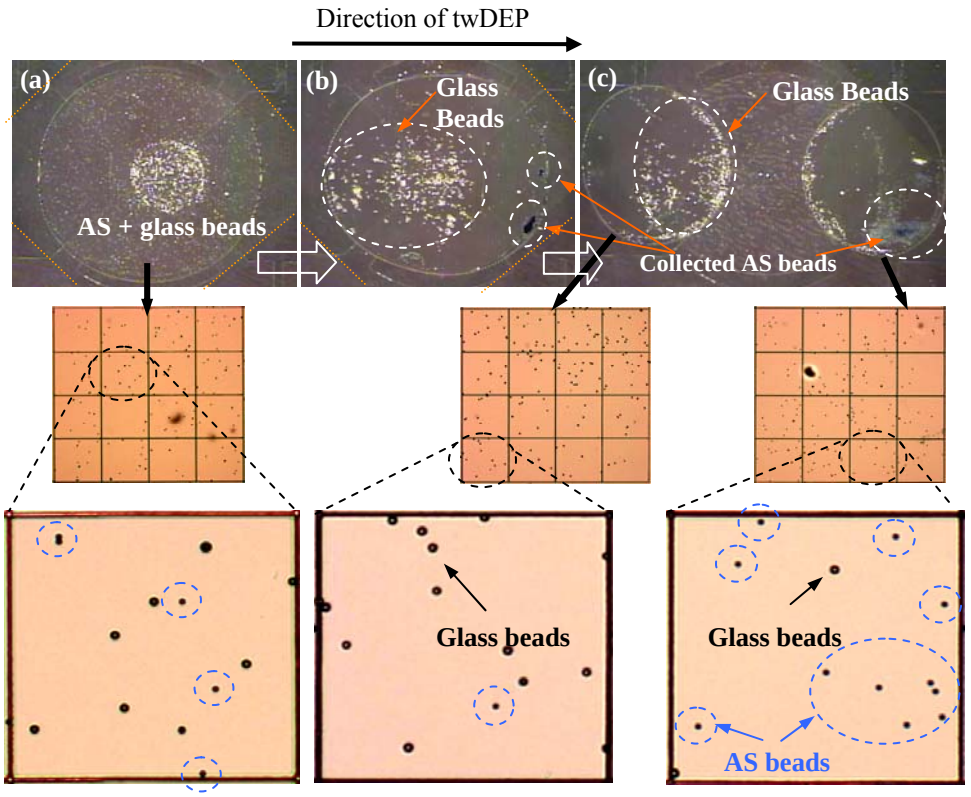

Figure 37. (Case 1) Sequential pictures of particle separation: (a) mixture droplet of 8-μm glass and 5-μm blue-dyed aldehyde sulfate (AS) beads; (b) The AS particles are moving to the right edge of the droplet under twDEP (800 kHz, 15 Vp-p) while glass beads are overall pushed to the left; (c) After EWOD droplet splitting, the AS particles are highly concentrated in the right droplet while the glass particles in the left droplet. The dotted lines around the droplets represent the boundary of the straight parallel section of the DEP electrodes shown in Fig. 34. The dotted circles on hematocytometer images denote the AS particles.

Table 5. Measured separation efficiency

	Mother droplet	Left droplet	Right droplet
Volume (μL)	0.37	0.19	0.18
AS beads (#/μL)	8057	437	16100
Percentile to total #	100 %	**2.8 %**	**97.2 %**
Glass beads (#/μL)	2768	4158	1300
Percentile to total #	100 %	**77.1 %**	**22.9 %**

Similarly, the mixture of GP spores and 8-μm glass beads (case 2) was successfully separated. Figure 38 shows the sequential pictures of separation process for case 2. Before separation, the GP spores (seen as big white dots in the on-chip images) and glass beads (seen as small white dots in the on-chip images) are mixed in the droplet as shown in Fig. 38(a). The frequency was set at 100 kHz (10 V_{p-p}) for the traveling wave, which was also optimally determined from the DEP and ROT spectra in Fig. 32(b). The GP spores are moved to the right edge of the droplet under twDEP. Here note that the traveling wave moves to the left. The motion of the GP spores opposite to the traveling wave is also in agreement with the ROT spectra in Fig. 32(b). In the mean time, the glass beads are moved to the left to some degree as its moving direction is predicted as well in Fig. 32(b). However, their moving speed is substantially low compared to the GP spores, as predicted from the ROT spectra in Fig. 32(b). After 5 minutes, the spores are collected at the right edge of the droplet while the glass beads are scattered more

likely in the left region of the droplet, as shown in Fig. 38 (b). After splitting, the GP spores are separated and concentrated in the right daughter droplet while the glass particles are abundant in the left droplet, as shown in Fig. 38(c). The particle counting results for each droplet show that 92 % of the total spores are collected in the right daughter droplet while 86% of the total glass particles are separated in the left droplet, as tabulated in Table 6.

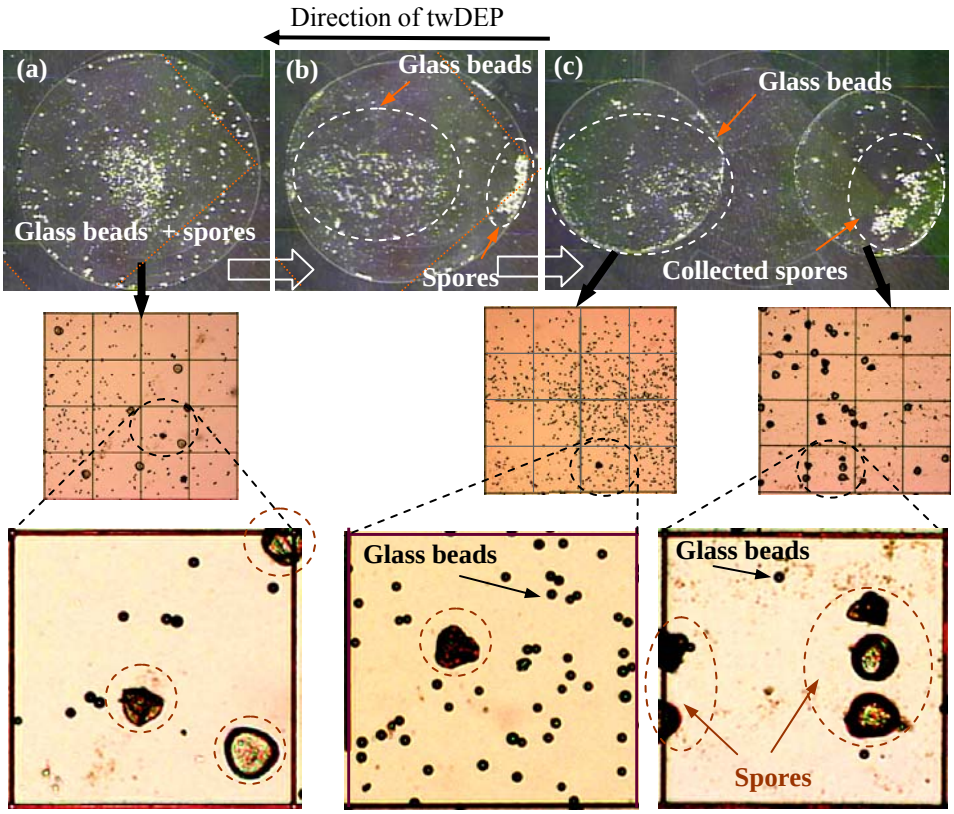

Figure 38. (Case 2) Sequential pictures of particle separation. Ground pine spores and glass beads are mixed (a) and then (b) separated under twDEP (100 kHz, 10 Vp-p). (c) finally split droplets. Spores are orange-circled. The dotted straight lines near the droplets represent the boundary of the straight parallel section of the DEP electrodes shown in Fig. 34.

Table 6. Measured separation efficiency

	Mother droplet	Left droplet	Right droplet
Volume (μL)	0.48	0.26	0.22
GPS (#/μL)	283	42	568
Percentile to total #	100 %	**8.1 %**	**91.9 %**
Glass beads (#/μL)	5267	8354	1618
Percentile to total #	100 %	**85.9 %**	**14.1 %**

3.6 DISCUSSION

A series of experiments demonstrated that highly responsive particles to twDEP, such as the AS particles in case 1 and the GP spores in case2, can be efficiently collected and isolated into the droplet edges, leading to high separation efficiency of over 92% for both cases after droplet splitting. On the contrary, the glass particles, which are not highly responsive to twDEP in nature, show relatively lower separation efficiency (77% for case 1 and 86% for case 2). As a result, a non-negligible number of glass particles are left in the right daughter droplets for both cases. This is because the glass particles initially located in the right side of the mixture droplet could not be completely transported to the left side of the droplet. Moreover, this lower responsivity results in longer separation time (sometimes over 10min).

One of the possible methods to circumvent this problem is to add a merging step before starting the twDEP separation step. In Fig. 29(a), for example, a pure solution droplet without any particles can be transported from the right and merged with the mixture droplet. After merging, the left half of the merged droplet is temporally occupied by the particle mixture and the right half only by the pure solution. Upon twDEP actuation, highly responsive particles move to the right half (i.e., to the pure solution area) while lowly responsive particles slightly move to the left. In this case, the initial background of the right half is the pure solution and the lowly responsive particles do not have to move a long distance. Consequently, in the right side only highly responsive particles are collected while in the left side only lowly responsive particles are collected. As a result, the separation efficiency would be higher in both droplets after splitting.

Overall, the present separation using twDEP shows higher separation efficiencies, compared to the in-droplet separation using electrophoresis [79]. This is because large-scale vortical flows inside the mother droplet do not occur during twDEP actuation, as opposed to electrophoresis. As discussed in Cho *et al.*, vortical flows generated in the droplet lowered the particle separation efficiency.

For higher separation efficiency, the DEP and ROT spectra have to be measured to determine the applied frequency and the conductivity of medium. As described in section IV. B, the two conditions should be satisfied for successful separation: (1) nDEP for two particle types in a mixture and (2) co-field ROT for one type and contra-field ROT for the other. In the process of finding these conditions, varying the applied frequency is a first and relatively easy approach. However, one should not overlook the importance of the medium conductivity σ_m. In some cases, the sign of DEP or ROT spectra can be changed by a slight change in the medium conductivity. For example, the difference of the medium conductivity between cases 1 and 2 are only 7

$mS \cdot m^{-1}$. However, the glass particle shows contra-field ROT in case 1 and co-field ROT in case 2.

For larger devices or droplets, the present separation method would be less efficient since the traveling distance the particles need to move over during the operation becomes longer. As a result, the total separation time would be longer and the particles would have more chances to stick to the device surfaces. On the contrary, if devices or droplets become smaller, the separation efficiency may be higher by the same argument. However, according to the droplet splitting criterion, the gap between the top and bottom plates have to be maintained much smaller than the droplet size with a certain ratio. If the droplet is too small, the gap between the plates may not accommodate relatively large particles. In the present experiments, the initial droplet size varies more or less case by case (see droplet volumes in Tables 4-6). This is due to the evaporation while the droplets and top plate were being positioned initially and the activation signals were being prepared. However, in this range of droplet volume variation, we could not find any noticeable effects on the concentration and separation efficiency.

We could not observe any noticeable Marangoni or electro-thermal flows during the operations. This is because the Joule heating may not be significant and heat dissipation may be fast enough in the present configuration. In the meantime, some circulating evaporation-driven flows were observed along the edge of the droplet which was exposed to the air environment. However, since the droplet was squeezed like a thin disk by the two plates, the evaporation-driven flows were highly localized near the droplet edge and not strong enough to affect the overall particle motions.

The present separation method seems to work in a relatively wide range of the initial particle concentration. However, it was observed that above a certain level in the initial particle

concentration locally circulating flows (vortices) were more frequently generated. This may be attributed to the electric field distortion by highly loaded particles. In the meantime, during the operations minor particle clustering was observed due mainly to surface forces among the particles. However, the clustering did not seem to significantly affect the overall concentration and separation efficiency. Interestingly, in the DEP and ROT spectra experiments, it was observed that each particle in clustered groups moved and rotated individually as if it was placed alone without clustering. This suggests that clustering does not significantly change the DEP force acting on the individual particles in the present conditions.

3.7 CONCLUSION

In this chapter, we described an in-droplet particle concentration and separation scheme using traveling wave dielectrophoresis (twDEP), which can offer an additional functionality to droplet-based digital microfluidics operated by electrowetting-on-dielectric (EWOD) principle. The scheme was proven experimentally using microfabricated testing devices. The separation scheme of two different types of particles consists of two main steps: (1) isolate each type of particle by twDEP into a designated region inside a mother droplet, (2) physically split the mother droplet into two daughter droplets by EWOD actuation so that the isolated particles of each type are highly concentrated into each daughter droplet. Similarly, by applying the separation scheme to a droplet containing only a single type of particle, the particle can be concentrated into a split droplet.

Successful concentration was experimentally achieved using 5-μm AS latex particles. An off-chip particle counting method quantitatively showed that 98% of the total particles are

concentrated into a split daughter droplet. Also, the in-droplet separation was successfully demonstrated using two different types of particles: 5-μm AS latex beads and 8-μm glass beads. After droplet splitting 97% of the total AS beads are separated into one split droplet and 77% of the total glass beads in the other split droplet. To extend the applicability to real biological samples, separation between biological spores (ground pine spores or GPS) and 8-μm glass beads was also demonstrated. Over 92% GP spores are separated into one daughter droplet while 86% glass beads in the other split droplet. In all these concentration and separation experiments, the applied frequency and the conductivity medium are key parameters controlling the concentration and separation efficiency, which have been optimally determined by measuring the dielectrophoretic (DEP) and electrorotation (ROT) spectra of used particles prior to the concentration and separation experiments.

BIBLIOGRAPHY

[1] M. G. Lippmann, "Relations entre les phénomènes electriques et capillaires," *Ann. Chim. Phys.*, vol. 5, pp. 494-549, 1875.

[2] H. Matsumoto and J. E. Colgate, "Preliminary investigation of micropumping based on electrical control of interfacial tension," presented at Proc. IEEE MEMS Workshop, Napa Valley, CA, Feb. 1990.

[3] B. Berge, "Electrocapillarity and wetting of insulator films by water," *Comptes Rendus de l'Academie des Sciences Serie II*, vol. 317, pp. 157-163, 1993.

[4] M. Vallet, B. Berge, and L. Vovelle, "Electrowetting of water and aqueous solutions on poly (ethylene terephthalate) insulating films," *Polymer*, vol. 37, pp. 2465-2470, 1996.

[5] J. Lee, H. Moon, J. Fowler, C.-J. Kim, and T. Schoellhammer, "Addressable micro liquid handling by electric control of surface tension," presented at Proc. IEEE Int. Conf. MEMS, Interlaken, Switzerland, Jan. 2001.

[6] J. Lee, H. Moon, J. Fowler, T. Schoellhammer, and C.-J. Kim, "Electrowetting and electrowetting-on-dielectric for microscale liquid handling," *Sens. Actuators, Phys. A*, vol. 95, pp. 259-268, 2002.

[7] H. Moon, S. K. Cho, R. L. Garrell, and C.-J. Kim, "Low voltage electrowetting-on-dielectric," *J. Appl. Phys.*, vol. 92, pp. 4080-4087, 2002.

[8] S. K. Cho, S.-K. Fan, H. Moon, and C.-J. Kim, "Towards digital microfluidic circuits: creating, transporting, cutting and merging liquid droplets by electrowetting-based actuation," presented at Proceedings of IEEE International Conference on MEMS, Las Vegas, Nevada, USA, 2002.

[9] S. K. Cho, H. Moon, and C.-J. Kim, "Creating, transporting, cutting, and merging liquid droplets by electrowetting-based actuation for digital microfluidic circuits," *J. Microelectromech. Syst.*, vol. 12, pp. 70, 2003.

[10] C. A. Robbins, L. J. Swenson, M. L. Neally, and R. E. Gots, "Health effects of mycotoxins in indoor air: a critical review," *Applied Occupational and Environmental Hygiene*, vol. 15, pp. 773-784, 2000.

[11] S. K. Mishra, L. Ajello, D. Ahearn, H. Burge, V. P. Kurup, D. L. Pierson, D. L. Price, R. B. Samsons, and K. F. Switzer, "Environmental mycology and its importance to public health," *Journal of Medical and Veterinary Mycology*, vol. 30, pp. 296-305, 1992.

[12] W. D. Griffiths and A. L. DeCosemo, "The assessment of bioaerosols: A critical review," *J. Aerosol. Sci.*, vol. 25, pp. 1425, 1994.

[13] H. A. Burge, *Bioaerosols*. Boca Raton, FL: Lewis Publishers, 1995.

[14] H. A. Burge, D. L. Pierson, T. O. Groves, K. F. Strawn, and S. K. Mishra, "Dynamics of airborne fungal populations in a large office building," *Curr. Microbiol.*, vol. 40, pp. 10, 2000.

[15] R. L. Gorny, T. Reponen, K. Willeke, D. Schmechel, E. Robine, M. Boissier, and S. A. Grinshpun, "Fungal fragments as indoor air biocontaminants," *Applied and Environmental Microbiology*, vol. 68, pp. 3522-3531, 2002.

[16] S. K. Mehta, S. K. Mishra, and D. L. Pierson, "Evaluation of three portable samplers for monitoring airborne fungi," *Appl. Environ. Microbiol.*, vol. 62, pp. 1835, 1996.

[17] S. K. Mehta, D. M. Bell-Robinson, T. O. Groves, L. D. Stetzenbach, and D. L. Pierson, "Evaluation of portable air samplers for monitoring airborne culturable bacteria," *Am. Ind. Hyg. Assoc. J.*, vol. 61, pp. 850, 2000.

[18] T. J. Mukoda, L. A. Todd, and M. D. Sobsey, "PCR and gene probes for detecting bioaerosols," *Journal of Aerosol Science*, vol. 25, pp. 1523-1532, 1994.

[19] M. P. Schafer, J. E. Fernback, and M. K. Ernst, "Detection and characterization of airborne Mycobacterium tuberculosis H37Ra particles, a surrogate for airborne pathogenic M. tuberculosis," *Aerosol Science and Technology*, vol. 30, pp. 161-173, 1999.

[20] R. F. Service, "Labs on a chip: Coming soon: The pocket DNA sequencer," *Science*, vol. 282, pp. 339, 1998.

[21] A. W. Chow, "Lab-on-a-chip: Opportunities for chemical engineering," *AIChE J.*, vol. 48, pp. 1590, 2002.

[22] R. Ehrnstrom, "Miniaturization and integration: challenges and breakthroughs in microfluidics," *Lab Chip*, vol. 2, pp. 26N-30N, 2002.

[23] A. R. Kopf-Sill, "Successes and challenge of lab-on-a-chip," *Lab Chip*, vol. 2, pp. 42N, 2002.

[24] G. Ehrenman, "Shrinking the lab down to size," *Mechanical Engineering*, vol. 126, pp. 26-29, 2004.

[25] J. G. E. Gardeniers and A. van den Berg, "Lab-on-a-chip systems for biomedical and environmental monitoring," *Annals of Bioanalytical Chemistry*, vol. 378, pp. 1700-1703, 2004.

[26] R. Swannell, "Fluorescent techniques for detecting microorganisms," presented at In Rapid Methods for Diagnosis of Microbial Problems in the Petroleum Industry, Institute of Petroleum, London, 1991.

[27] Q.-Y. Zeng, S.-O. Westermark, A. Rasmuson-Lestander, and X.-R. Wang, "Detection and quantification of Cladosporium in aerosols by real-time PCR," *Journal of Environmental Monitoring*, vol. 8, pp. 153-160, 2006.

[28] M. G. Pollack, R. B. Fair, and A. D. Shenderov, "Electrowetting-based actuation of liquid droplets for microfluidic applications," *Appl. Phys. Lett.*, vol. 77, pp. 1725-1726, 2000.

[29] M. G. Pollack, A. D. Shenderov, and R. B. Fair, "Electrowetting-based actuation of droplets for integrated microfluidics," *Lab Chip*, vol. 2, pp. 96-101, 2002.

[30] P. R. C. Gascoyne and J. V. Vykoukal, "Dielectrophoresis-Based Sample Handling in General-Purpose Programmable Diagnostic Instruments," *Proc. IEEE*, vol. 92, pp. 22-24, 2004.

[31] C. Y. Zhang, H. C. Yeh, M. T. Kuroki, and T. H. Wang, "Single-quantum-dot-based DNA nanosensor," *Nature Materials*, vol. 4, pp. 826-831, 2005.

[32] Y. Ho, Kung, Y. M., S., and T. H. Wang, "Multiplexed hybridization detection with multicolor colocalization of quantum dot nanoprobes," *Nano Letters*, vol. 5, pp. 1693-1697, 2005.

[33] J. M. Yang, C.-M. Ho, X. Yang, and Y.-C. Tai, "Micromachined particle filter with low power dissipation," *Journal of Fluids Engineering*, vol. 123, pp. 899-908, 2001.

[34] T. K. Hsiai, S. K. Cho, J. M. Yang, X. Yang, Y.-C. Tai, and C.-M. Ho, "Pressure drops of water flow through micromachined particle filters," *Journal of Fluids Engineering*, vol. 124, pp. 1053-1056, 2002.

[35] A. Desai, S.-W. Lee, and Y.-C. Tai, "An air-to-liquid MEMS particle sampler," presented at Proceedings of 13th MEMS Conference, Sendai, Japan, 2000.

[36] F. Mugele and J.-C. Baret, "Electrowetting: from basics to applications," *J. Phys.: Condens. Matter*, vol. 17, pp. R705, 2005.

[37] C. Y. Zhang, S. Y. Chao, and T. H. Wang, "Comparative quantification of nucleic acids using single-molecule detection and molecular beacons," *Analyst*, vol. 130, pp. 483-488, 2005.

[38] T. H. Wang, Y. H. Peng, C. Y. Zhang, P. K. Wong, and C. M. Ho, "Single-molecule tracing on a fluidic microchip for quantitative detection of low-abundance nucleic acids," *Journal of the American Chemical Society*, vol. 127, pp. 5354-5359, 2005.

[39] H. A. Burge and W. R. Solomon, "Sampling and analysis of biological aerosols," *Atmos. Environ.*, vol. 21, pp. 451, 1987.

[40] W. Eduard and D. Heederik, "Methods for Quantitative Assessment of Airborne Levels of Noninfectious Microorganisms in Highly Contaminated Work Environments," *Am. Ind. Hyg. Assoc. J.*, vol. 59, pp. 113, 1998.

[41] P. A. Jensen, W. F. Todd, G. N. Davis, and P. V. Scarpino, "Evaluation of eight bioaerosol samplers challenged with aerosols of free bacteria," *Am. Ind. Hyg. Assoc. J.*, vol. 53, pp. 660, 1992.

[42] W.-H. Lin and C.-S. Li, "Collection Efficiency and Culturabilityof Impingement into a Liquid for Bioaerosols of Fungal Spores and Yeast Cells," *Aerosol Sci. Technol.* , vol. 30, pp. 109, 1999.

[43] H. R. An, G. Mainelis, and M. Yao, "Evaluation of a high-volume portable bioaerosol sampler in laboratory and field environments," *Indoor Air*, vol. 14, pp. 385, 2004.

[44] P. Görner, J.-F. Fabriès, P. Duquenne, O. Witschger, and R. Wrobel, "Bioaerosol sampling by a personal rotating cup sampler CIP 10-M," *J. Environ. Monit.*, vol. 8, pp. 43, 2006.

[45] C. D. Chin, V. Linder, and S. K. Sia, "Lab-on-a-chip devices for global health: Past studies and future opportunities," *Lab Chip*, vol. 1, pp. 41, 2007.

[46] T. Frisk, D. Rönnholm, W. v. d. Wijngaart, and G. Stemme, "A micromachined interface for airborne sample-to-liquid transfer and its application in a biosensor system," *Lab Chip*, vol. 6, pp. 1504, 2006.

[47] R. B. Fair, A. Khlystov, V. Srinivasan, V. K. Pamula, and K. N. Weaver, "Integrated chemical/biochemical sample collection, pre-concentration, and analysis on a digital microfluidic lab-on-achip platform," presented at OpticsEast 2004, Conference 5591-17, Philadelphia, PA, USA, 2004.

[48] Y. Zhao and S. K. Cho, "Micro particle sampling using electrowetting-actuated droplet sweeping," presented at The 13th International Conference on Solid-State Sensors, Actuators and Microsystems (Transducers 2005), Seoul, Korea, 2005.

[49] M. G. Lippmann, "Relations entre les phénomènes electriques et capillaires," *Ann. Chim. Phys.*, vol. 151, pp. 494, 1875.

[50] B. Berge, "Electrocapillarity and wetting of insulator films by water," *C. R. Acad. Sci. Ser. II*, vol. 317, pp. 157, 1993.

[51] A. F. M. Leenaars and S. B. G. O'Brien, "Particle removal from silicon substrates using surface tension forces," *Philips Journal of Research*, vol. 44, pp. 183-209, 1989.

[52] J. Visser, "Particle adhesion and removal: A review," *Particulate Science and Technology*, vol. 13, pp. 169-196, 1995.

[53] J. Visser, *Surface Science and Colloid Science*, vol. 8. Willy, New York, 1976, p. 3.

[54] A. D. Zimon, *Adhesion of Dust and Powder*. Plenum, New York, 1982.

[55] W. J. O'Brien, "Capillary penetration of liquids between dissimilar solids," vol. PhD. Ann Arbor: Univesity of Michigan, (Univ. Microfilm No. 6715666), 1967.

[56] H. Morgan and N. G. Green, *AC Electrokinetics: Colloids and Nanoparticles*. Baldock, Hertfordshire, England: Research Studies Press Ltd., 2003.

[57] T. N. Krupenkin, J. A. Taylor, T. M. Schneider, and S. Yang, "From Rolling Ball to Complete Wetting: The Dynamic Tuning of Liquids on Nanostructured Surfaces," *Langmuir*, vol. 20, pp. 3824, 2004.

[58] M. S. Dhindsa, N. R. Smith, and J. Heikenfeld, "Reversible Electrowetting of Vertically Aligned Superhydrophobic Carbon Nanofibers," *Langmuir*, vol. 22, pp. 9030, 2006.

[59] N. Verplanck, E. Galopin, J.-C. Camart, and V. Thomy, "Reversible Electrowetting on Superhydrophobic Silicon Nanowires," *Nano Lett.*, vol. 7, pp. 813, 2007.

[60] A. B. D. Cassie, "Contact Angles," *Discussion Faraday Soc.*, vol. 3, pp. 11-16, 1948.

[61] T. N. Wenzel, "Surface roughness and contact angle," *Journal of Physics Colloid Chemistry*, vol. 53, pp. 1466-1467, 1949.

[62] D. Quéré, "Non-sticking drops," *Reports on Progress in Physics*, vol. 68, pp. 2495-2532, 2005.

[63] J. R. E. Johnson and R. H. Dettre, "Contact angle hysteresis I. study of an idealized rough surface," *Advances in Chemistry Series*, vol. 43, pp. 112-135, 1964.

[64] V. Bahadur and G. S. V., "Electrowetting-based control of static droplet states on rough surfaces," *Langmuir*, vol. 23, pp. 4918-4924, 2007.

[65] S. K. Chung, Y. Zhao, and S. K. Cho, "Micro particle sampling on a perforated filter membrane by EWOD-actuated droplet sweeping," presented at The 10th International Conference on Miniturized Systems for Chemistry and Life Science (Micro TAS 2006), Tokyo, Japan, 2006.

[66] W. J. O'Brien, "Capillary penetration of liquids between dissimilar solids," vol. Doctoral. Ann Arbor, USA: University of Michigan, 1967.

[67] R. Arshady, "Microsperes for biomedical applications: preparation of reactive and labelled microspheres," *J. Biomater.*, vol. 14, pp. 5, 1993.

[68] G. Gillies, M. Kappl, and H.-J. Butt, "Direct measurement of particle-bubble interactions," *Adv. Colloid Interface Sci.*, vol. 114-115, pp. 165, 2005.

[69] Y. Zhao and S. K. Cho, "Microparticle Sampling by Electrowetting-Actuated Droplet Sweeping," *Lab Chip*, vol. 6, pp. 137, 2006.

[70] Y. Zhao and S. K. Cho, "Micro particle sampling using electrowetting-actuated droplet sweeping," presented at The 13th International Conference on Solid-State Sensors, Actuators and Microsystems (Transducers 2005), Seoul, Korea, 2005.

[71] Y. Zhao and S. K. Cho, "Microparticle sampling by electrowetting-actuated droplet sweeping," *Lab Chip*, vol. 6, pp. 137-144, 2006.

[72] S.-K. Chung, Y. Zhao, and S. K. Cho, "Micro particle sampling on a perforated filter membrane by EWOD-actuated droplet sweeping," presented at μTAS 2006, Tokyo, Japan, pp. 31-33, 2006.

[73] Y. Zhao, S. K. Chung, U.-C. Yi, and S. K. Cho, "Micro Particle Sampling on Microfabricated Perforated Filter Membranes," presented at The 11th International Conference on Miniaturized Systems for Chemistry and Life Sciences (μTAS 2007), Paris, France, 2007.

[74] J. M. Yang, C.-M. Ho, X. Yang, and Y.-C. Tai, "Micromachined particle filters with low power dissipation," *J. Fluids Eng.*, vol. 123, pp. 899-908, 2001.

[75] P. R. C. Gascoyne and J. V. Vykoukal, "Particle Separation by Dielectrophoresis," *Electrophoresis*, vol. 23, pp. 1973-1983, 2002.

[76] C. H. Kua, Y. C. Lam, C. Yang, and K. Youcef-Toumi, "Review of Bio-particle Manipulation Using Dielectrophoresis," *Innovation in Manufacturing Systems and Technology*, 2005. Available at: http://hdl.handle.net/1721.1/7464.

[77] S. K. Cho, H. Moon, and C.-J. Kim, "Creating, Transporting, Cutting and Merging of Liquid Droplets by Electrowetting-Based Actuation for Digital Microfluidic Circuits," *J. MEMS.*, vol. 12, pp. 70 - 80, 2003.

[78] Y. Zhao and S. K. Cho, "Micro air bubble manipulation by electrowetting on dielectric (EWOD): transporting, splitting, merging and eliminating of bubbles," *Lab Chip*, vol. 7, pp. 273-280, 2007.

[79] S. K. Cho and C.-J. Kim, "Particle Separation and Concentration Control for Digital Microfluidics Systems," presented at 16th IEEE MEMS Conference, Kyoto, Japan, 2003, pp. 686-689.

[80] H. A. Pohl, *Dielectrophoresis: The behavior of neutral matter in nonuniform electric fields*. Cambridge, U. K.: Cambridge Univ. Press, 1978.

[81] R. Pethig, Y. Huang, X.-B. Wang, and J. P. H. Burt, "Positive and negative dielectrophoretic collection of colloidal particles using interdigitated castellated microelectrodes," *J. Phys. D: Appl. Phys.*, vol. 24, pp. 881-888, 1992.

[82] P. R. C. Gascoyne, Y. Huang, R. Pethig, J. Vykoukal, and F. F. Becker, "Dielectrophoretic separation of mammalian cells studied by computerized image analysis," *Meas. Sci. Technol.*, vol. 3, pp. 439-445, 1992.

[83] X.-B. Wang, Y. Huang, J. P. H. Burt, G. H. Markx, and R. Pethig, "Selective dielectrophoretic confinement of bioparticles in potential energy wells," *J. Phys. D: Appl. Phys.*, vol. 26, pp. 1278-1285, 1993.

[84] G. H. Markx, M. S. Talary, and R. Pethig, "Separation of viable and non-viable yeast using dielectrophoresis," *J. Biotech.*, vol. 32, pp. 29-37, 1994.

[85] F. F. Becker, X.-B. Wang, Y. Huang, R. Pethig, J. Vykoukal, and P. R. C. Gascoyne, "Separation of human breast cancer cells from blood by differential dielectric affinity," *Proc. Natl. Acad. Sci. USA*, vol. 92, pp. 860-864, 1995.

[86] N. G. Green and H. Morgan, "Dielectrophoretic separation of nanoparticles," *J. Phys. D: Appl. Phys.*, vol. 30, pp. L41-L84, 1997.

[87] J. Cheng, E. L. Sheldon, L. Wu, M. J. Heller, and J. P. O'Connell, "Isolation of Cultured Cervical Carcinoma Cells Mixed with Peripheral Blood Cells on a Bioelectronic Chip," *Anal. Chem.*, vol. 70, pp. 2321-2326, 1998.

[88] H. Morgan, M. P. Hughes, and N. G. Green, "Separation of submicron bioparticles by dielectrophoresis," *Biophys. J.*, vol. 77, pp. 516-525, 1999.

[89] Y. Huang, S.-H. Joo, M. Duhon, M. Heller, B. Wallace, and X. Xu, "Dielectrophoretic cell separation and gene expression profiling on microelectronic chip arrays," *Anal. Chem.*, vol. 74, pp. 3362-3371, 2002.

[90] G. H. Markx, R. Pethig, and J. Rousselet, "The dielectrophoretic levitation of latex beads, with reference to field-flow fractionation," *J. Phys. D: Appl. Phys.*, vol. 30, pp. 2470-2477, 1997.

[91] X.-B. Wang, J. Vykoukal, F. F. Becker, and P. R. C. Gascoyne, "Separation of Polystyrene Microbeads Using Dielectrophoretic/Gravitational Field-Flow-Fractionation," *Biophys. J.*, vol. 74, pp. 2689-2701, 1998.

[92] J. Rousselet, G. H. Markx, and R. Pethig, "Separation of erythrocytes and latex beads by dielectrophoretic levitation and hyperlayer field-flow fractionation," *Colloids Surf. A*, vol. 140, pp. 209-216, 1998.

[93] J. Yang, Y. Huang, X.-B. Wang, F. F. Becker, and P. R. C. Gascoyne, "Cell separation on microfabricated electrodes using dielectrophoretic / gravitational field-flow-fractionation," *Anal. Chem.*, vol. 71, pp. 911-918, 1999.

[94] X.-B. Wang, J. Yang, Y. Huang, J. Vykoukal, F. F. Becker, and P. R. C. Gascoyne, "Cell Separation by Dielectrophoretic Field-flow-fractionation," *Anal. Chem.*, vol. 72, pp. 832-839, 2000.

[95] J. Yang, Y. Huang, X.-B. Wang, F. F. Becker, and P. R. C. Gascoyne, "Differential Analysis of Human Leukocytes by Dielectrophoretic Field-Flow-Fractionation " *Biophys. J.*, vol. 78, pp. 2680-2689, 2000.

[96] S. Masuda, M. Washizu, and M. Iwadare, "Separation of Small Particles Suspended in Liquid by Non-uniform Travelling Field," *IEEE Trans. Ind. Appl.*, vol. 23, pp. 474-480, 1987.

[97] S. Masuda, M. Washizu, and I. Kawabata, "Movement of Blood Cells in Liquid by Non-uniform Travelling Field," *IEEE Trans. Ind. Appl.*, vol. 24, pp. 217-222, 1988.

[98] R. Hagedorn, G. Fuhr, T. Müller, and J. Gimsa, "Traveling-wave dielectrophoresis of microparticles," *Electrophoresis*, vol. 13, pp. 49-54, 1992.

[99] M. P. Hughes, R. Pethig, and X.-B. Wang, "Dielectrophoretic forces on particles in travelling electric fields," *J. Phys. D: Appl. Phys.*, vol. 29, pp. 474-482, 1996.

[100] M. S. Talary, J. P. H. Burt, J. A. Tame, and R. Pethig, "Electromanipulation and separation of cells using travelling electric fields," *J. Phys. D: Appl. Phys.*, vol. 29, pp. 2198-2203, 1996.

[101] A. D. Goater, J. P. H. Burt, and R. Pethig, "A combined travelling wave dielectrophoresis and electrorotation device: applied to the concentration and viability determination of Cryptosporidium " *J. Phys. D: Appl. Phys.*, vol. 30, pp. L65-L69, 1997.

[102] L. Cui, D. Holmes, and H. Morgan, "The dielectrophoretic levitation and separation of latex beads in microchips," *Electrophoresis*, vol. 22, pp. 3893-3901, 2001.

[103] P. Gascoyne, C. Mahidol, M. Ruchirawat, J. Satayavivad, P. Watcharasit, and F. F. Becker, "Microsample preparation by dielectrophoresis: isolation of malaria," *Lab Chip*, vol. 2, pp. 70-75, 2002.

[104] Y. Huang, R. Hölzel, R. Pethig, and X.-B. Wang, "Difference in the AC electrodynamics of viable and non-viable yeast cells determined through combined dielectrophoresis and electroroatation studies," *Phys. Med. Biol.*, vol. 37, pp. 1499-1517, 1992.

[105] Y. Zhao, U.-C. Yi, and S. K. Cho, "Highly Efficient in-Droplet Particle Concentration and Separation by twDEP and EWOD for Digital Microfluidics " presented at 20th IEEE MEMS Conference, Kobe, Japan, 2007, pp. 537-540.

[106] Y. Zhao, U.-C. Yi, and S. K. Cho, "In-droplet Particle Separation by Traveling Wave Dielectrophoresis (twDEP) and EWOD," presented at Solid-State Sensors, Actuators, and Microsystems Workshop, Hilton Head Island, SC, USA, 2006, pp.181-184.

[107] X.-B. Wang, Y. Huang, F. F. Becker, and P. R. C. Gascoyne, "A unified theory of dielectrophoresis I and travelling wave dielectrophoresis," *J. Phys. D: Appl. Phys.*, vol. 27, pp. 1571-1574, 1994.